Universidade de Aveiro Departamento de Engenharia de Materiais e Cerâmica
2021

Francisca Gonçalves Perfeito

Development of magnetic temperature sensors for hyperthermia and cryogeny applications

Desenvolvimento de sensores magnéticos de temperatura para hipertermia e aplicações criogénicas

Universidade de Aveiro
2021
Departamento de Engenharia de Materiais e Cerâmica

Francisca Gonçalves Perfeito

Development of magnetic temperature sensors for hyperthermia and cryogeny applications

Desenvolvimento de sensores magnéticos de temperatura para hipertermia e aplicações criogénicas

Dissertação apresentada à Universidade de Aveiro para cumprimento dos requisitos necessários à obtenção do grau de Mestre em Materiais e Dispositivos Biomédicos, realizada sob a orientação científica do Doutor Nuno João de Oliveira e Silva, Investigador Principal do Laboratório Associado CICECO do Departamento de Física da Universidade de Aveiro e co-orientação da Doutora Ana Daniela Gonçalves Firmino, Investigadora Júnior do Laboratório Associado CICECO – Instituto de Materiais da Universidade de Aveiro.

This work is a contribution to the Project On2Off Nanomagnets (POCI-01-0145-FEDER-029460) funded by FCT – Fundação para a Ciência e Tecnologia, I.P., through national funds, and the co-funding by the FEDER, within the PT2020 Partnership Agreement and Compete 2020.

Dedico esta tese aos meus pais, à minha irmã e ao meu melhor amigo. Dedico também esta tese à minha bisavó materna e avós, que direta ou indiretamente, me apoiaram ao longo do meu percurso.

o júri

Presidente	Doutora Paula Celeste da Silva Ferreira Investigadora Coordenadora em Regime Laboral da Universidade de Aveiro
Orientador	Doutor Nuno João de Oliveira e Silva Investigador Principal do Departamento de Física da Universidade de Aveiro
Arguente	Doutora Ana Luísa Daniel da Silva Investigadora Auxiliar em Regime Laboral da Universidade de Aveiro

agradecimentos

Gostaria de agradecer ao meu orientador, Doutor Nuno João de Oliveira e Silva, por me ter dado a oportunidade de desenvolver este trabalho, pela sua constante disponibilidade, excelente orientação científica e incansável apoio prestado no decorrer desta dissertação.

Agradeço também à minha coorientadora, Doutora Daniela Firmino, pela sua disponibilidade, motivação, correções, e acompanhamento ao longo deste trabalho, sem o qual este teria sido muito mais custoso.

Agradeço a todos os meus colegas e amigos do laboratório por proporcionarem um bom ambiente e pela sua permanente disponibilidade.

Ainda à Daniela Firmino, o meu profundo agradecimento pela sua paciência, boa disposição, disponibilidade e imensurável orientação, nos aspetos práticos e teóricos do trabalho laboratorial.

Gostaria de agradecer também à Doutora Rosário Soares pela formação e disponibilidade no âmbito da Difração de Raios X e pela sua amizade. Gostaria de agradecer também pelas análises de microscopia eletrónica à Doutora Marta Ferro e ao Doutor Ricardo Silva.

Agradeço também a todos os membros do Complexo de Laboratórios Tecnológicos e Departamento de Química bem como o Departamento de Engenharia de Materiais e Cerâmica da Universidade de Aveiro pelo seu apoio e contribuição para a minha aprendizagem e manuseamento dos diversos equipamentos para realizar o meu trabalho.

Por fim, gostaria de agradecer à minha mãe, ao meu pai, à minha irmã e ao meu melhor amigo, pela indispensável motivação, apoio e bem-estar que proporcionaram ao longo deste percurso, sem o qual não seria possível chegar onde estou hoje.

palavras-chave

Mn-Zn ferrites; Nanotermómetros; Sensores remotos; Hipertermia; Criopreservação.

resumo

Nanopartículas magnéticas de óxido de ferro têm atraído a atenção da comunidade científica ao longo dos anos devido às suas características promissoras, tais como a sua biocompatibilidade *in vivo*, modificações de superfície versáteis e síntese fácil. Com isso em mente, no que toca a sensores de temperatura, estes constituem uma das mais delicadas áreas da termometria quando aplicado a processos como hipertermia magnética e criopreservação, que possuem uma forte dependência a mudanças mínimas de temperatura. Na verdade, obter informações sobre as pequenas variações de temperatura que ocorrem em escala celular é atualmente abordado usando nanotermómetros com base na dependência bem definida de uma determinada propriedade com a temperatura. No entanto, as abordagens atuais são baseadas principalmente em propriedades óticas, sendo limitadas por vários inconvenientes, tais como a penetração ineficiente da luz em muitos tecidos, por exemplo. Visando superar este grande desafio, as nanopartículas magnéticas apresentam um enorme potencial, pois combinam o tamanho adequado para internalização em células e os campos magnéticos podem facilmente penetrar nos tecidos, possibilitando a monitoração remota da temperatura com o magnetismo.

Neste contexto, o objetivo desta tese é desenvolver nanopartículas estáveis de ferrite Mn-Zn dispersas em meio aquoso para atuar como sensores remotos de temperatura para aplicações biológicas, em particular para hipertermia magnética e criopreservação.

Nanopartículas $Mn_xZn_{1-x}Fe_2O_4$ foram produzidas com sucesso usando duas metodologias distintas: decomposição térmica e pelo método de sais fundidos auxiliado pelo aumento de temperatura. As nanopartículas preparadas foram analisadas por microscopia eletrônica de varrimento (SEM), microscopia eletrônica de varrimento em modo de transmissão (TEM), espectroscopia dispersiva de energia de raios-X (EDS), espectroscopia de infravermelho com transformada de Fourier (FT-IR), espalhamento de luz dinâmico (DLS), potencial zeta, e propriedades magnéticas. A difração de raios-X (XRD) verificou com sucesso a presença de uma estrutura cristalina cúbica com uma fase predominante no grupo espacial $Fd\bar{3}m$ das ferrites Mn-Zn produzidas por ambas as metodologias. A espectroscopia FT-IR foi utilizada para avaliar a presença de vários compostos na superfície das nanopartículas, como por exemplo, a funcionalização das partículas com ácido cítrico e EDTA. Além disso, a análise do Refinamento de Rietveld foi útil para discriminar os tamanhos de nanopartículas, que, no geral, constituíram diâmetros variando de 5.9 a 15 nm na metodologia por decomposição térmica e tamanhos entre 1.3 a 4.2 nm na metodologia por sais fundidos. Foram realizadas medidas de magnetização das nanopartículas para avaliar seu potencial como nanotermómetros magnéticos, nos quais as nanopartículas $Mn_{0.30}Zn_{0.47}Fe_2O_4$ (amostra TD9) com um tamanho de cerca de 6.9 nm, demonstraram reversibilidade entre 150 e 375 K com um máximo de sensibilidade (S_m) de cerca de 2.9 $\%.K^{-1}$ a 225 K. Para além disso, também se verificou que as nanopartículas $Mn_{0.11}Zn_{0.78}Fe_2O_4$ (amostra TD4) com um tamanho de cerca 8.0 nm revelaram funcionar como um sensor entre 300 e 400 K com uma máxima sensibilidade máxima de aproximadamente 2.1 $\%.K^{-1}$ a 300 K. Tendo em conta estes resultados, as nanopartículas produzidas são consideradas apropriadas para aplicações de hipertermia e criopreservação. Por fim, a encapsulação destes ferrofluidos foi efetuada com gelatina, de modo a simular um compartimento liquefeito tri-dimensional sujeito a alterações de temperatura para avaliar a eficácia do comportamento das nanopartículas como sensores. Em suma, todos os resultados destacam o grande potencial das nanopartículas $Mn_xZn_{1-x}Fe_2O_4$ produzidas para nanotermometria.

keywords

Magnetic nanoparticles; Mn-Zn ferrites; Nanothermometers; Wireless sensors; Hyperthermia; Cryopreservation.

abstract

Magnetic iron oxide nanoparticles have gathered increasing attention from the scientific community over the years due to their promising features such as their *in vivo* biocompatibility, versatile surface modifications, and facile synthesis. With this in mind, temperature sensing comprises one of the most delicate areas of thermometry when applied to processes such as magnetic hyperthermia and cryopreservation, which strongly depend on minute temperature changes. In fact, gaining insight into the small temperature variations occurring at cellular scale is currently addressed using nanothermometers based on the well-defined temperature dependence of a given property. However, current approaches are mainly based on optical properties, being limited by several drawbacks, such as the inefficient penetration of light in many tissues, for example. In view to overcome this great challenge, magnetic nanoparticles have a huge potential, since they combine adequate size for cellular internalization and magnetic fields can easily penetrate tissues, enabling remote temperature monitorization.

In this context, the objective of this thesis is to develop stable Mn-Zn ferrite nanoparticles dispersed in aqueous medium to act as remote distance temperature sensors for bioapplications, in particular for hyperthermia and cryogenic applications.

$Mn_xZn_{1-x}Fe_2O_4$ NPs were successfully produced using two distinct methodologies, namely thermal decomposition, and a molten salt-assisted thermal decomposition approach. The prepared NPs were then analyzed by scanning Electron Microscopy (SEM), transmission electron microscopy (TEM), energy-dispersive X-ray spectroscopy (EDS), Fourier transform infrared (FT-IR) spectroscopy, dynamic light scattering (DLS), zeta potential, and magnetic properties. X-ray powder diffraction (XRD) successfully verified the presence of a cubic crystal structure with a predominant phase in the $Fd\bar{3}m$ space group of the Mn-Zn ferrites produced by both methodologies. FT-IR spectroscopy was used to assess presence of several compounds on the NPs surface, such as the functionalization of the particles with citric acid and EDTA. Moreover, Rietveld refinement was useful to discriminate the NPs sizes, which overall constituted diameters ranging from 5.9 to 15 nm by thermal decomposition methodology and 1.3 to 4.2 nm by molten salts methodology. Magnetization measurements were made to evaluate the potential of the NPs as magnetic nanothermometers, in which the 6.9 nm-sized $Mn_{0.30}Zn_{0.47}Fe_2O_4$ (sample TD9) nanoparticles exhibited magnetic reversibility between 100 to 375 K with a maximum sensibility of 2.9 $\%.K^{-1}$ at 225 K. In addition, the 8.0 nm-sized $Mn_{0.11}Zn_{0.78}Fe_2O_4$ (sample TD4) nanoparticles also revealed potential sensor applications between 300 and 400 K, with a maximum sensibility of 2.1 $\%.K^{-1}$ at 300 K. According to these findings, the produced NPs are deemed suitable for both hyperthermia and cryopreservation applications. Lastly, the encapsulation of these ferrofluids was carried out with gelatin, in order to simulate a 3-D phantom tissue to be subjected to temperature changes to assess the effectiveness of the behavior of the nanoparticles as wireless sensors. In sum, all the results highlight great potential in the hereby produced $Mn_xZn_{1-x}Fe_2O_4$ NPs for nanothermometry.

Contents

List of Figures

List of Tables

List of abbreviations

2-D	Two-dimensional
3-D	Three-dimensional
AC	Alternating Current
CPAs	Cryoprotective agents
CTAB	Cetyltrimethylammonium bromide
DBE	Dibenzyl ether
DC	Direct Current
D_c	Critical diameter
DIPA	Di-iso-propanolamine
DLS	Dynamic light scattering
DMSA	2,3-dimercaptosuccinic acid
DVB	Divinylbenzene
EDS	Energy dispersive X-ray spectroscopy
EDTA	Ethylenediaminetetraacetic acid
EPR	Enhanced permeability and retention
FC	Field-cooled
FT-IR	Fourier transform infrared
GMR	Giant magnetoresistance
HDO	Hexadecanediol
KPS	Potassium persulfate
LED	Light emitting diode
MFH	Magnetic fluid hyperthermia
MIONs	Magnetic iron oxide nanoparticles
MIPA	isopropanolamine
Mn-Zn	Manganese-zinc
MNPs	Magnetic nanoparticles
MPI	Magnetic particle imaging
MR	Magnetic resonance
MRI	Magnetic resonance imaging
NIR	Near infrared
NPs	Nanoparticles
OA	Oleic acid
OAm	Oleylamine

OSPE	Octahedral site preference energy
PEG	Polyethylene glycol
PEI	Polyethylenimine
PLGA	Poly(lactic-co-glycolic acid)
PNIPAAm	Poly(N-isopropylacrylamide
RT	Room temperature
SEM	Scanning electron microscopy
TEM	Transmission electron microscopy
TMAOH	Tetramethylammonium hydroxide
TOP	Trioctylphosphine
TOPO	Tri-*n*-octylphosphine
XPS	X-ray photoelectron spectroscopy
XRD	X-ray diffraction
ZFC	Zero-field-cooled

List of symbols

B_0	Static magnetic field
H	Magnetic field intensity
H_c	Coercivity
M	Magnetization
M_r	Remanent magnetization
M_s	Saturation magnetization
S_m	Maximum sensitivity value
T_B	Blocking temperature
T_C	Curie temperature
T_N	Néel temperature

The context

Temperature monitoring is a field of tremendous importance for various applications, such as hyperthermia and cryopreservation, for example. Conventional thermometers, although useful for many other practices, can only measure surface temperatures with precision and often suffer from needing cables in order to work. With this in mind, the development of wireless nanosized thermometers that can integrate biological environments provides an appealing and promising alternative. In fact, employing nanoparticles (NPs) capable of sensing temperature inside cells with a high spatial resolution would open new doors to the three-dimensional (3-D) temperature mapping of target tissues, and allow the real time assessment of a plethora of physiological processes that rely on strict temperature variations.

To this end, magnetic iron oxide NPs present themselves as potential candidates for the development of these nanothermometers, possessing optimal *in vivo* biocompatibility, tunable surface, ease of synthesis, as well as high chemical stability. In addition, through doping of these particles, their magnetic properties can be tuned, in a way that a temperature dependent magnetization is achieved at a desired temperature interval, thus serving as magnetic nanothermometers.

Hence, this thesis aims to produce magnetic $Mn_xZn_{1-x}Fe_2O_4$ NPs for potential application in the temperature monitoring of both hyperthermia and cryopreservation. This dissertation is organized into four chapters: general introduction, experimental part, results and discussion, and conclusions and future work. In the first chapter (Chapter 1), the fundamental theoretical concepts as well as a relevant review of literature regarding the preparation of materials of interest is presented. In the second chapter (Chapter 2), the materials and experimental procedures, as well as the characterization techniques used in this work are displayed. The third chapter (Chapter 3) presents the obtained results, their discussion and comparison with literature. Finally, the fourth chapter (Chapter 4) offers the main conclusions obtained in this work, as well as the proposed future work.

Chapter 1: General introduction

The biosphere can provide innumerous examples of systems displaying adaptive behaviors in response to external stimuli. For example, many creatures in nature use Earth's magnetic field for orientation and navigation.[1,2] These stimuli-responsive

mechanisms are of special importance to the scientific community, which aims to understand and explore them in hope of developing new strategies/solutions for a plethora of applications.[2] In this regard, advances in nanotechnology stand in the spotlight, giving insight the phenomena occurring at nanoscale that provide many new opportunities for the development and improvement of many devices, including solar cells, batteries, supercapacitors, actuators, carriers, and sensors.[3] Temperature is one of the most relevant parameters when it comes to sensing. When we think about temperature sensors, thermometers or thermocouples often come to mind, both of which generally present a well-defined response, although often limited to surface temperatures, or hindered by need to use wires. However, measuring temperature with a high spatial resolution at sub-micron lengths, for example, regarding intracellular temperature variations, becomes a challenge.[4,5] In this context, nanoscience shows enormous potential, allowing the design of devices that can penetrate cell membranes, and measure temperature in-depth and in a 3-D manner.

Hence, the idea occurred of having a nano-sized, stimuli-responsive system with magnetic properties strictly correlated to temperature variations, and therefore acting as a temperature sensor. Following a temperature change, the material's inherent magnetization would also change in a dramatic and precise manner. This change would be detected by another sensor and associated to a certain temperature, allowing non-contact/wireless temperature sensing for various applications such as hyperthermia and cryopreservation. In addition, these nano-sized systems are feasible to be incorporated by living cells, where they can monitor temperature where other conventional sensors could not, and thus study heat variations of several biological processes. These magnetic responsive elements would work as wireless sensors opening a new range of applications: *i)* determination of a previously unknown local temperature with high spatial resolution when the concentration of NPs is known and *ii)* measurement of the magnetic signal at different well-defined temperatures, where the concentration of NPs is unknown, both at a cellular scale.

The goal in mind is to be able to develop magnetic $Mn_xZn_{1-x}Fe_2O_4$ NPs dispersed in aqueous colloidal suspensions behaving as remote temperature sensors that explore an "on-to-off" variation in magnetization associated to a magnetic phase transition. Furthermore, these magnetic nanothermometers will be evaluated regarding temperature detection with high spatial resolution in a 3-D model system. To this end, local temperature changes can then be sensed at distance using a giant magnetoresistance (GMR) sensor or a fluxgate magnetometer, where the system is

calibrated with an externally controlled thermometer. After calibration, the temperature will be modified using a near infrared (NIR) light emitting diode (LED) and liquid nitrogen. In summary, the pivotal purpose is to develop magnetic NPs able to be explored as wireless temperature sensors.

1.1. Interest of nanomaterials in nanomedicine

Nanomaterials are generally defined as any material ranging of 1-100 nm, whose dimensions are compatible with biological molecules, as illustrated in Figure 1. According to their size, these nanomaterials can be categorized as *i)* nanoparticles (0D: all the dimensions are measured within the nanoscale), *ii)* nanowires or nanotubes (1D: one dimension is measured outside the nanoscale), and *iii)* nanofilms or nanolayers (2D: two dimensions are measured outside the nanoscale).[6]

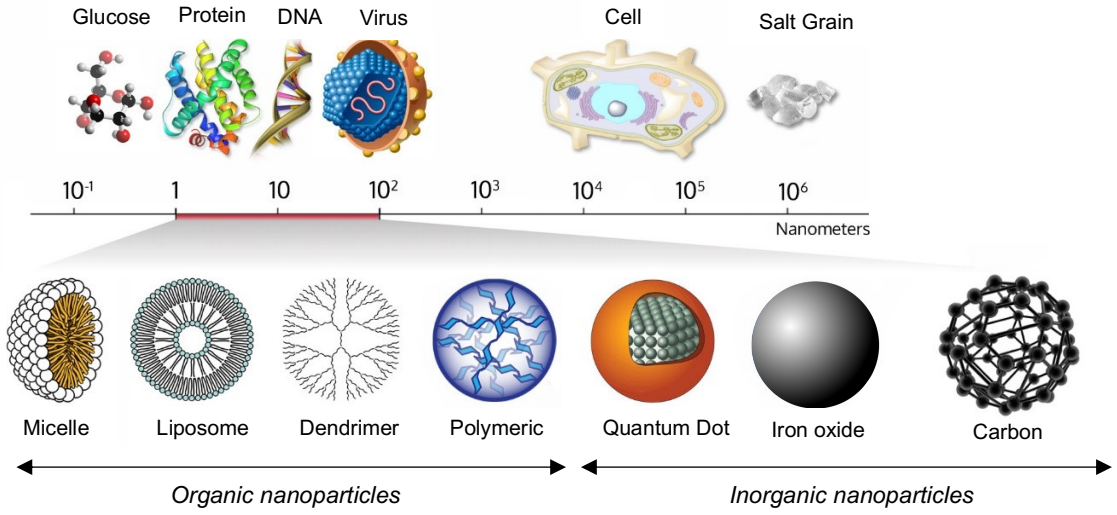

Figure 1. Schematic representation of both size comparison of nanoparticles with atomic nature and classification of nanoparticles according to its nature as well as some examples. Adapted from [7].

The chemical synthesis plays a critical role in tailoring the physical and chemical properties of the nanoparticles. According to their nature they can be classified into organic or inorganic nanoparticles as shown in Figure 1.[8,9] They can also present themselves in various shapes such as spheres[10–13], rods[8,12,13], wires[8,12,14], plates[8,13,14], stars[8,12,13], cages[8,14], multipods[8,13,15,16], among others.

In retrospect, it was in 1959, when the Nobel Prize Laureate Richard Feynman in his lecture "There's Plenty of Room at the Bottom", discussed the possibilities and potential benefits of the manipulation of materials at the atomic level.[17] This talk was a turning point and encouraged researchers to look at nanomaterials for completely new biomedical applications, such as exploring the potential of NPs in diagnostic accuracy

and treatment efficacy, while successfully dealing with the biological and evolutionary diversity of each being.[18] In comparison to their conventional bulk counterparts, at nanoscale, particles have unique properties such as, high surface-to-volume ratio, high surface energy, unique mechanical, thermal, electrical, magnetic, and optical behaviors, among others. These properties make them suitable for use in applications such as probes, delivery platforms, carriers and devices improved for disease detection, therapy and prevention.[8]

Understanding fundamental concepts about nanoparticles as well as their physical and chemical properties is crucial to optimize several parameters, as resumed in Figure 2, in order to successfully design NPs for biomedical applications.

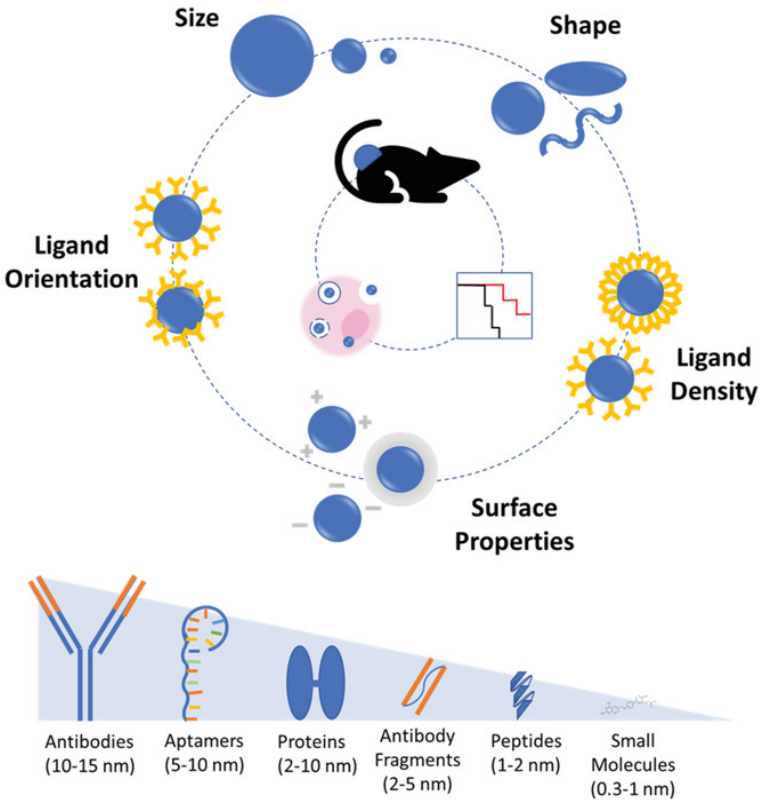

Figure 2. Schematic illustration of nanoparticle optimization parameters for biomedical applications. Physical and chemical properties upon delivery affect cellular accumulation, particle internalization and cargo delivery, and ultimately the therapeutic outcome. Sizes and targeting moieties are also summarized. Image reprinted from reference [19].

Recently, NPs synthesis and applications are very diverse and complex making it almost impossible to perform an overview on the subject without risking oversimplification. In this regard, size control is one of the most important parameters to manage in NPs synthesis. For example, when interacting with the cell membrane, very small NPs present limitations, as they can only interact with a fixed number of cell receptors. It is of common knowledge that there is an optimal NP size range of *ca.* 25-

50 nm in order to have efficient endocytosis.[20] Hence, for the viable use of NPs as a biomedical platform, both scientifically and economically, it is essential to develop successful synthesis protocols that guarantee a homogeneous size distribution of NPs that fits into the required size interval for their intended application. However, control over size distribution is not fully understood yet, although it is widely accepted that a nucleation and growth mechanism must occur.[21] Alongside these developments, an increased interest on magnetic nanoparticles (MNPs) has arisen mainly due to the application of magnetic properties at nanoscale. In a more practical example, macroscopic materials may contain more than 10^{23} atoms and their magnetic properties are described by solid-state physics. However, at nanoscale, a material, such as a MNP, is composed by several hundred to 10^5 atoms, making magnetic properties differ from their bulk form.[18] Generally speaking, almost all properties become size dependent which prompts one to conclude that with efficient size control, it is possible to synthetize nanomaterials that exhibit the specifically required properties. In other words, the effective combination of nano-sized particles with unique magnetic properties results in nanomaterials with added value and potential for biomedical applications.

1.2. Magnetic properties

Magnetism is a phenomenon whose discovery dates back to antiquity, confirmed in 1819 by Oersted, in which a magnetic field is created whenever an electric charge is in motion.[22] This can be originated either from the movement of electrons in an electric field, from the constant subatomic movement of electrons and also from their spin. Since all matter has electrons, it can be stated that every material is influenced by the presence of magnetic fields. From the atomic view of matter, there are two types of electronic contribution to magnetism: *i)* orbital; and *ii)* spin. These types of electronic motion are the sources of the macroscopic magnetic phenomena in materials. Orbital refers to the orbit of an electron around an atom, creating a magnetic moment due to the fact that an electron is a moving charge.[22,23] Spin, in turn, generates spin moment, consisting of an electron intrinsic property, since each electron rotates along its own axis, as illustrated in Figure 3.[22,23] The net magnetic moment of an atom can be described as the sum of the magnetic moments, from both electron motions of all the constituent electrons. However, there are moment cancellations arisen from opposite moment directions that cannot be dismissed. It is important to highlight that materials composed of atoms with completely filled electron shells do not present a net magnetic moment.[22,23]

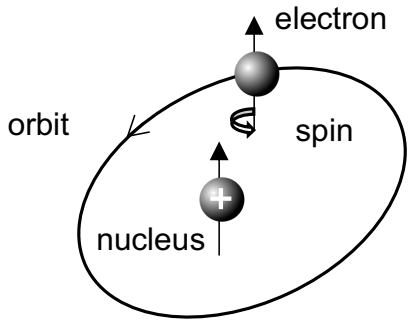

Figure 3. The electronic motions about the nucleus of an atom. Adapted from [23].

1.2.1. The classifications of magnetism

It should be noticed that there are many types of magnetism in bulk materials, where the most common are diamagnetism, paramagnetism and ferromagnetism, whereas anti-ferromagnetism and ferrimagnetism are considered subclasses of ferromagnetism (Figure 4). The classification is based on the arrangement of electron and atomic magnetic dipoles when an external magnetic field is applied, the latter usually designated by *H*.[22–24]

Diamagnetism does not exhibit magnetic dipoles in the absence of magnetic field, but they generate weak magnetic dipoles in opposite direction to that of the external applied field. Some diamagnetic materials are mercury, zinc and silver, for example. In paramagnetism, randomly oriented dipoles are present in the absence of a magnetic field and free to rotate, whereas upon application of an external magnetic field, they preferentially align in the same direction of the external field. Paramagnetic materials are considered aluminum, sodium and titanium, for example.[23] Regarding ferromagnetism, some magnetic materials exhibit permanent magnetic dipoles in the absence of an external magnetic field, possessing large permanent magnetizations. Transition metals such as some phases of iron, along with cobalt and nickel, for example, display ferromagnetic behavior.[23] This kind of behavior is related to atomic magnetic moments derived from uncanceled electron spins. In addition, coupling interactions make net spin magnetic moments of the neighboring atoms to align with each other, even without an external magnetic field. It is noteworthy to specify that the origin of coupling interactions is not fully understood but it is believed that it occurs due to the structure of metal.[23] In case of antiferromagnetism, the coupling results in an antiparallel alignment of neighboring dipoles, in which magnetic moments cancel each other in the absence of a magnetic field. Consequently, antiferromagnetic materials as a whole do not possess net magnetic moment, for example a ceramic material such as manganese oxide.[23] In the

case of ferrimagnetic materials, these display some weak dipoles that are aligned in an anti-parallel way to the neighboring stronger dipoles when a magnetic field is absent. However, these magnetic moments have different magnitudes and consequently the incomplete cancellation of magnetic moments of ferrimagnetic materials results in net magnetization. Cubic ferrites such as magnetite (Fe_3O_4) seem to follow such behavior, for example.[23]

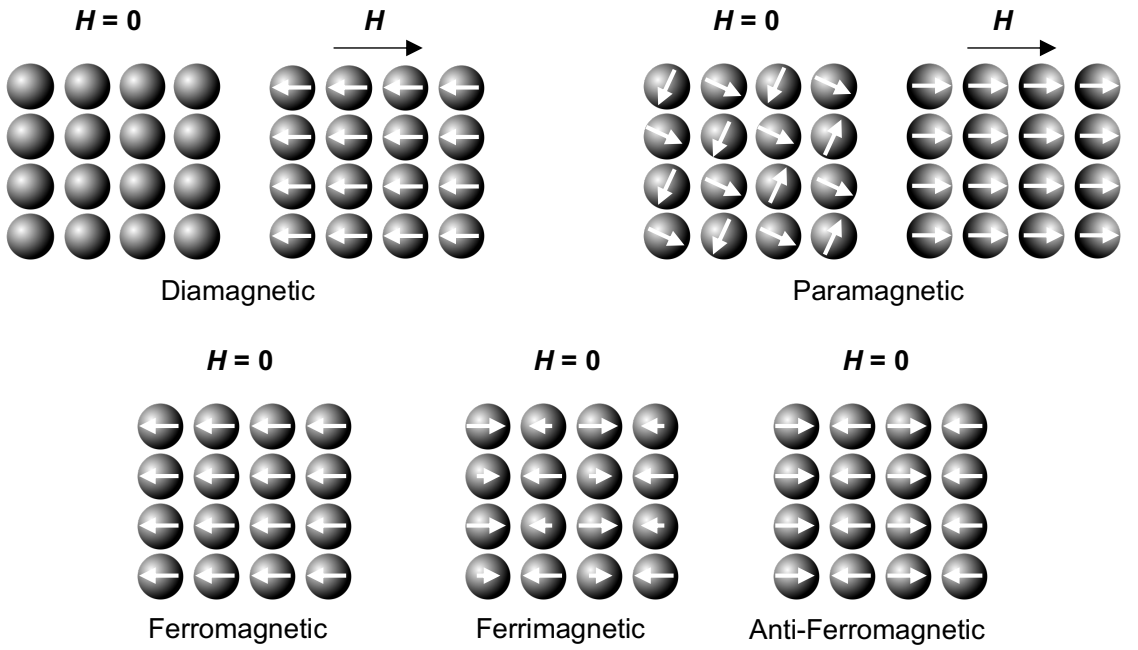

Figure 4. Schematic representation of the atomic magnetic dipole arrangement in absence and presence of an external magnetic field (H). In this image atoms are represented as black dots while the arrows represent atomic dipole moments. Adapted from [23].

1.2.2. The influence of temperature on magnetic behavior

Temperature is a factor that can change the magnetic properties of materials. As temperature increases, the magnitude of thermal vibrations of atoms also increases, causing magnetic moments to be free to rotate. Therefore, with increasing temperature, an elevated thermal motion of the atoms usually leads to the randomization of the directions of previously aligned moments. For the sake of simplicity, only ferro- and ferrimagnetic materials will be considered in the following discussion. In these materials, the atomic thermal motions compete with the spins alignment, whether an external magnetic field is present or not, resulting in a decrease of the maximum value of magnetization that can be reached, known as the saturation magnetization, M_s. Knowing this, M_s generally reaches its maximum at 0 K, where thermal vibrations are minimal. However, increasing temperature leads to a decrease of M_s followed by a sudden drop to zero at what is known as Curie temperature, T_C. Below T_C, in ferro- and ferrimagnetic

state, temperature is not sufficiently high to counteract the coupling forces between the magnetic moments, however, rising of the temperature weakens the overall magnetization, overcoming the mutual spin-coupling forces. Hence, these materials display paramagnetic behavior.[23]

1.2.3. Domains and hysteresis

In the previous section was mentioned that, below T_C, any ferro- and ferrimagnetic material is composed of regions possessing uniform magnetization. These regions called domains are separated by domain boundaries. In magnetic materials of large size, it is well known that there is a multi-domain structure, in which each domain may have different magnetization orientations.[15,21,23] The formation of these domain boundaries is a process influenced by the balance between *i)* the magnetostatic energy, which increases proportionally with the volume of the materials, *ii)* the magnetic anisotropy energy, which depends essentially on the material, and the domain wall energy, which in turn increases in proportion to the interfacial area between the domains.[15,21,23]

By monitoring the magnetic properties and the temperature-dependent behavior of these materials it is possible to conclude that if ferro- and ferrimagnetic materials are initially unmagnetized, but if a sufficiently strong magnetic field is applied, it causes domains within a material to align according to the field. However, there is a residual magnetization that remains in the applied field direction even at zero field. The value for this magnetization is known as the remanent magnetization, M_r. This phenomenon causes the hysteresis effect, characterized by sigmoidal shape of the *M-H* curve, also known as hysteresis loops, which are a measure of magnetization (*M)* against the magnetic field intensity (*H*), illustrated in Figure 5. Thus, the M_r is only lost by heating the ferromagnet above the T_C or by applying a magnetic field in the negative direction with enough intensity to bring the magnetization of the sample back to zero (also known as the coercivity, H_c).

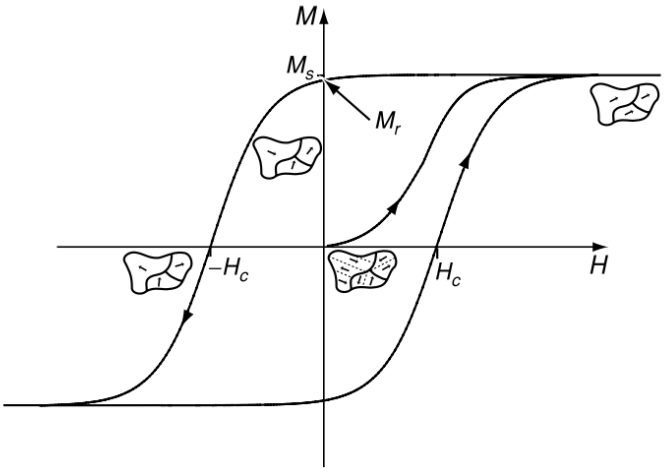

Figure 5. Magnetic hysteresis diagram of a ferromagnetic material. Image reprinted from reference [22]*.*

According to hysteresis characteristics, ferro- and ferrimagnetic materials can be classified as “soft” or “hard” materials, as depicted in

Figure 6. In sum, soft magnetic materials possess a net magnetic moment that can be easily altered according to an external field, thus exhibiting low H_c. On the other hand, the net magnetic moment of hard magnetic materials is difficult to change in the presence of an external field and therefore exhibit a high H_c and M_s.[22–26]

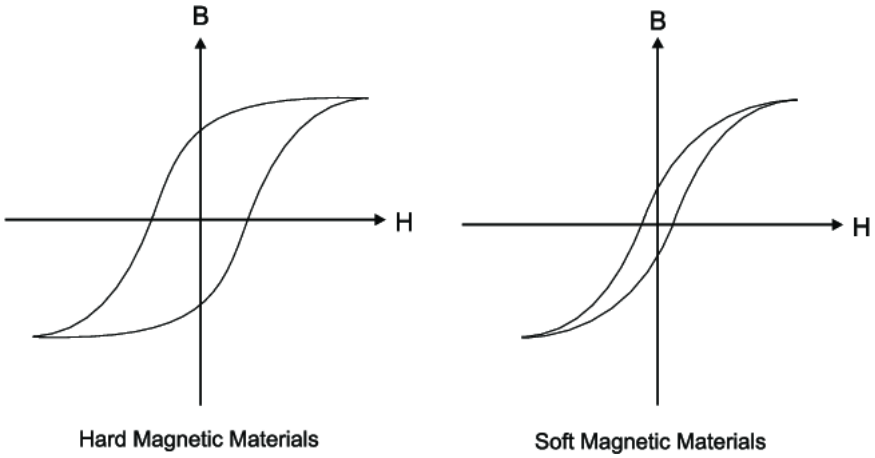

Figure 6. Schematic depiction of a) hard and b) soft magnetic materials as well as their hysteresis characteristics. Image adapted from [27]*.*

Regarding nanoscale materials, there is a critical volume below which it is more energetically expensive to create a domain wall. For instance, the entire material becomes a magnetic domain, *i.e.*, a single domain.[15,21,23,26] This is called the critical diameter or critical size (D_c), which is dependent on the material and is also influenced several anisotropy energy terms.[15,21,26]

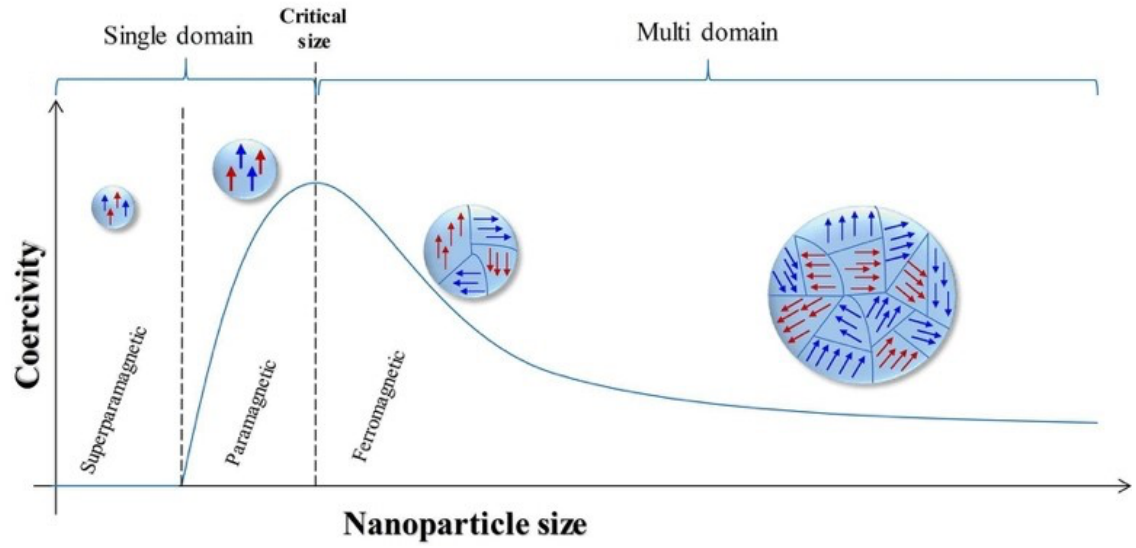

Figure 7. The effect between particle size, coercive field and magnetic domain structures (dipoles are represented by blue and red arrows). Image reprinted from reference [18].

At smaller sizes, below D_c, as shown in Figure 7, the phenomenon of superparamagnetism can be observed. In superparamagnetism, thermal energy may be enough to change the magnetization of the whole particle, while the individual atomic moments maintain their ordered state with respect to each other.[15,28] This implies that the magnetic moment of superparamagnetic nanoparticles will be zero at high enough temperatures, in the absence of a magnetic field. Such behavior is marked by the lack or negligible M_R after the applied field is removed, thus enabling colloidal stability and avoiding agglomeration.[15,28–30] However, some particles can become blocked (the magnetic spins do not flip after the external magnetic field is removed), thus becoming permanently magnetized. The temperature below which blocking occurs is known as "blocking temperature", T_B, which depends on the anisotropy constant, the size of the particles, the applied magnetic field, and the experimental measuring time.[15,29] Typically, T_B can be experimentally determined through several criteria, like for example, merging the point of zero-field-cooled (ZFC) and field-cooled (FC) magnetization curves or the maximum of the ZFC curve, as shown in Figure 8.[15,24,29] However, T_B obtained by the maximum of the ZFC curve is only reliable assuming that the sample is formed by NPs with a similar size. Consequently, an accurate value of T_B should rely in the merging point of ZFC/FC measurements by determination of the distribution of energy barriers.[31]

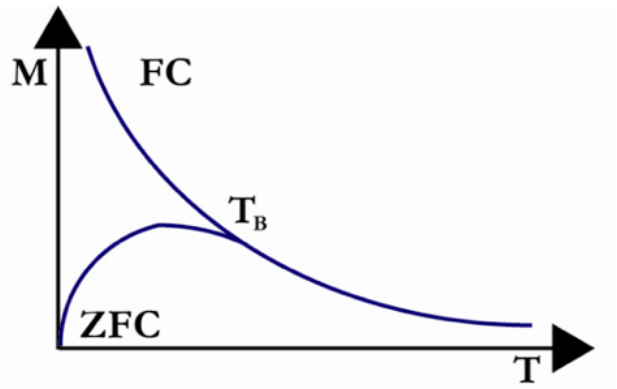

Figure 8. Relation between blocking temperature with hysteresis curve. Image adapted from [32].

The mechanisms of superparamagnetism were explained by Néel and further studied by Brown. The findings are founded on an activation law for the relaxation time of the net magnetization of the particle given by the Néel-Brown relaxation. In this context, if the particle magnetic moment is able to fluctuate across the energy barrier, the system is classified unblocked, otherwise, it is in the blocked state.[15,29,33] In order to align with an external magnetic field, MNPs must overcome the anisotropy barrier, *i.e.*, at a finite temperature where there is a probability for the magnetic moment flip and reverse its direction , as illustrated in Figure 9.[15,29]

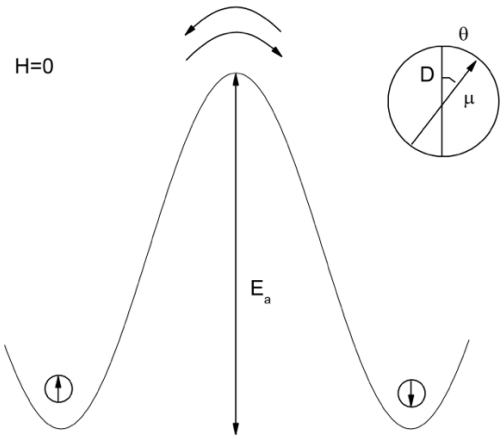

Figure 9. Visual representation of the energy barrier for uniaxial anisotropy at zero external field. Image reprinted from [33].

More precisely, Néel relaxation refers to the process for a magnetic vector to "flip" between its energy minima due to thermal fluctuations, or in other words, it occurs when thermal energy overcomes the anisotropy energy barrier, leading to a rotation of an internal magnetic moment, instead of a physical rotation. In contrast, Brownian relaxation is characterized essentially by the vector fluctuation around the energy minima, then

jumping and fluctuating around the other energy minima due to the viscous forces related to the physical rotation with respect to surrounding fluid. In this model, time is determined by the rotational mobility of the particles.[15] In Figure 10 both types of relaxation in the presence of an external field are represented.

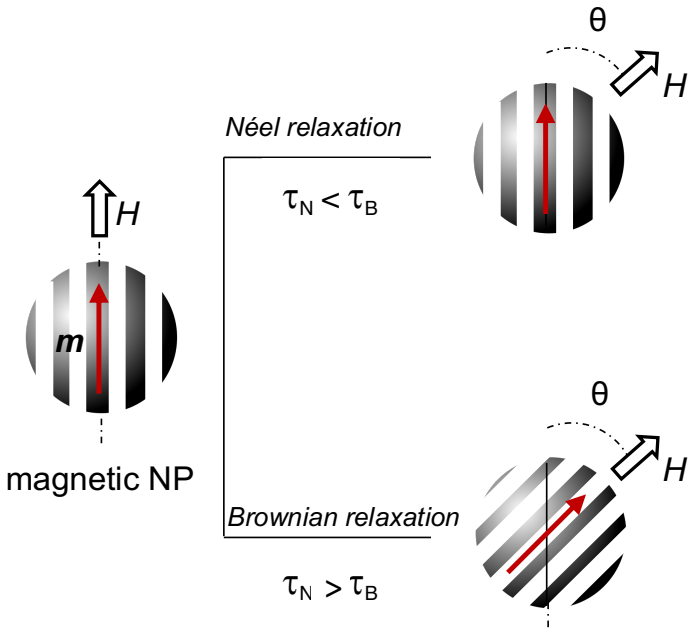

Figure 10. Schematic illustration of Brownian-Néel relaxation from magnetic NPs in the presence of an external field (H). Néel relaxation refers to the rotation of the moment within the MNP when the anisotropy energy barrier is overcome, whereas Brownian relaxation involves mechanical rotation of the MNPs. Adapted from [34].

After having discussed the presented aspects of magnetism, its application in temperature sensing can now be properly addressed in the following chapter.

1.3. Magnetic temperature sensors

Sensitive probing of temperature variations at micro- and nanoscale is crucial in countless areas of modern science and technology such as cancer hyperthermia and temperature controlled drug delivery.[35–37] Conventional thermometers, however, suffer from serious drawbacks such as: *i)* being usually invasive[38], *ii)* allowing only single point temperature measurements[38], *iii)* the need to be connected using cables[39], *iv)* being limited to measure surface temperatures[35,39] *v)* and being susceptible to interfere with the therapeutic and imaging instruments[38,40,41]. With this in mind, development of nanothermometers capable of sub degree temperature measurements with a high spatial resolution over a large range of temperatures, as well as being capable to be integrated within a living system are of utmost importance.[37,42] This would create many new possibilities ranging from thermally controlled drug delivery[35,43–45], monitoring

temperature-dependent activities at a cellular level[35,42,43], gene expression[35,37,44], hyperthermia treatment[35,43–46] to circuit monitoring.[37,42,43] Precise local temperature measurements could provide a powerful insight into the impact of temperature in intracellular components during cell metabolism[35,37,43], as well as on electronical performance[43]. Moreover, it could be useful in the detection of certain tumors and inflammations.[38,40] In fact, an abnormality in intracellular temperature is often and indicator of cellular dysfunction, for example, it is known that cancerous cells display higher temperature, when compared to normal cells due to their increased metabolism.[42] Triggered by such urge, a nanoscale thermometer for probing cellular compartments should comprise certain properties, such as: *i)* real-time assessment[45,47,48], *ii)* accurately estimation of temperatures noninvasively[35,36,44], *iii)* the ability to perform remotely 3-D temperature measurements[38,44] and *iv)* biocompatibility[44].

To date, ultrasound, optical, and magnetic approaches for *in vivo* temperature probing have been proposed.[5,35,36,41,43–45,49,50] However, ultrasound temperature estimation is rendered difficult due to the difference of density between bones and organs.[49] The drawbacks of optical approaches are the limited penetration of light into deep tissues because of optical complexity of different body tissues[5,38,44], difficulty in stimulating and detecting the signal[38,44,50], and the possibility of increased healthy tissue damage or unwanted apoptosis if under intense illumination[44,45] In addition, temperature detection *in vivo* can be hindered by the significant absorption and scattering of ultraviolet and visible light by physiological tissues.[45,50] To address this issue, probes with absorption and emission in the NIR were suggested.[45,49] However, this leads to an increase in cost and complexity of the detections systems, with no improvement regarding targeting and detection in deep tissues due to the low accessibility of the irradiated regions.[45,49] Therefore, the particular interest in magnetic thermometry arises from the potential for noninvasive, real-time and remote measurement of temperature with precision within biological nanoscale environments.[26–28,33] In this context, MRI-based thermometry and MNPs-based thermometry arise as suitable approaches due to the fact that both are strongly temperature dependent and magnetic fields interact weakly with biological molecules, thus the ability of penetrate deep into the body.[36,40,48,51,52] However, magnetic resonance (MR) thermometers are not fit to measure environments that do not contain water,[51] such as adipose tissue, and may suffer from signal dampening due to motion artifacts, as well as from heterogeneity of the static magnetic field, B_0. Also, the main drawback is only being able to measure the temperature close to the transition temperature, exploring an “on-to-off” magnetization rather than

temperature range.[36,40] On the other hand, MNPs-based thermometry for *in vivo* applications does not suffer from the aforementioned limitations. In fact, employing the temperature sensitivity of the MNPs magnetization and relaxation time under Alternating Current (AC) and/or Direct Current (DC) magnetic fields allows precise temperature determination.[43,44,46,51]

With this in mind, sub-micron high-resolution thermometry constitutes an area of special interest for this thesis. Herein, a general outline of developed systems for this end, along with their working temperature ranges and sensitivity will be presented here. There is a rich variety of systems designed to sense temperature at nanoscale, however, the magnetic thermometers highlighted in this review will not necessarily comprise the same exact applications as the systems developed in this thesis. In the following examples, the sensitivity of developed magnetic particles was estimated using the graphics present in each paper, in order to provide a comparison basis. In the following examples, the sensitivity of developed magnetic particles was estimated using the merging points of the ZFC-FC curves present in each paper, in order to provide a comparison basis regarding the sensitivity of different materials if they were to be employed as thermometers. It is important to clarify that all the following maximum sensitivity (S_m) values, as well as the temperature intervals obtained here are merely approximations and therefore do not reflect the findings in each corresponding paper.

As a starting point, in 2009 Ivanovskaya and co-workers reported crystalline spheric $Mn_{0.5}Zn_{0.5}Fe_2O_4$ particles with a diameter ranging from 600 to 800 nm in order to study the effect of synthesis temperature of the as-prepared particles *via* spray pyrolysis methodology. Reversibility of the temperature dependence of magnetization is demonstrated between *ca.* 350 to 375 K, with a S_m = 6 %.K^{-1} in the aforementioned temperature range.[53] In 2013, Yang *et al.*[54] synthesized nonstoichiometric zinc ferrite particles through thermal decomposition route to understand how the presence of surfactants would influence the doping process. Simply put, $Zn_{0.387}Fe_{2.613}O_4$ NPs with different sizes, such as 26.5 and 13.4 nm, were produced. The former can work as a sensor from 250 to 300 K with a S_m = 2 %.K^{-1} at 250 K, as well as a M_s of 56 emu.g^{-1}. As for the latter, reversibility is demonstrated to be between 150 to 300 K with a S_m = 0.6 %.K^{-1} at 150 K. As stated by the authors, these particles showed promising features for biomedical applications, suggesting their use as hyperthermia agents.[54] The effect of the presence of surfactants was also later studied by Szczygieł *et al.*[55] combining coprecipitation and sol-gel autocombustion methods. The prepared nanocrystalline $Mn_{0.65}Zn_{0.35}Fe_2O_4$ ferrite particles could work as a sensor between 400 to 450 K, with S_m

= 1.4 %.K^{-1} at 400 K. However, the authors of this work suggest further exploring and improving their methodology in order to employ these particles as catalysts.[55] Regarding the synthesis of doped ferrites as well as the understanding of the correlations between chemical composition and MR signal enhancement, Zhang and his team reported monodisperse $MnFe_2O_4$ particles with sizes smaller than 4 nm *via* thermal decomposition technique. In the case of the 3.9 nm NPs, these presented sensor behavior within the temperature interval of 25 to 50 K, with S_m = 4.0 %.K^{-1} at 25 K. As for the 3 nm-sized NPs these showed sensor potential in the temperature range of 15 to 50 K, with S_m = 0.5 %.K^{-1} at 20 K. Now regarding the 2 nm sized NPs, these could work as a sensor from 5 to 50 K, being S_m = 8.0 %.K^{-1} at 5 K.[56] In another study seeking the understanding of intrinsic loss power towards hyperthermia therapy, Phong *et al*. reported the synthesis of $Mn_{0.5}Zn_{0.5}Fe_2O_4$ particles prepared by hydrothermal route. As such, 15 nm-sized crystalline NPs revealed promising features as a sensor between 184 to 400 K with a S_m = 4.4 %.K^{-1}.[57] More recently, in 2020 Almessiere *et al*. reported the synthesis of $Mn_{0.5}Zn_{0.5}Fe_{2-2\varkappa}(Dy_\varkappa Y_\varkappa)O_4$ particles prepared by both sol-gel combustion and sonochemical methodology, highlighting the beneficial properties of ultrasonic irradiation. Particles prepared by sol-gel combustion ($\varkappa$ = 0.00) showed potential as a sensor from 65 to 325 K with a S_m = 0.6 %.K^{-1} at 100 K, whereas for ($\varkappa$ = 0.02), the same could be verified from 275 to 325 K with a S_m = 0.4 %.K^{-1} at 275 K, and lastly for ($\varkappa$ = 0.05), which also displayed promising sensor behavior from 300 to 325 K with a S_m = 0.7 %.K^{-1} at 300 K. Using a different methodology, his team also prepared NPs by sonochemical methodology, where the following displayed sensor potential: ($\varkappa$ = 0.00) within 78 to 325 K with a S_m = 10 %.K^{-1} in 100 to 150 K, ($\varkappa$ = 0.02) from 77 to 325 K with a S_m = 4 %.K^{-1} in 175 to 250 K, and finally ($\varkappa$ = 0.05) from 63 to 325 K with a S_m = 6.2 %.K^{-1} in 100 to 150 K. In spite of focusing on studying these methodologies, authors also reported that their NPs possessed an inhibitory effect on cancer and bacterial cells, whereas, no inhibitory action was observed on normal healthy cells, being suitable for applications in this field.[58] To summarize, an overview of developed systems with potential for thermometry are presented in Table 1.

Table 1. Overview of magnetic particles displaying the maximum relative sensitivity values (S_m, %.K^{-1}), the temperature range (ΔT, K), the temperature or range of temperatures at which S_m is maximum (T_m, K) and observations associated with each example.

Thermometers	S_m (%.K^{-1})	ΔT (T_m, K)	Observations	Ref.
Fe_3O_4_MIPA	3.2	250-375 (*325-350*)	All NPs were prepared by aqueous coprecipitation methodology for biomedical applications.	59
Fe_3O_4_DIPA	1.4	100-375 (*250-375*))		
Fe_3O_4_NaOH	0.64	250-375 (*250-375*)		
$CoFe_2O_4$_MIPA	0.56	250-375 (*250-375*)		
$CoFe_2O_4$_DIPA	0.60	225-375 (*225-375*)		
$CoFe_2O_4$_NAOH	-	-		
$MnFe_2O_4$_MIPA	2.0	150-375 (*325-375*)		
$MnFe_2O_4$_DIPA	2.8	250-375 (*325-375*)		
$MnFe_2O_4$_NaOH	-	-		
$ZnFe_2O_4$	0.92	50-300 (*50-75*)	Ferrofluids were prepared according to the ionic ferrofluid process developed by Massart and colleagues[60], with few modifications.	61
$Mn_{0.5}Zn_{0.5}Fe_{2-2x}(Dy_xY_x)O_4$			Prepared by sol-gel combustion and sonochemical methodologies for antibacterial and anticancer applications.	58
Sol-gel:				
$\varkappa$ = 0.00	0.60	65-325 (*100-150*)		
$\varkappa$ = 0.02	0.40	275-325 (*275-325*)		
$\varkappa$ = 0.05	0.70	300-325 (*300-325*)		
Sonochemical:				
$\varkappa$ = 0.00	10	78-325 (*100-150)*		
$\varkappa$ = 0.02	4.0	77-325 (175-250)		
$\varkappa$ = 0.05	6.2	63-325 *(125-250)*		
β-FeOOH	0.0020	250-300 (*250-300*)	Prepared by annealing of SiO_2@β-FeOOH nanorods.	62
ε-Fe_2O_3	0.40	150-300 (*150-300*)		
$Zn_{0.387}Fe_{2.613}O4$			Prepared *via* thermal decomposition methodology for *in vivo* cancer therapy.	54
- 25.6 nm	2.0	250-300 (*250-300*)		
- 13.4 nm	0.6	150-300 (*150-300*)		
$MnFe_2O_4$	0.4	100-200 (*100-150*)	Prepared by thermal decomposition methodology for magnetic hyperthermia applications.	63
$MnFe_2O_4$@$CoFe_2O_4$	-	-		
$MnFe_2O_4$@$CoFe_2O_4$@$NiFe_2O_4$	0.2	250-300 (*250*)		
Fe_3O_4	10	50-375 (*250-300*)	Prepared by a classical one-pot thermal decomposition route for theragnostic applications.	64
$La_{0.75}Sr_{0.25}MnO_3$	1.4	320-340 (*320*)	Synthetized by molten salts methodology for biomedical applications.	65
$La_{0.53}Sr_{0.47}MnO_3$	1.4	275-310 (*275-300*)		
Fe_3O_4	18	300-400 (*300*)	Thermal decomposition methodology in the presence of oxygen.	66
$La_{0.67}Sr_{0.33}MnO_3$	0.65	225-300 (*225*)	Molten salts methodology to assess its suitability for the designing of several manganite perovskite nanocrystals.	67

$Ni_{0.5}Zn_{0.5}Fe_2O_4$ $Mn_{0.5}Zn_{0.5}Fe_2O_4$ $Ni_{0.5}Mn_{0.5}Fe_2O_4$	2.5 2.4 1.1	12-300 (*12-50*) 25-300 (*50-100*) 15-300 (*15-50*)	Synthetized by the reverse micelle technique.	68
$Zn_{0.05}Fe_{2.95}O_4$	0.42	340-400 (*340-400*)	Prepared by thermal decomposition methodology of a mixture of zinc and iron oleates for use as a spintronic material.	69
$Mn_{0.3}Mg_{0.2}Co_{0.5}Fe_2O_4$ $Mn_{0.3}Mg_{0.2}Zn_{0.5}Fe_2O_4$	- 6.0	- 200-400 (*300-400*)	Prepared by glycol-thermal reaction.	70
$ZnFe_2O_4$	13	16-400 (*16-50*)	Synthesized through a facile coprecipitation methodology.	71
$Zn_{0.3}Mn_{0.3}Ni_{0.2}Fe_{2.2}O_4$	1.2	300-350 (*320*)	Synthetized by coprecipitation methodology.	32
Fe_3O_4 - 7 nm - 15 nm - 23 nm	 0.04 0.03 0.02	 250-300 100-300 20-300	Synthesized by thermal decomposition methodology for magnetic hyperthermia applications.	72
$Co_xFe_{3-x}O_4$ - 7.2 nm	0.06	250-300 (*300*)	Prepared by thermal decomposition for magnetic nonvolatile memory applications.	73
$Zn_yFe_{1-y}O@Zn_xFe_{3-x}O_4$ [Zn]/[Fe]= 0.6 [Zn]/[Fe] = 10	 0.025 0.24	 275-300 (*275-300*) 175-300 (*175-300*)	Prepared by thermal decomposition methodology.	74
$Mn_xFe_{3-x}O_4$ $Mn_xFe_{3-x}O4$@PLGA	0.10 0.15	200-300 (*240-300*) 170-300 (*170-300*)	Synthetized by thermal decomposition methodology for nanomedicine applications as nanocarriers with magnetic functionalities, *i.e.*, magnetic heating.	75
Fe_2O_4 $MnFe_2O_4$ $CoFe_2O_4$ $NiFe_2O_4$ $ZnFe_2O_4$	0.050 4.9 4.7 5.7 7.0	100-300 (*100-200*) 55-300 (*55-100*) 225-300 (*225-300*) 20-300 (*20-100*) 15-300 (*15-50*)	Prepared by microwave-assisted rapid synthesis in 1-dodecanol for various technological applications such as magnetic data storage, catalysts, and sensors.	76

MIPA: isopropanolamine, DIPA: di-iso-propanolamine, NaOH: sodium hydroxide, SiO_2: silica; PLGA: poly(lactic-co-glycolic acid)

1.3.1. Hyperthermia

Hyperthermia is a promising approach for tumor treatment based on controlled heating of the malignant tissue in order to increase the sensitivity of cancer cells to other treatments or induce the destruction of the tissues directly.[77,78] In addition, there are alternative direct mechanisms to promote cell death, including *i)* denaturation, *ii)* folding, aggregation of proteins, and *iii)* coagulation. Also, there is an indirect response in which

the overexpression of heat shock proteins that promote the activation of the immune system and inflammatory response, which in turn suppresses tumor cells.[24,79–81]

Temperature increase can be achieved by using different strategies such as ultrasound, microwaves or infrared radiation.[64,82] The mechanisms of cell death involving this approach include either apoptosis or necrosis in a temperature-depending manner.[79–81] Hyperthermia therapy can be classified based on the temperature reached during the treatment, namely thermal ablation, moderate hyperthermia, and diathermia.[24] Thermal ablation occurs above 50 ºC leading to tissue necrosis, resulting in serious inflammatory and immune responses, which are undesirable.[79,83] Moderate hyperthermia, usually referring to hyperthermia treatment itself, aims to treat cancer in a temperature range of *ca.* 40 to 44 ºC. At this temperature cell death occurs by denaturation, as well as aggregation of intracellular proteins, without damaging the adjacent healthy tissues.[78,79,84,85] As for diathermia, it occurs at temperatures below 40 ºC and is useful for treating rheumatic diseases by physiotherapy.[24] With this taken into account, the issue lies in accurately probing the amount of heat provided in these treatments, or in other words, knowing the exact temperature the target tissues are being subjected to. This underlines the importance and need for the development of wireless sensors capable of being embedded into the tissues, even within living cells (Figure 11).

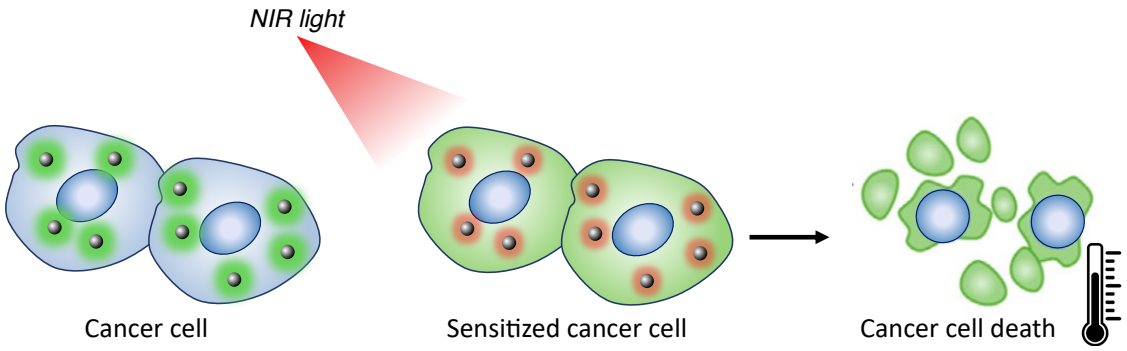

Figure 11. Measurement of temperature at which occurs cell death by using a NIR LED light. Image adapted from reference [34].

The success of hyperthermia is linked to physiological differences between normal and cancer cells. Cancer cells are more susceptible to the increase of temperature than normal cells due to their high rate of metabolism.[24,77] On a tissue level, rapidly growing tumors exhibit several common physiological marks, such as, hyper vasculature, enhanced vascular permeability, and decreased lymphatic drainage. The angiogenic tumor blood vessels possess an abnormal architecture that shows enhanced permeability and retention (EPR) effect: the tendency for systematically administrated

macromolecules within a 10 – 200 nm size range to be accumulated in solid tumors, thus decreasing their ability to dissipate heat stress.[19,78,86] EPR effect is illustrated in Figure 12.

Regarding the general definition of hyperthermia therapy, three different types of approaches can be described based on the location of the affected tissue: local hyperthermia, regional hyperthermia, and whole-body hyperthermia. Local hyperthermia involves heating a small area of tissue such as a tumor, while for regional hyperthermia a large area of tissue such as a whole organ is heated. As for whole body hyperthermia, it involves heating the whole body for treatment of metastatic cancer.[24]

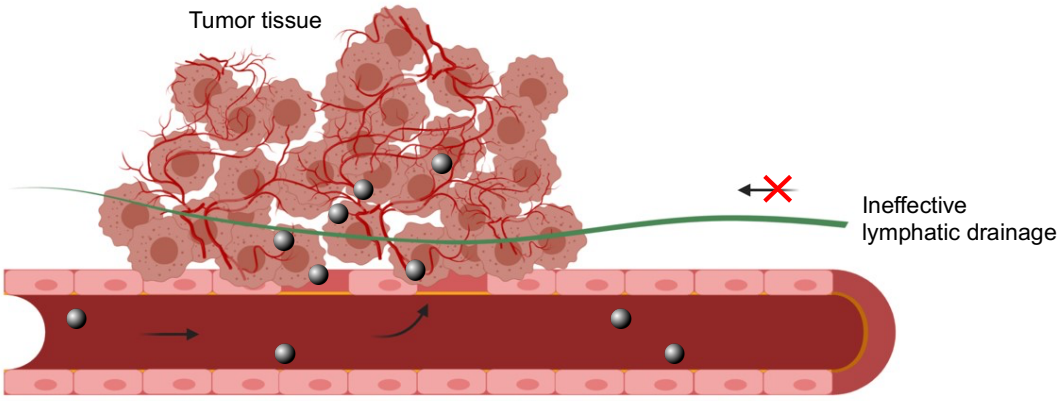

Figure 12. Representation of the enhanced permeability and retention (EPR) effect due to physiology of tumor site, including increased vascular permeability and ineffective lymphatic drainage. Adapted from [86,87] *using Biorender.com.*

1.3.2. Cryopreservation

Cryopreservation is an approach for long-term storage of cells or tissues by cooling them to cryogenic temperatures in order to slow or complete cease biological activity.[88,89] Long-term preservation of cells or tissues essentially consists in a slow freezing procedure, often carried out in a specialized container at -80 ºC, where the cells are cooled, then plunged into liquid nitrogen (*i.e.* ~150 ºC) or electronic freezers (*i.e.* ~160 ºC), until they are thawed for use at the desired circumstance.[88,90,91] The current practice relies in either slow-freezing or vitrification in the presence of cryoprotective agents (CPAs). In the slow-freezing approach, biopreservation occurs at low freezing rates, allowing dehydration in a controlled manner while avoiding intracellular ice formation in order to minimize cell membrane damage and cytoskeleton damage.[88,92] However, this approach is time consuming and requires a specific cooling rate accordingly to different types of cells.[89,93,94] Vitrification, on the other hand, employs high freezing rates and high CPA concentrations, transforming cells into an amorphous state

to completely avoid ice formation.[91] Unfortunately, high levels of CPA may cause uncontrolled differentiation as well as reduced viability due to their inherent toxicity.[88,94] Vitrification shows great promise for tissue preservation, however two major challenges concerning the rewarming of large volumes have been proven difficult to overcome.[95,96] First, an ultra-rapid heating rate is crucial to avoid devitrification and recrystallization, thereby preventing ice formation during the warming.[91,96] On the other side, achieving uniform heating rates throughout the whole volume in large samples through convective heating, generally by immersion the sample in a water bath at 37 ºC, is associated with non-uniform heat distribution, inducing large thermal gradients that often leads to thermal stresses causing fractures or cracks.[88,89,91,92,95,96]

For these reasons, the development nanosized magnetic temperature sensor that would allow the 3-D temperature mapping of a bulk sample would greatly improve our understanding and control over processes which heavily rely on small temperature changes. To this end, magnetic iron oxide nanoparticles (MIONs) present themselves as a suitable candidate for the development of nanosized temperature sensors, as will be explained in the following section.

1.4. Magnetic iron oxide nanoparticles

1.4.1. Structure and Composition

MIONs have attracted interest not only due to their magnetic properties mentioned above but also due to excellent *in vivo* biocompatibility, tunable surface modifications, and facile synthesis.[5,31,83,97,98]

Among MIONs, Fe_3O_4 NPs have received tremendous attention justified by the aforementioned reasons, but also for displaying non-toxicity[83], high chemical stability[97], high heating efficiency[5], and the fact that they are well tolerated by the human body.[5] Magnetite is a well-known ferrimagnetic mineral that has a cubic inverse spinel structure (space group, *Fdm*) of AB_2O_4 type, $(Fe^{3+})_A(Fe^{2+}Fe^{3+})_BO_4$, in which one-eighth of the tetrahedral holes (8) are occupied by Fe^{3+} cations and one-half of the octahedral holes (16) are occupied by Fe^{3+} and Fe^{2+} cations.[31,33,99] In Figure 13 the unit cell of magnetite is elucidated as well as its spinel structure. The magnetic spins at octahedral sites are aligned parallelly with the direction of the external magnetic field, while the ones at tetrahedral sites align antiparallelly. Since there is twice the number of octahedral sites relatively to the tetrahedral sites, there is an unbalance of magnetic spins that results in a strong attraction to an external magnetic field with a high M_S in bulk, thus presenting a ferrimagnetic behavior up to about a T_C of approximately 850 K.[15,25,33] Taking into

account that magnetite possesses a *Tc* well above room temperature, it is expected that its magnetic properties are almost constant around room temperature.[25] Therefore, through doping, fine-tuning of its magnetic properties can be achieved in order to have particles that possess greater sensibility to temperature variations from -150 ºC to 44 ºC.

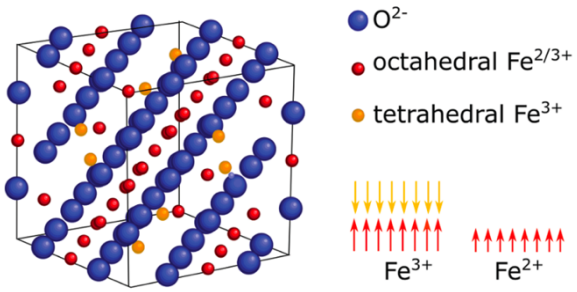

Figure 13. Unit cell of magnetite, in which a face-centered cubic lattice of O^{2-} ions (blue) is filled with Fe^{3+} and Fe^{2+} cations in octahedral sites (red) and Fe^{3+} cations in tetrahedral sites (yellow). Image reprinted from reference [15].

The net magnetization of the ferrite is dependent on the compensation of the different sublattices, which are composed by parallel magnetic moments of the atoms. Thus, the magnetization of the ferrite compound is fully determined by the inversion degree, in other words, the value of Fe^{3+} cations that occupy tetrahedral sites.[54,99,100] Previous reports suggest that doping spinel ferrites, with a formula AB_2O_4, with different ions such as Co^{2+}, Ni^{2+}, Zn^{2+} or Mn^{2+} can be performed to produce changes in the intrinsic magnetic couplings, yielding different M_s, magneto crystalline anisotropy values and different temperature dependence of the net magnetic moment.[31,100]

Doping is possible due to a plethora of factors responsible for determining the distribution of cations in spinel structure, such as the cation radius, Coulomb interactions between cations, and crystal field effects of the octahedral site preference energy (OSPE). The crystal field theory defines OSPE as the stable crystal field energy difference between the octahedral and tetrahedral fields, where usually a greater absolute value of OSPE means that the cation will prefer to occupy the octahedral interstices.[101] The aforementioned factors are listed in Table 2 for common ions.

Table 2. Number of electrons, crystal field stable energy (CFSE), and octahedral site preference energy (OSPE) of 3d transition metal ions. Adapted from [101].

ion	No. of 3d electrons	CFSE (kJ.mol^{-1})		OSPE (kJ.mol^{-1})
		Octahedral field	Tetrahedral field	
Sc^{3+}	0	0	0	0
Ca^{2+}	0	0	0	0
Ti^{4+}	0	0	0	0
Ti^{3+}	1	-87.4	-58.6	-28.8
V^{3+}	2	-160.2	-106.7	-53.5
Cr^{3+}	3	-224.7	-66.9	-157.8
Cr^{2+}	4	-100.4	-29.3	-71.1
Mn^{3+}	4	-135.6	-40.2	-95.4
Mn^{2+}	5	0	0	0
Fe^{3+}	5	0	0	0
Fe^{2+}	6	-49.8	-33.1	-16.7
Co^{3+}	6	-188.3	-108.8	-79.5
Co^{2+}	7	-92.9	-61.9	-31.0
Ni^{2+}	8	-122.2	-36.0	-86.2
Cu^{2+}	9	-90.4	-26.8	-63.7
Zn^{2+}	10	0	0	0
Ga^{3+}	10	0	0	0
Ge^{3+}	10	0	0	0

Generally, in the spinel ferrites with a formula AB_2O_4, the tetrahedral interstices are smaller than the octahedral interstices. It is therefore plausible to expect that A sites will be occupied with cations with smaller radii while B sites are occupied with larger cations.[101] Spinel ferrites have defects that can be classified into intrinsic and nonintrinsic. As for intrinsic defects, these are found in atomic arrangements without any dopants, including vacancies (Schottky defects), vacancy-interstitial pairs (Frenkel defects), and interstitial defects. In contrast, nonintrinsic defects are usually caused by external dopants such as substitutions of A and B sites with different cations.[101] As evidenced in Table 2, for example, the absolute value of Mn^{3+} (95.4 kJ.mol^{-1}) is higher than that of Mn^{2+} (0 kJ.mol^{-1}), indicating that Mn^{3+} prefers to occupy the octahedral interstices while Mn^{2+} tend to occupy the tetrahedral interstices. Following the same line of reasoning, Zn^{2+} presents the same absolute value (0 kJ.mol^{-1}) when compared with Mn^{2+}, meaning that both tend to occupy the tetrahedral interstices.

For these reasons, $Mn_xZn_{1-x}Fe_2O_4$ ferrites have been studied because for their low inherent toxicity, high M_s and low H_c, as a result of replacing Fe^{2+} ions by Mn^{2+} and Zn^{2+} ions.[31,102] However, even small structural changes yield different saturation values due to non-effective dopant incorporation, non-homogeneous compositions of Fe^{2+}/Fe^{3+}

replacement for Mn^{2+}/Mn^{3+} and Zn^{2+} ions, and thus making it difficult to obtain the expected properties.[31] For the sake of simplicity we will consider that only A sites are occupied by Mn^{2+} and Zn^{2+}, even if typically Mn in form of Mn^{3+} can also occupy B sites. A representative structure of $Mn_xZn_{1-x}Fe_2O_4$ ferrite is shown in Figure 14. Replacing a tetrahedral site Fe^{3+} with a less magnetic ion has the effect of lowering the strength of the opposing magnetic spin and consequently increasing the overall M_S relatively to magnetite. In the case of $Mn_xZn_{1-x}Fe_2O_4$ ferrites, both Mn^{2+} and Zn^{2+} ferrites have shown huge success when it comes to obtaining high M_S values, as the Mn^{2+} and Zn^{2+} ions preferably reside in tetrahedral positions. However, it is the occupation of Mn^{2+} ions that are responsible for determining its magnetic properties since Zn is nonmagnetic.[15,103,104] In fact, these chemical and structural modifications pave the way for the use of these ferrites as temperature sensors.

To better understand the behavior of $Mn_xZn_{1-x}Fe_2O_4$ ferrite as a temperature sensor, it is important to know the role of each atom in the spinel crystal structure. For instance, the oxygen anion, O^{2-}, is responsible for bounding all the surrounding elements together. Due to the fact that its bonds exhibit 180º between metal cations, the shared electrons possess opposite spins and are thus accountable for the antiferromagnetic order. As for the iron cation, Fe^{3+}, its contribution for the magnetic moment of the material comes from the high-spin d-orbital, as shown in Table 2. The manganese cation, Mn^{2+}, exhibits the same electronic configuration of Fe^{3+}, thus contributing with approximately the same magnetic moment as iron. Zinc cation, Zn^{2+}, has the valence orbitals fully paired, also evidenced in Table 2, which means that its contribution in terms of magnetic moment is null.[105]

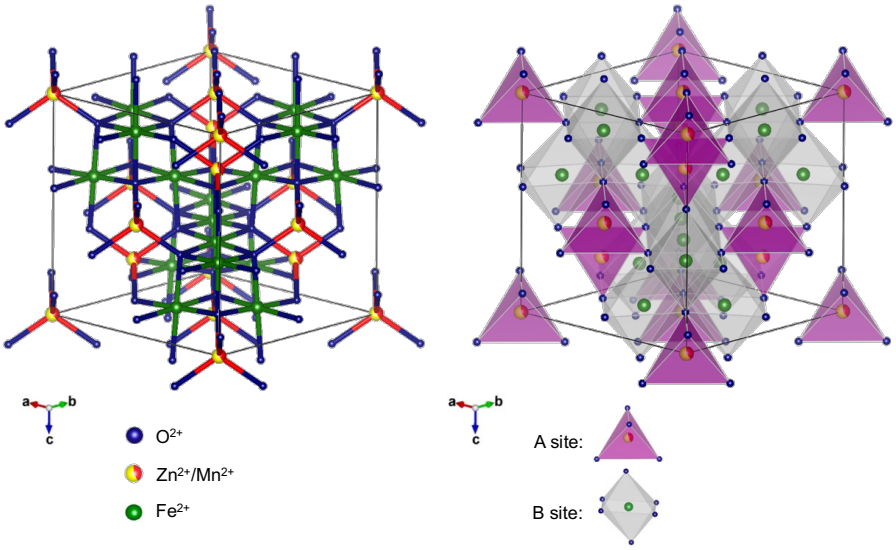

Figure 14. Representative spinel structure of $Mn_xZn_{1-x}Fe_2O_4$. Drawing of the structural models was achieved using VESTA software[106] *and lattice parameters imported from Crystallography Open Database (COD)*[107].

Having discussed their intrinsic magnetic properties, it now becomes clear how these ferrites have the potential to develop magnetic temperature sensors. However, achieving the desired structure with the desired properties for the intended application is not always an easy task. Herein, it is important to evaluate the many different methodologies that can be employed to produce MIONs, as well as their advantages and drawbacks. Thus, the next chapter will englobe several synthesis strategies, complemented with examples reviewed in current literature.

1.5. Synthesis strategies of MIONs

Nanoparticles synthesis strategies can be classified into two general approaches, namely the "top-down" and the "bottom-up" approach.[8,14,108] Top-down strategy involves miniaturization process from bulk materials towards a nanomaterial. On the contrary, bottom-up strategy whereby functional nanomaterials are assembled to achieve nanoscale building blocks.[14] The main synthesis pathways for obtaining magnetic iron oxide nanoparticles are reported as follows: *i)* chemical methods, such as coprecipitation, thermal decomposition, hydrothermal/solvothermal, sol-gel, microemulsion, polyol, sonochemical, molten-salts, cationic exchange; *ii)* physical methods including spray pyrolysis, laser pyrolysis, laser ablation, chemical vapor deposition, mechanical milling, among others; and *iii)* microbial methods.[30] In Figure 15 is depicted the growth kinetics, widely known as the La Mer curve.[8]

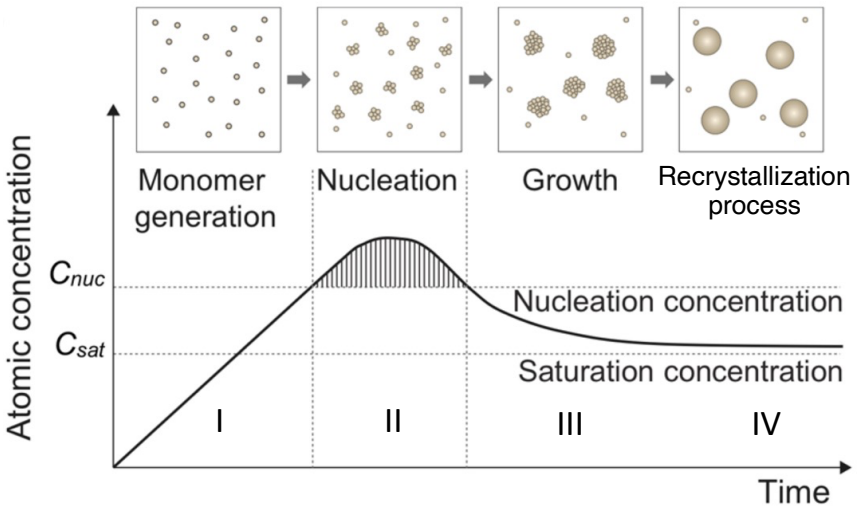

Figure 15. Monomer concentration over time describing the growth kinetics of inorganic nanoparticles. Upon exceeding nucleation concentration, the monomers become supersaturated and see nucleation is induced, leading to continuous aggregation of monomers onto the seeds, which consequently originates crystal growth. C_{nuc}: nucleation concentration, and C_{sat}: saturation concentration. Image adapted from reference [109].

According to Figure 15, the growth process can be divided in four main stages: (I) monomer precursor accumulation in solution; (II) nucleation; (III) particle growth; and (IV) recrystallization process.[8] A monomer here refers to a building block of the nanocrystals, generally recognized as the corresponding naked ions or molecules in solution.[8] Phase I demonstrates the first stage of accumulation of the monomer is created either from raw organometallic compounds or by thermolysis of the corresponding precursors in solution. The nucleating process of phase II will only take place after the accumulated monomer concentration in the solution reaches above the nucleation concentration. Due to a higher concentration of the monomer in phase II than the saturation concentration of the nanocrystals, all the formed nuclei will grow in solution, therefore leading to a concentration dependent consumption of the monomer. Consequently, the maximum of monomer concentration will be achieved in the middle period of the nucleation process, which will then decrease due to the increasingly monomer consumption rate, which can exceed the rate for the creation of the monomer. When the monomer concentration drops back below the nucleation concentration, the nucleation process will cease, after which there is a gradual growth of the formed nuclei that crystallize into nanocrystals (phase III). When the monomer concentration is reduced to the saturation level, it means the growth phase is completed, beginning phase IV of the recrystallization process, where the Ostwald ripening process will occur. During this stage, there is growth of larger particles at the expense of smaller ones. This is due to

the favoring of larger particles with smaller surface-to-volume ratios, whereas the smaller particles are energetically unstable when compared as shown in Figure 16. In order to achieve a narrow size distribution, this Ostwald ripening process must be avoided, and this can be done by means of precise temperature control. In practice, depending on the preparation conditions, either the prevention or the intended use of this process can be selected in order to produce homogeneous inorganic nanoparticles.[8]

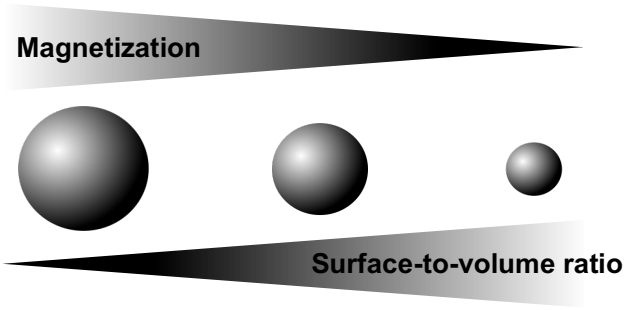

Figure 16. Representation of size-dependent magnetization effect and surface-to-volume ratio of MNPs.

Alternative methods such as microemulsion synthesis, hydrothermal synthesis or polyol synthesis have been attempted in order to improve the control over shape and size, although size control is still limited.[36,110] The aforementioned methods have fallen into disuse since the 2000s, as the thermal decomposition methods presented more potential and quickly developed for the synthesis of iron oxide NPs.[36] Thermal decomposition is well-suited for the formation of well crystallized NPs functionalized with organic molecules, providing colloidal stability in organic solvents. Furthermore, it presents the advantage of superior size and shape as it eases the separation of the nucleation and growth steps, which is a crucial factor to obtain NPs with a narrow size distribution. However, the obtained particles can only be dispersed in nonpolar solvents. A solution to this problem is to exchange the hydrophobic ligands for hydrophilic ligands.[36,111]

1.5.1. Coprecipitation methodology

This methodology is perhaps the simplest and most efficient chemical pathway to synthetize MIONs (Figure 17).[30,112] It consists on the coprecipitation of stoichiometric amounts of ferrous (Fe^{2+}) and ferric (Fe^{3+}) salts in an alkaline aqueous solution (Equation 1).[29,109,110,112] The size and shape of the MIONs depends on the pH of the solution, reaction temperature, ionic strength, presence of oxygen, stirring rate, nature of the salts (chlorides, nitrates, sulfates, or perchlorates), Fe^{2+}/Fe^{3+} ratio, and the nature and

concentration of precipitating agents to ensure the separation of the nucleation and growth processes.[29,30,101,110,112] Regarding the precipitation-inducing agents, the most commonly used are sodium hydroxide (NaOH), potassium hydroxide (KOH), and sodium carbonate (Na_2CO_3), for example.[101,112] While coprecipitation methodology is suitable for swift large scale production of MIONs directly in aqueous medium, it possesses some disadvantages, such as poor control over size homogeneity, and the produced NPs tend to aggregate in bulky clusters and possess a low degree of crystallinity.[36,112] In an attempt to surpass at least in part these drawbacks, modifications to the coprecipitation procedures have been proposed.

In this regard, Pereira *et al.* reported a novel one-step aqueous coprecipitation route to synthetize $MnFe_2O_4$ nanoparticles using alkanolamines isopropanolamine (MIPA) and di-iso-propanolamine (DIPA) as the alkaline agents. The synthesized NPs exhibited sizes ranging between 9.3 – 11.7 nm, high M_s (81.7-82.6 emu.g^{-1}), lower H_c, as well as high colloidal stability.[59] In another attempt, Mello and co-workers described the *in situ* coprecipitation synthesis of $Mn_xZn_{1-x}Fe_2O_4$ NPs in a polyethylene glycol (PEG) matrix.[113] This reaction was performed in the presence of PEG in order to ensure both physical and chemical stability of the colloidal systems, as well as biocompatibility *in situ*.[101] The synthetic conditions lead to the formation of $Mn_xZn_{1-x}Fe_2O_4$ NPs with well-defined sizes ranging from 10 to 15 nm, well-defined shape, high M_s (74 – 81 emu.g^{-1}) and lower H_c (7 – 9 Oe).[113]

Nevertheless, despite recent and significant improvements on the reactional conditions of this synthesis method, even in the presence of water-soluble coating materials, the resultant MNPs are still prone to agglomeration both in aqueous and physiological media. In addition, these novel synthetic approaches can be very challenging.[114]

$$M^{2+} + 2Fe^{3+} + 8OH^- \rightarrow MFe_2O4 + 4H_2O \qquad \textbf{(Equation 1)}$$

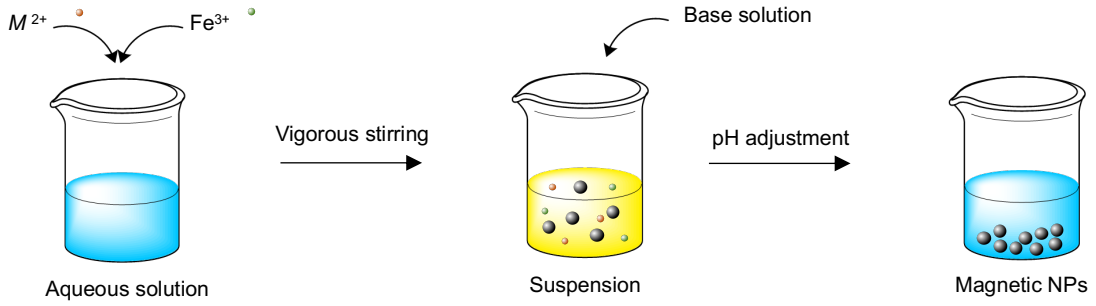

Figure 17. Schematic illustration of the synthesis of iron oxide nanoparticles obtained by coprecipitation methodology.

1.5.2. Thermal decomposition methodology

Thermal decomposition has been demonstrated to be the most effective approach to achieve MNPs with excellent crystallinity, as well as homogenous size distribution and shape, thus overcoming the limitations of coprecipitation methodology.[13,29,109,112,114,115] Decomposition of iron precursors or organometallics such as metal acetylacetonates ($Fe(acac)_3$), metal cupferronates ($Fe(cup)_3$, (cup)= N-nitrosophenylhydroxylamine)) and metal carbonyls ($Fe(CO)_5$) to synthesize MNPs is achieved when heat is applied to a reaction mixture.[29,109,110,114,115] The reaction medium usually consists of a high boiling point (*bp*) organic solvent and the presence of surfactants.[13,29,109,112,114,115] Amphiphilic surfactants such as oleylamine (OAm), oleic acid (OA), fatty acids and hexadecylamine control the nucleation and growth kinetics of the MNPs.[112] Consequently, monomers are generated and upon reaching a concentration above a supersaturation level, nucleation and subsequent growth of crystalline MNPs are induced (Figure 18).[109]

In 2002, Sun *et al.* reported the preparation of monodisperse Fe_3O_4 nanocrystals by separating nucleation and growth stages into two steps. In their study, single crystalline 4 nm MNPs were synthetized by decomposing $Fe(acac)_3$ in phenyl ether with 1,2-hexadecanediol (1,2-HDO) in the presence of a mixture of OAm and OA at 265 ºC. In a separated vessel, NP size was further increased up to 20 nm through a seed-mediated growth using the as-prepared Fe_3O_4 NPs as seeds. By changing the reaction solvent between phenyl ether (*bp* = 258 ºC) into benzyl ether (*bp* = 298 ºC), MNPs with diameters of 6 nm were synthesized.[116]

This approach was extended to the synthesis of size-controlled monodisperse MFe_2O_4 NPs simply using additional divalent transition precursors, as previously mentioned in *chapter 1.5.1*. In 2004, Sun and colleagues prepared monodispersive $MnFe_2O_4$ particles with around 14 nm and $CoFe_2O_4$ particles with around 16 nm, wherein acetylacetonates in phenyl ether were heated to 200 ºC in a previous stage followed by a second heat stage up to 265 ºC in the presence of OA acid, OAm and 1,2-HDO.[117] Comparing the both as-prepared particles, the authors concluded that $CoFe_2O_4$ particles presented more H_c than the $MnFe_2O_4$ particles, being 400 Oe and 140 Oe at 10 K, respectively.[117] In addition, they confirmed that an excess of OAm results in spherical nanoparticles as a consequence of their weaker bonding to nanoparticles surface, which in turn enables the growth of the nanoparticles in all plane directions.[118]

Regarding biological applications, the reaction conditions of thermal decomposition methodology have been tuned to obtain complex spinel oxides, such as $Mn_{\varkappa}Zn_{1-\varkappa}Fe_2O_4$ NPs. In 2009, Jang and his co-workers described a simple one-pot synthetic route to obtain spheric $Mn_{\varkappa}Zn_{1-\varkappa}Fe_2O_4$ NPs ($\varkappa$ = 0; 0.1; 0.2; 0.3; 0.4, and 0.8) with 15 nm and a maximum M_s of 175 emu.g^{-1} and a H_c of 3.7 (kA/m) when $\varkappa$ = 0.4. Simply, this method was carried out heating the solution in the presence of surfactants such as OAm and OA in octyl ether up to 300 ºC for 1 h.[119] In another attempt, in 2013, Xie and his co-workers described the synthesis of spherical $Mn_{\varkappa}Zn_{1-\varkappa}Fe_2O_4$ NPs with 9 nm by heating a solution of 20 mL octyl ether, coexisting with 10 mmol of OA and 2 mmol of OAm. The mixture was heated to 110 ºC for 30 mins with a 3 ºC.min^{-1} heating ramp with further heating up to 220 ºC for 2 h with the same heating ramp. Finally, the mixture was heated up to 300 ºC for 1 h, maintaining the same heating ramp.[120] However, the study showed a tendency for the Zn^{2+} cations occupy the tetrahedral sites, thus hindering the cation distribution regarding Mn and Zn ions. In addition, this method presented some issues, specifically the need to have a three-steps methodology. Another example to achieve high M_s was reported by Sun *et al.*, in 2019, where spheric $Mn_{\varkappa}Zn_{1-\varkappa}Fe_2O_4$ NPs were obtained by heating a solution of 2 mmol of OAm,10 mmol of OA and 20 mL of dibenzyl ether (DBE) up to 220 ºC with a 3.3 ºC.min^{-1} heating ramp. Thereafter, a second heating was performed, up to 300 ºC at the same rate and kept at this temperature for 1 h. In this study, nanoparticles with 24 – 30 nm and a M_s of 82.86 emu.g^{-1} were obtained.[121] Recently, Wang *et al.* reported a two-step synthesis to obtain spheric $Mn_{\varkappa}Zn_{1-\varkappa}Fe_2O_4$ NPs with 15 nm by heating up to 200 ºC for 2 h a mixture with 10 mmol of 1,2-HDO, 3 mmol of OA, 3 mmol of OAm and 20 mL of benzyl ether. The mixture was further heated up to 300 ºC with a 2 ºC.min^{-1} heating ramp and left for further 90 mins.[122] Interestingly, the presence of 1,2-HDO contributed for the well-resolved lattice fringes and the monodispersive size of the as-prepared NPs.

To conclude, despite the abundance of optimized methodologies for the synthesis of Mn-Zn ferrites, thermal decomposition methodology stands unparalleled regarding to NP size distribution control, which in turn directly affects magnetism, thus being of special importance for this thesis.

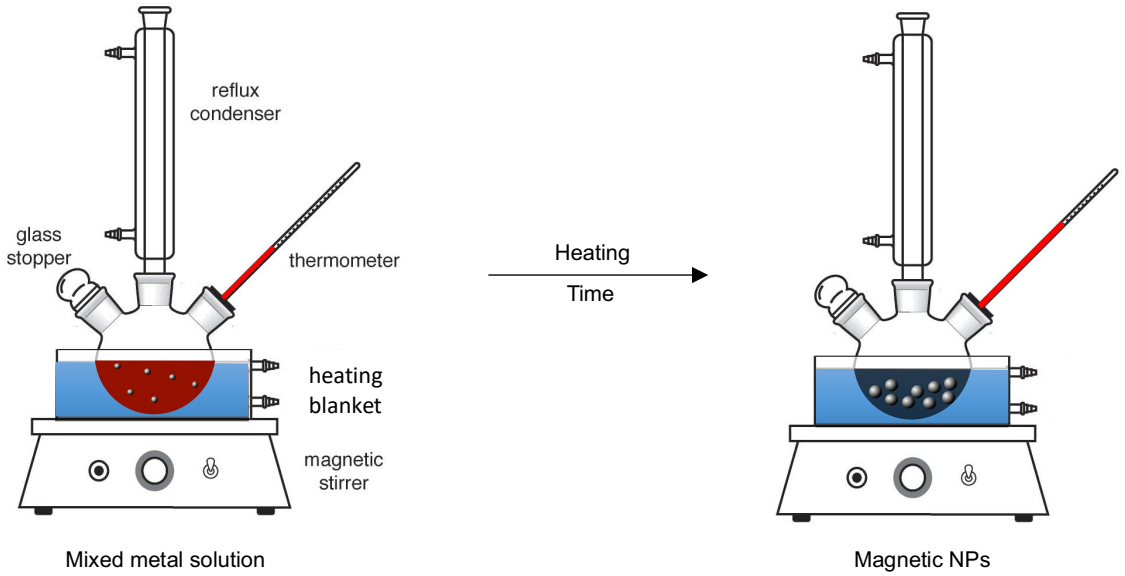

Figure 18. Schematic illustration of synthesis of iron oxide nanoparticles obtained by thermal decomposition methodology.

Two main methods can be described in order to perform a thermal decomposition of an iron complex as demonstrated in Figure 19. The first is the “hot injection” way, which consists in the injection of pertinent precursors into a hot solution containing the high boiling solvent and the surfactants. This process creates a burst of decompose metallic complex, which is critical to sharply separate the nucleation process from the growth process and consequently crucial for producing homogeneous NPs.[8] However, this method and its reproducibility are not easily controlled, which bears a limitation in scale-up synthesis.[36] The second way, the “heating-up” approach, whereby the temperature of the reaction solution containing preloaded precursors and surfactants is elevated from room temperature to the solvent boiling point, leading to the supersaturation of the solutions, thus to the nucleation of NPs.[8] This method provides a great deal of freedom regarding the design of NPs to tune their size, morphology, and composition. However, this freedom comes with a cost, as it is increasingly difficult to understand the master process because all parameters are related to each other and the tuning of one parameter will consequently influence another.

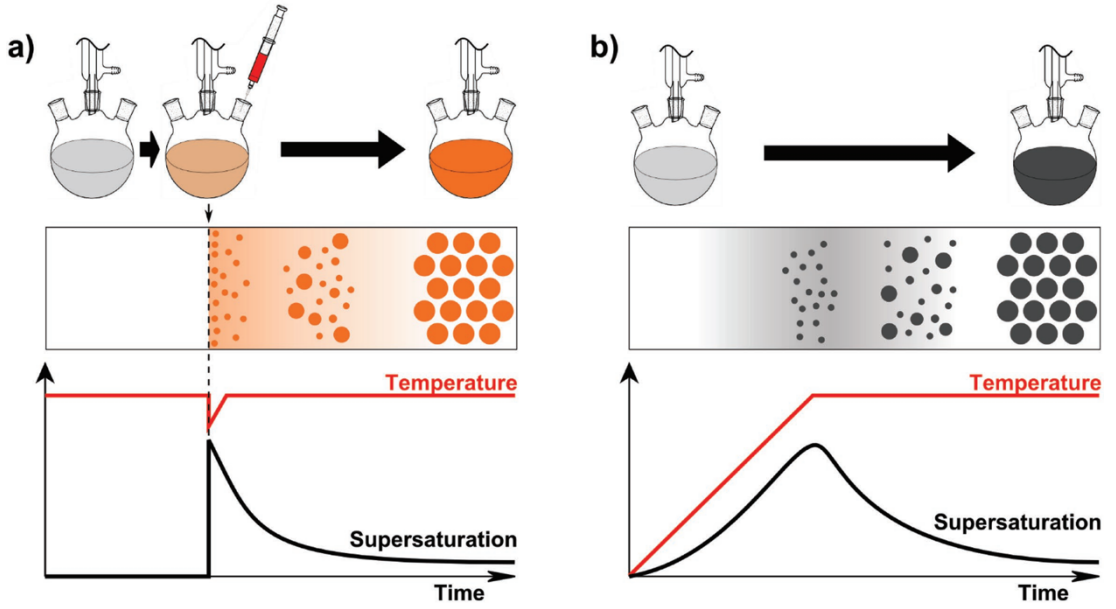

Figure 19. Schematic representation of synthesis methods of nanoparticles by: a) "Hot injection", and b) "Heat-up" method.[20]

1.5.3. Molten salts methodology

Molten salts are a type of ionic liquid that provides a suitable environment for the formation and stabilization of metal nanoparticles, often neglecting the need to use stabilizing additives or capping molecules.[123,124] Briefly, this method consists on the nucleation and growth of an oxide within a molten salts solution medium by the dissolution of precursors and posterior precipitation of the oxide product. The process can be summarized in five steps: *i)* mixing the precursors with the appropriate salts; *ii)* heating the mixture to a determined temperature to cause the melting of the salts; *iii)* at synthesis temperature, dissolution of the precursors into the ionic solvent will take place; *iv)* then, nucleation of the desired product occurs, followed by its growth; *v)* finally, with the appropriate cooling rate, the mixture is cooled and the product collected.[124] The first synthesis of Mn-Zn ferrites by this method was performed by Okamoto *et al.* in 1986, where flaky Fe_2O_3 powders were prepared by hydrothermal route that were subsequently mixed with ZnO and Mn_3O_4 in an alumina crucible and heated up to 1150 ºC for 1 h under a N_2 atmosphere, resulting in Mn-Zn NPs with about 10 μm and anisotropic morphology.[125] In a different study performed in 2014, Lou and his team reported the synthesis of $MgFe_2O_4$ NPs by heating the molten salt at 800 ºC for 4 h with a 5 ºC.min^{-1} heating ramp.[126] Recently, Yamada *et al.* described the synthesis of $CoMn_xFe_{2-x}O_4$ NPs by heating the molten salt up to 900 ºC for 2 h.[127] However, to the best of my knowledge,

there are no synthesis regarding the production of Mn-Zn ferrite nanoparticles by molten salts methodology.

1.5.4. Hydrothermal/Solvothermal methodology

In the hydrothermal approach, reactions occur in a sealed environment under high-pressure, thus enabling the synthesis of highly crystalline phases at much lower temperatures when compared to coprecipitation and thermal decomposition methods.[101,115,128] Two main routes are reported in the literature for the formation of ferrites: *i)* hydrolysis and oxidation where ferrous salts are used, and *ii)* neutralization of mixed metal hydroxides.[30,101,115,128] In a typical hydrolysis procedure, appropriate reaction precursors, solvents, and surfactants with functional groups are mixed and then heated in reaction vessels known as autoclaves (Figure 20). Surfactants like polyethylenimine (PEI), ethylenediaminetetraacetic acid (EDTA), cetyltrimethylammonium bromide (CTAB), and OA will act as chelating agents to the cationic ions to regulate their reacting concentration which is essential for the control of the crystalline phase, size, and morphology.[128] The main difference between these methods is that the hydrothermal method uses water as the solvent whereas in the solvothermal method an organic solvent is used.

Rath *et al.* reported the first synthesis of 9 – 12 nm-sized $Mn_{0.65}Zn_{0.35}Fe_2O_4$ particles by neutralizing the chlorides precursors in aqueous ammonia solution. After pH adjusting, the mixed solution was heated at 180 ºC. By varying the pH it was shown that under pH of 10, incomplete precipitation is observed, thus demonstrating that pH around 10 was optimum to obtain a complete precipitation as well as maintaining the initial stoichiometry. It was also verified that increasing pH from 9 to 11 leads to an increase both in H_c and M_s. Particles obtained at pH 10 showed a M_s of 58.3 emu.g^{-1} and a H_c of 13 Oe at 2 K.[129] Inspired by this work and considering the aforementioned observations, Zahraei *et al.*, in 2015 reported the synthesis of $Mn_xZn_{1-x}Fe_2O_4$ NPs by adjusting the pH between 9 – 10.5 of chlorides precursors using an aqueous ammonia solution. The mixed solution was heated by varying the temperature, namely at 160, 180 and 200 ºC. Regarding the effect of temperature, the optimum hydrothermal temperature was found to be 180 ºC. In order to investigate the optimum hydrothermal duration, temperature was regulated in 4, 12 and 20 h at 180 ºC. However, a contamination of hematite phase was observed during all performed studies. To surpass this, citrate was used as a chelator, whereas a monophase $Mn_{0.6}Zn_{0.4}Fe_2O_4$ particles with a mean particle size of 7 nm and a narrow size were obtained. In addition, the NPs are easily dispersed in water

at physiological pH and presented a M_s of 103.7 emu.g^{-1} and a H_c of 210 kOe at 5 K.[50] Recently, according to our knowledge, Rezaei and his team reported for the first time the synthesis of monophase $Mn_xZn_{0.3}Fe_{2.7-x}O_4$ by one-step citric acid-assisted hydrothermal method. Interestingly, increasing the pH up to 10 allowed to obtain a pure phase, which is in a good agreement in previous reports by Zahraei *et al*. Optimized $Mn_{0.5}Zn_{0.3}Fe_{2.2}O_4$ particles sized 28 nm are considered to be a good candidate for biomedical applications showing a high M_s of 54 emu.g^{-1} at 300 K.[130]

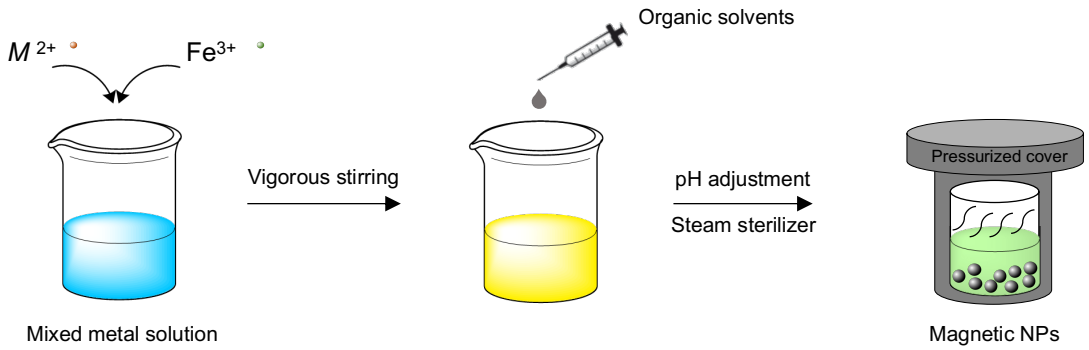

Figure 20. Schematic illustration of the synthesis of iron oxide nanoparticles obtained by hydrothermal methodology.

1.5.5. Sol-gel methodology

Sol-gel method is a mild wet route to the synthesis of nanostructured metal oxides. Typically, metal salts are used as precursors in which hydrolysis and condensation will occur in the formed transparent sol systems (Figure 21) in the presence of chelating agents.[101,110,112] The latter usually are described as being citric acid, ethylenediaminetetraacetic acid, propionic acid, ethylene glycol, glycine, glacial acetic acid, P123, or resorcinol/formaldehyde.[101] Through condensation and inorganic polymerization, the sol mixture will gradually turn into a 3-D network of metal oxide denominated wet gel. These reactions are performed at room temperature. Further heat treatments are needed to remove any volatile by-products in order to acquire the final crystalline state, typically raging temperatures from 450 to 800 ºC.[101,110,112,131,132] Temperature, pH, nature of solvent, type and concentration of the salt precursors and stirring are the main parameters that influence the hydrolysis and the condensation reactions.[101,110,112]

Metal doped ferrite particles synthesized by sol-gel methodology was pioneered in 1993 by Chatterjee *et al*. In this study, crystalline $Ni_{0.5}Zn_{0.5}Fe_2O_4$ particles were synthesized within a SiO_2 matrix using nitric acid was used as a chelate agent. By varying

the sintering temperature of the gel from 700 to 1050 ºC, the authors were able to increase the particles size from 13 to 34.7 nm, respectively. As a result, a M_s of 11.7 emu.g^{-1} at 10 kOe and a H_c of 20 Oe where obtained from the particles sintered at 700 ºC, whereas a M_s of 31.5 emu.g^{-1} at 10 kOe and a H_c of 75 Oe were obtained from the ones sintered at 1050 ºC.[133] Similarly, in 2001, Mandal and his team synthesized 20 nm-sized crystalline $Mn_{0.5}Zn_{0.5}Fe_2O_4$ particles within a SiO_2 matrix, where the gel was heated at 550 ºC for 8 h with a further heat up to 1040 ºC for 10 mins. However, it was only mentioned that even at 10 kOe magnetic field there was no sign of magnetic saturation, suggesting the need of exploiting the magnetic properties of this system of Mn-Zn ferrites.[134]

In this framework, later in 2014, Szczygieł and his team studied the effect of precipitating agents towards the magnetic properties. In a two-step methodology, 65.9 and 40.8 nm-sized $Mn_{0.6}Zn_{0.4}Fe_2O_4$ particles with enhanced magnetic properties by pre-sintering the gel at 850 ºC for 10 h and sintered at 1300 ºC under atmospheric air. Particles prepared using a NaOH solution sowed a M_s of 112 emu.g^{-1} and a H_c of 80 Oe at 2 K, whereas particles prepared using ammonium oxalate ($(NH_4)_2C_2O_4$) showed a M_s of 95.7 emu.g^{-1} and a H_c of 65 Oe at 2 K.[55] Recently, Aisida *et al.* demonstrated a one-step synthesis of Mn-Zn NPs which consisted in using nitrate as precursors. After separately dissolving the precursors in double distilled water, the pH was adjusted to 9 using NaOH. Homogeneous sol structure was obtained by maintaining the mixture 50 ºC for 4 h. A reddish-brown viscous gel was formed after keeping it at 70 ºC for 6 h. Finally, nanoparticles were sintered at 900 ºC for 1 h in a vacuum tube furnace, obtaining nanoparticles of 17.5 nm in size with a M_s of 44.4 emu.g^{-1} and a H_c of 124 Oe.[135]

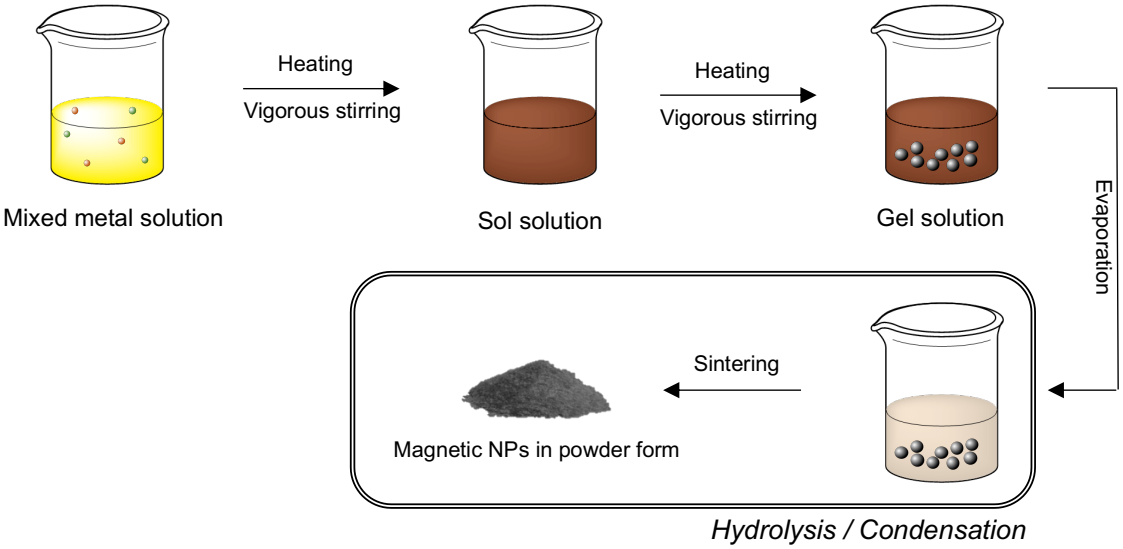

Figure 21. Schematic illustration of the synthesis of iron oxide nanoparticles obtained by sol-gel methodology.

1.5.6. Polyol methodology

The polyol methodology consists of a reverse sol-gel process in which the polyol acts as solvent, reducing agent and stabilizer, playing an important role in preventing interparticle aggregation and controlling the MNPs size (Figure 22).[29,30,110] Polyols like ethylene glycols, namely mono-, di-, tri-, and poly(ethylene glycol), propylene glycol among others, possess interesting properties: *i)* high dielectric constants; *ii)* an ability to dissolve inorganic compounds, and *iii)* a high boiling temperature.[29,30,110] When employing this synthetic technique, the metal precursor is suspended in a liquid polyol. The suspension is then heated up to its boiling point, under vigorous stirring. During this process, the metal precursor becomes soluble in the diol where an intermediate is formed. The latter is reduced to form a metal nuclei that will then nucleate and form metal particles.[30,110] First described in 2001, Ammar *et al.* developed a novel route for the preparation of $CoFe_2O_4$ particles using 1,2-propanediol at 160 ºC under atmospheric air. In this study, crystalline 5.5 nm-sized particles with 65 emu.g^{-1} at 300 K were reported.[136] Concerning the promising magnetic properties demonstrated by this innovative methodology, Ammar and his team explored the properties of $Mn_xZn_{1-x}Fe_2O_4$ particles. In this regard, crystalline 12 nm-sized $Mn_{0.2}Zn_{0.8}Fe_2O_4$ particles were developed using diethylene-glycol for 6 h, which exhibited M_s of 96 emu.g^{-1} at 5 K, as well as lower H_c of 0.3 kOe at 5 K. However, it was found that with doses up to 0.1 mg.mL^{-1} the as-prepared particles present a considerable cytotoxicity for the human endothelial cells, suggesting the need for particles functionalization.[137] In this context, Iacovita *et al.* reported the synthesis of $Mn_xZn_{1-x}Fe_2O_4$ particles in ethylene glycol, where the mixture was heated

with a heating ramp of 3 ºC.min^{-1} up to 200 ºC for 6 h. However, to improve colloidal stability, TMAOH (tetramethylammonium hydroxide) was used, thus reflecting a lower cytotoxicity up to 0.2 mg.mL^{-1}.[138] To conclude, despite the breakthroughs towards polyol methodology, it typically involves temperatures of calcination which greatly exceed 200 ºC to afford a higher crystallization when compared with other well-studied methodologies.[139]

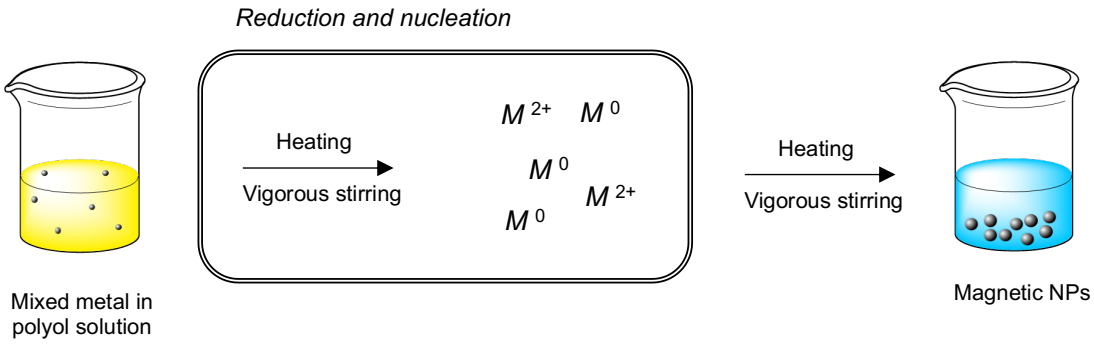

Figure 22. Schematic illustration of the synthesis of iron oxide nanoparticles obtained by polyol methodology.

1.5.7. Sonochemical methodology

When employed, the sonochemical methodology uses the chemical effects of ultrasonic irradiation that arises from acoustic cavitation to assist nanoparticle synthesis (Figure 23). The high energy released upon implosive collapse of the bubbles produced in the solvent medium is released into heat, which generates a transient localized hot spot through adiabatic compression or shock wave formation within the gas phase of the collapsing bubble.[29,30,110,115] This method, also known as "ultrasound-assisted synthesis" is used to prepare highly monodispersive MNPs through the optimization of parameters such as, sonication time, frequency, and power of the sonication.[29,115]

To the best of our knowledge, the first synthesis of metal doped Fe_3O_4 by sonochemical methodology was described in 1998 by Shafi and co-workers. This synthesis produced $CoFe_2O_4$ particles through ultrasonic irradiation of $Fe(CO)_5$ and $Co(NO)(CO)_3$ precursors in Decalin at RT, under an oxygen pressure of 100 – 150 kPa for 3 h. The respective particles exhibited a size of *ca.* 10 nm and presented an amorphous phase, trace amounts of carbon impurities and a M_s of 72 emu.g^{-1}. After heating the $CoFe_2O_4$ NPs for 5 h at 450 and 700 ºC under atmospheric air, the authors verified an increase in the crystallinity as well as a decrease in the M_s of 22 and 45 emu.g^{-1}, respectively.[140] In 2014, Abbas and his team, in 2014, also reported the synthesis of

the $CoFe_2O_4$ NPs at RT for 70 mins, in which the authors obtained high crystalline particles by working with different solvents, namely, an aqueous medium and an ethanol/water mixture. Furthermore, whereas particles synthesized in ethanol exhibited an average size of 20 nm with a cubic shape, the samples prepared by both in water or in the mixture exhibited a 200 nm monodispersive spherical shape. The higher M_s was observed for the particles prepared in the water/ethanol mixture, reaching 92.57 emu.g^{-1}.[141] Motivated by the need for advances in biomedical applications, Almessiere and colleagues recently described a 11 nm-sized monodispersive $Mn_{0.5}Zn_{0.5}Dy_xFe_{2-x}O_4$ particles that can be synthesized in water for 45 min at RT. In its findings, the team verified an increase of M_s from 54.77 to 59.55 emu.g^{-1} at 10 K when Dy^{3+} increases from 0.0 to 0.3.[142] As such, contributions of this study deserve to be mentioned, since they obtained a better anti-bacterial and anti-proliferative activities between $Mn_{0.5}Zn_{0.5}Dy_xFe_{2-x}O_4$ particles prepared *via* ultrasonication methodology than in those produced by *via* sol-gel.[58]

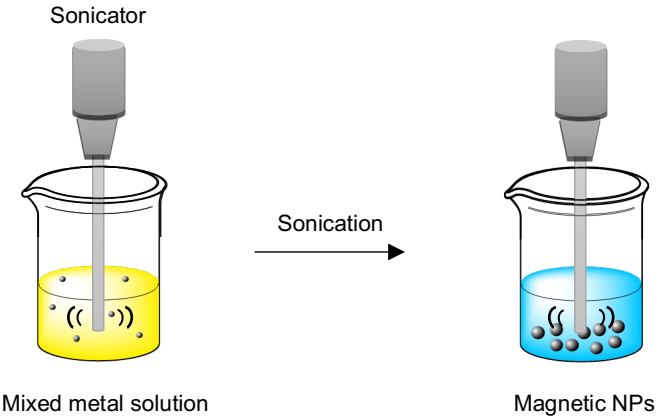

Figure 23. Schematic illustration of the synthesis of iron oxide nanoparticles obtained by sonochemical methodology.

1.5.8. Microwave-assisted synthesis methodology

Microwave-assisted synthesis relies on the generation of high energy microwaves with wavelengths from 1 mm to 1 m that cause molecular motion with friction, generating enough energy for the synthesis of MNPs.[101] In depth, microwave radiation causes the excitation of the molecules, causing an alignment of the molecular dipoles according to the external field. The rearrangement of the molecules with the electric field generates an intense internal heating, that is responsible for reducing the reaction times.[29,143] Furthermore, this technique allows the control of MNPs size and shape by varying the experimental conditions in real time.[131,143]

The first microwave-assisted methodology was reported in 2007 by Zhenyu and his team. Combining microwaving heating with coprecipitation conditions, crystalline $Mn_xZn_{1-x}Fe_2O_4$ particles sized around 10 nm were obtained. In this study, the authors verified that microwave heating only for 5 mins was enough obtain 12.11 nm-size particles, whereas under conventional heating it is necessary more than 6 h to obtain 10.0 nm-size particles.[144] More recently, crystalline MFe_2O_4 (where *M* = Mn, Fe, Co, Ni and Zn) particles with average sizes of 3.2 and 4.3 nm were reported by suspending acetylacetonates precursors in 1-dodecanol and irradiating the mixture to raise its temperature to 259 ºC in 10 min and maintained at this temperature for 60 mins. These particles showed suitable properties in order to improve several applications, namely, storage, catalysts, sensors and ferrofluids.[76] In sum, microwave heating has proven valuable in its contribution to the development of low-temperature routes to obtain crystalline particles in a significant short reaction time.[139]

1.5.9. Cationic exchange methodology

The concept of cationic exchange essentially consists on the chemical conversion of one solid to another by exchanging the constituent cations.[145,146] It is generally a simple process in which a starting nanocrystal has its cations replaced while preserving the original anion sublattice, although, in some cases, it is observed a certain degree of structural reorganization.[146,147] This process yields nanocrystals of a new material that preserves the size and shape of the original nanocrystal. In a crystal, cations are usually much smaller than anions, thus having a much higher diffusion rate than its counterpart. This is why cations are able to diffuse within a rigid lattice of anions and why cation exchange takes place instead of anion exchange. In sum, this technique allows the design of novel nanocrystals with a specific morphology, or even a specific crystal phase, if the starting nanocrystals are finely developed.[145,147,148]

The formation of iron oxide particles prepared by partial cationic exchange was firstly reported in 2013 by Sytnyk *et al.* by exposing Fe_3O_4 to Co^{2+} cations in the presence of trioctylphosphine (TOP), obtaining $CoFe_2O_4$ nanocrystals, while the anionic framework remained intact with size and shape preservation. Cationic exchange demonstrated to be an outstanding approach for tuning and improving the magnetic properties, as verified the increase in M_s from 6.97 to 43.51 emu.g^{-1} at 300 K.[149] In 2016, a study performed by Zhao and co-workers showed the synthesis of $Mn_xFe_{3-x}O_4$ NPs and $Zn_xFe_{3-x}O_4$ NPs. In this study, chlorides were used as precursors. Briefly, after dissolving manganese chloride in 6 mL of degassed OAm and heated to 120 ºC for 15 mins, the mixture was

left to cool at RT. The latter was injected into a degassed solution containing 10 mL of 1-octadecene, 2 mL of OAm and 1 mL of tri-*n*-octylphosphine (TOPO) at 180 ºC for 2 h. The obtained $Mn_{\varkappa}Fe_{3-\varkappa}O_4$ NPs maintained its size and morphology during cation exchange reactions. For the $Zn_{\varkappa}Fe_{3-\varkappa}O_4$ NPs the protocol is slightly modified due to different physical properties of Mn and Zn cations. Remarkably, spherical $Mn_{\varkappa}Fe_{3-\varkappa}O_4$ and $Zn_{\varkappa}Fe_{3-\varkappa}O_4$ NPs possessed M_s of 57.3 emu.g^{-1} and 64.6 emu.g^{-1}, respectively, while the as-prepared SPIOs demonstrate a M_s of 49.7 emu.g^{-1}.[150] With all this in mind, cationic exchange demonstrates, to some extent, a better control over the purity of produced nanomaterials. This in turn, sets the pace for the discovery of many unexplored nanomaterials yet to be synthesized, perhaps with novel and astounding features that may only be acquired through cationic exchange.[147]

1.5.10. Microbial methodology

Biological systems such as fungi, bacteria, actinomycetes, yeasts and viruses have demonstrated potential for the production of several nanoparticles, both intra- and extra-cellularly, earning the role of biofactories for nanoparticle synthesis.[151] However, these systems often need to be modified and their environment for production, optimized. In other words, careful monitorization of parameters such as pH, temperature, exposure time to the substrate, biomass, and substrate concentration is critical to control growth conditions, cellular activities, and enzymatic processes to ensure the production of NPs with controlled size and shape.[152]

To our knowledge, the first synthesis of metal doped Fe_3O_4 NPs by microbial route was performed in 2001 by Roh and co-workers. Fe(III)-reducing bacteria, namely, *Thermoanaerobacter* and *Shewanella* were used under anaerobic conditions. The fermentation was carried out by incubation of a β-FeOOH precursor ($M_{\varkappa}Fe_{1-\varkappa}OOH$, where *M* = Co, Cr and Ni) with the bacteria while maintaining the temperature at 65 ºC and maintained for 7 to 30 days by intermittent addition of electron donors such as glucose. It was described the successful synthesis of nm-sized $M_{\varkappa}Fe_{3-\varkappa}O_4$ (where *M* = Co, Cr and Ni) particles.[153] In order to understand the biological reduction and mineralization process with more detail, Moon *et al* performed a similar experimental study, in 2007, where $M_{\varkappa}Fe_{3-\varkappa}O_4$ (where *M* = Co, Cr, Mn, Cr and Ni) with a 5 – 90 nm-sized particles were reported.[154] Regarding the enhancement of the magnetic properties, Byrne *et al*, in 2014, reported the synthesis of spherical $Zn_{\varkappa}Fe_{3-\varkappa}O_4$ with a size ranging from 8.3 to 16.1 nm, where the maximum M_s reached 97 emu.g^{-1} at 300 K for $\varkappa$ = 0.16. Zinc doped NPs were obtained by the reduction of Fe(III)-Zn(II) bearing materials

by *Geobacter sulfurreducens*, using sodium acetate as electron donors.[155] However, there is still a significant knowledge deficiency regarding the underlying processes and pathways through which microorganisms can produce doped NPs, thus making microbial approach a difficult to control synthetic technique to be used in the synthesis of NPs.[151,155]

To summarize there is a vast collection of literature regarding the different synthesis methodologies for MNPs with different structural properties. Table 3 presents an overview of several reliable methodologies, their synthesis conditions and practical outcomes, comparing their advantages and disadvantages.

Table 3. Comparison of nanoparticles synthesis methods. Adapted from [28,36,110,112,156].

Method	Conditions	Size distribution	Shape control	Degree of crystallinity	Yield
Thermal decomposition	(1) Improved size control, narrow size distribution, tunable magnetic properties (2) Long reaction time, high temperature, organic solvents, requires surface treatment after synthesis	Very narrow	High	High	High
Coprecipitation	(1) Fast reaction time, water solvent, ease surface modification, low temperature (2) Low reproducibility, uncontrolled oxidation, lack of precise stoichiometric phase control	Average	Average/ Poor	Low	High
Hydrothermal	(1) Water/water-ethanol solvents, tunable magnetic properties (2) High pressure, long reaction time, high temperature	Relatively narrow	Average	High	Average
Microemulsion	(1) Low reaction time, ease synthesis, low temperature (2) Water/organic solvents, high solvent utilization, difficult scale-up	Relatively narrow	Poor	Low	Poor
Polyol	(1) Quite fast reaction time, ease surface modification (2) High temperature, organic solvents	Relatively narrow	Average	Relatively High	Average

(1) Advantages, (2) Disadvantages

1.6. Stabilization procedures of MIONs

In order to use MIONs in biomedical applications it is crucial to produce a stable and biocompatible colloidal suspension. A colloidal suspension of MNPs in a magnetically passive carrier liquid with distinct properties such as fluidity of Newtonian liquids and magnetization like bulk magnetic materials is termed a ferrofluid. These possess several properties, as for example magnetic, thermal, optical, electrical, etc., and can be tuned by an external magnetic field for the intended application. For instance, they can be employed as heat transfer medium in thermal management devices or coolant in energy conservation systems.[157,158] However, due to the strong magnetic dipole-dipole interactions and innate high surface energy, these particles tend to aggregate, hindering their use in biomedical applications.[158] Furthermore, magnetic iron oxide nanoparticles possess a high dissolution rate in biological systems, which is accompanied by the leaching of toxic metal ions.[98,111] For these reasons, many efforts have been devoted to the surface modification of MIONs with a wide variety of stabilizing agents, such as surfactants or polymers, in order to introduce nanoparticle repulsions that avoid Van der Waals interactions and magnetic dipole forces, while providing biocompatibility.[110,159,160] The nature of the surface of a material dictates the stabilization strategy to be applied. Iron oxide nanoparticles, for example, possess hydroxyl groups (–OH) on their surface which can change their charge according to pH variations, thus exhibiting amphoteric properties.[110,161]

With this in mind, there are two main approaches to functionalize the surface of nanoparticles and obtain stable colloidal suspensions, namely, ligand addition and ligand exchange, as illustrated in Figure 24.[110] In ligand addition, the hydrophobic portions of the particles interact with amphiphilic molecules, which adds new molecules to the surface of the nanoparticles. In the case of ligand exchange, the pre-existing hydrophobic groups on the surface are replaced with new ones, through exchange reactions.[24,161] The type of molecule used for functionalization determines how the particles will interact with each other, causing either steric of electrostatic repulsions. In turn, these repulsions are responsible for enhancing particle stabilization, while the hydrophilic character of polymers added to the surface of nanoparticles is also essential to assure biocompatibility in living systems.[162]

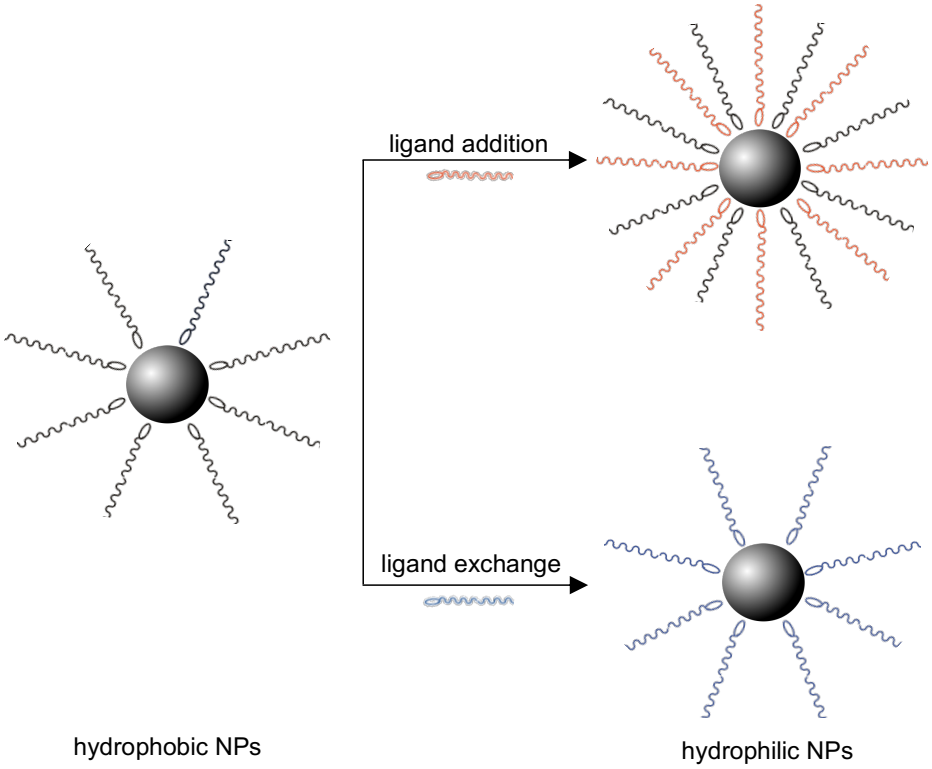

Figure 24. Representation of surface modification approaches of hydrophobic magnetic particles capped with hydrophobic ligands via ligand addition method using amphiphilic ligands and ligand exchange method using hydrophilic ligands, respectively. Image adapted from [24].

It is important to mention that the addition of ligands to the surface may increase the total radius of the NPs, which may affect its application in biomedicine, since the size of NPs is deeply relevant for its success. Therefore, it is often in the best interest to search for alternatives that possess simple functionalization methods, as well as coatings which do not contribute to an increase in NP size.

These strategies may include a plethora of different materials, as exhibited in Table 4. PEG is one such example, being known for its biocompatibility and improving the circulation time of nanoparticles for *in vivo* applications.[163] In a practical example, Xie *et al*. produced PEG-coated manganese-zinc (Mn-Zn) ferrites for cancer targeted magnetic hyperthermia applications. In this study, *in vivo* fluorescence imaging of mouse models of 4T1 breast tumor allowed the authors to conclude that the PEG coating contributed to a longer circulation time, as well as to the passive and active accumulation in the tumors, confirming the system's colloidal stability.[164]

Citric acid is another compound known to have been employed in the stabilization of MIONs.[165,166] It is a dispersive agent that possesses three carboxylic groups (–COOH) capable of covalent binding with the iron ions in iron oxide particles. Electrostatic repulsions between citric acids therefore prevent NP aggregations, consequently

increasing the dispersibility of the MIONs.[167] Zahraei *et al*. synthetized citric acid-stabilized Mn-Zn ferrite NPs and not only verified an increased stability by transmission electron microscopy and dynamic light scattering analysis, as also evaluated the impact of subsequent coatings of chitosan, PEG, and dextran on the NPs stability and heating properties for theragnostic applications. Briefly, the coating of these NPs with citric acid provides their surface with carboxylic groups capable of forming amide groups with the aforementioned polymers. This evidences that citric acid can either be used as a stabilizing agent on its own or serve as a basis for further functionalization. Moreover, the researchers confirmed that subsequent polymer conjugation produced stable and biocompatible assemblies for said application.[168]

Now regarding inorganic materials, SiO_2 is often preferred as a stabilizer, owing to its biocompatibility and its chemically inert nature. In addition, SiO_2 acts as a shield to the magnetic dipolar attractions between MIONs, granting them improved stability.[163]

Table 4. Some examples of organic, polymeric and inorganic materials reported as coating of MFe_2O_4 NPs.

Coating	Capping agents	Refs.	Capping agents	Refs.
Organic	caffeic acid	25	dopamine	169
	citric acid	170,171	OAm	118,172
Polymeric	PEG	113,121,122	chitosan	173,174
	PNIPAAm	175	DMSA	119,164
Inorganic	gold (Au)	176	silver (Ag)	177
	SiO_2	178,179		

PNIPAAm: poly(N-isopropylacrylamide, DMSA: 2,3-dimercaptosuccinic acid

1.7. 3-D liquified compartmentalized systems as disease models

Given the intended applications for this thesis, magnetic ferrofluids acting as temperature sensors for hyperthermia or cryopreservation applications need to exhibit a certain amount of sensitivity in their measurements in a way that the NPs temperature is closely similar or equal to that of the surrounding medium.[180] This is a matter of extreme importance, as in hyperthermia, for example, lack of accuracy in temperature measurements may directly translate into excessive or insufficient supply of heat for cancer cell ablation, resulting in healthy tissue damage or inefficient cell ablation, respectively. Therefore, it is important to simulate an external environment that mimics

a target tissue and is susceptible to temperature changes in order to evaluate the thermometry potential.[181] For this, a phantom tissue can be used.[182] In fact, there is a plethora of phantoms available for thermal experiments, in which gel phantoms are the most recognized. These can present different materials such as polyacrylamide, agar, and gelatin, which are the most widely used for this application.[183] As a practical example, Miaskowski and Sawicki produced simplified female breast phantom to evaluate the potential of a magnetite ferrofluid for magnetic fluid hyperthermia, concluding that with proper control of temperature, breast tumors could be ablated with minimal side effects.[184] Similarly, Ashikbayeva and colleagues evaluated the potential of gold and magnetic iron oxide nanoparticles for laser-assisted ablation on a porcine liver phantom. With the aid of fiber-optic sensor network incorporated into the tissue, the authors managed to create a two-dimension (2-D) temperature map of the phantom and concluded that the sensing fibers allowed the measurement of temperature with great accuracy. However, the system was prone to one drawback, namely the failure to introduce laser light into the tissue interstitially.[185] Thus, the present thesis aims to tackle these drawbacks by exploiting the magnetic properties of iron oxide nanoparticles to create nano-sized temperature sensors that will potentially be able to perform a 3D temperature mapping of tissues.

1.8. Outline and Main Objectives

This dissertation aims to develop nanothermometers by controlling their T_C through doping of iron oxides with manganese and zinc ions. Based on the current literature and previous works describing new and improved methodologies toward the thermometry, this work intends to prepare NPs with high sensitivity and a linear response within a temperature range from -150 to 44 ºC. These nanothermometers are to be applied in possible applications regarding the nanoscale wireless 3-D temperature mapping of biological tissues to better control both hyperthermia and cryopreservation procedures. Predictably, the synthesis of the NPs will be carried out using thermal decomposition methodology and, if possible, a molten-salt methodology with mild reaction conditions. In latter, the optimization of several reactional parameters is to be studied, such as reaction temperature and time, precursors or mixture of precursors, heating ramp, among others. The as-prepared NPs will be characterized using several standard solid-state techniques (XRD, FT-IR), electron microscopy (SEM, EDS and TEM), as well as analysis by DLS, magnetization measurements, and zeta potential determination.

Investigations on the magnetic properties of the resulting MNPs may only be possible with the close collaboration with some researchers and group leaders expert in these scientific fields. Thus, Dr. Nuno João Silva (Researcher of the Associated Laboratory CICECO) will perform the variation of magnetism with temperature in collaboration with the research group led by Dr. A. Millán (Instituto de Ciencia de Materiales de Aragón/CSIC, Zaragoza).

Therefore, the main goals to be accomplished are:

i) Synthesis and optimization of the reaction conditions of $Mn_xZn_{1-x}Fe_2O_4$ NPs by thermal decomposition and molten salt methodology;

ii) Stabilization of the MNPs obtained, due to their tendency to aggregate and/or agglomerate throughout biocompatible molecules;

iii) Magnetic properties evaluation, mainly of MNPs that present a unique phase and a relatively good elemental composition to assess their potential for thermometry applications.

Chapter 2: Experimental section

This chapter consists of a thorough description of the selected materials, as well as the characterization techniques used to analyze the developed nanomaterials. The experimental procedures, such as the innovative synthesis of Mn-Zn ferrite nanothermometers by thermal decomposition and molten salts methodology, as well as the stabilization strategies with citric acid and EDTA are also described in detail in this section. Regarding thermal decomposition, there are several well-established methods already developed for the synthesis of Mn-Zn ferrite NPs, however, here we present several optimizations of this methodology, resulting in a more economic approach. With respect to the hereby presented molten salts method, it reflects the first synthesis of Mn-Zn ferrites made by this methodology.

2.1. Reagents, characterization methods and general procedures

2.1.1. Reagents

1,2-Hexadecanediol (>98.0%) was obtained from TCI. Dibenzyl ether (≥98.0%), manganese$_{(II)}$ acetylacetonate ($Mn(acac)_2$), ≥98.0%), zinc$_{(II)}$ acetylacetonate ($Zn(acac)_2$ ≥95.0%), iron$_{(III)}$ acetylacetonate ($Fe(acac)_3$), ≥99.0%), zinc nitrate hexahydrate ($Zn(NO_3)_2$•$6H_2O$, 99%), manganese$_{(II)}$ nitrate hydrate ($Mn(NO_3)_2$•xH_2O, 99.98%), citric

acid ($C_6H_8O_7$, >99.0%) and sodium hydroxide (NaOH, 98.0%) were purchased from Alfa Aesar. Oleylamine (80-90%) was obtained from Acros Organic. Ethanol absolute (100%) was supplied by VWR Chemicals. Potassium nitrate (KNO_3, 99.0%) and EDTA were purchased from PanReac. $Iron_{(III)}$ nitrate nonahydrate ($Fe(NO_3)_3 \cdot 9H_2O$, >98%), oleic acid (90%) and dichloromethane (≥99.8%) were obtained from Sigma-Aldrich. All chemicals were used as acquired without any further modification or purification.

2.2. Characterization methods

2.2.1. X-ray powder diffraction (XRD)

X-ray diffraction (XRD) is a nondestructive technique widely used for phase identification of crystalline materials and to identify the unit cell structure as well as the atomic space. The latter, also known as interatomic distance, can be calculated using Bragg's law. The NPs in form of powder were dried overnight at 75 ºC and left to cool to RT in a desiccator before characterization by XRD. The samples were grinded with a mortar to ensure a smooth surface for the diffraction to occur at the same weight throughout the whole sample. XRD patterns were recorded using a PANalytical X'Pert PRO diffractometer equipped with a copper anode with a wavelength Cu Kα of 1.5450 Å (operated at 40 kV and 45 mA). Scans from thermal decomposition samples were collected in the 20-65º 2θ range, each 0.05º with a scan step speed of 0.05 s in reflection mode, whereas scans from molten-salts samples were collected in the 20-80º 2θ range keeping fixed the remaining parameters. Rietveld Refinement was performed using the Software FullProf Suite® which also gives information about crystal phases, lattice parameters and crystallite size, for example.

2.2.2. Fourier transform infrared (FT-IR) spectroscopy

The Fourier transform infrared (FT-IR) spectroscopy model Mattson-7000 operating in absorbance mode was used to verify the presence or absence of surfactants such as OA and OAm in the surface of MNPs. Samples were prepared by grounding the nanoparticles with potassium bromide (KBr) at 2 % by weight and compressed them into a pellet. FT-IR spectra were collected in the range of 4000 - 250 cm^{-1} by accumulating 256 scans, and with a resolution of 2 cm^{-1}. After measuring all FT-IR spectra corresponding to a selected strain and background subtraction, the average spectra were calculated. In order to identify the organic functional groups of the aforementioned compounds, the samples were analysed in attenuated total reflectance (ATR) mode, on

a Mattson (GALAXY SERIES FT-IR 7000) in the range of 4000 - 350 cm^{-1} by accumulating 256 scans, and with a step resolution of 2 cm^{-1}.

2.2.3. Scanning Electron Microscopy (SEM) and Energy-dispersive X-ray spectroscopy (EDS)

Scanning electron microscopy (SEM) is widely used method that produces images of a sample's surface by scanning it with a high-energy beam of electrons, enabling a qualitative analysis SEM micrograph were obtained using a Hitachi SU-70. To this end, ultrasound bath was used to disperse a diluted suspension of NPs in ethanol for 30 mins. After that, a drop of suspension was held by a carbon tape in a commercial aluminum stub and kept in air until complete evaporation of the solvent. Further coating with carbon was necessary due to the high acceleration voltage using in the SEM (15.0 kV). Said carbon coating is required because of the insulator nature of the powders. Without this coating, the samples would accumulate charge when interacting with the electron beam, which in turn deflects the beam and causes image brightness saturation, which hinders particle distinction.

The chemical composition and distribution of elements (Mn, Zn, Fe) of the samples were evaluated by energy-dispersive X-ray spectroscopy (EDS) using a sensor attached to Hitachi SU-70. In the case of lighter elements, such as oxygen, EDS analysis presents a significant error. Therefore, upon analyzing the samples composition, it was assumed that oxygen was completely integrated in the ferrite. The stoichiometric estimation was performed under the assumption that the Fe ion was also fully integrated, and according to the chemical formula $Mn_xZn_{1-x}Fe_2O_4$. The composition of the samples was calculated through the normalization of the metal ions with respect to the heaviest of ion present, Fe, in order to ensure minimal error.

2.2.4. Transmission Electron Microscopy (TEM)

The morphology and size distribution of the MNPs was studied by using Transmission Electron Microscopy (TEM) on a JEOL (model 2200FS) with an acceleration of 200 kV. To prepare an electron-transparent NP sample, samples in powder form were diluted in ethanol and stirred in ultrasound for 30 mins to favor particle dispersion. Subsequently, the diluted solution was deposited onto a copper grid coated with an amorphous carbon film by diving it inside the solution and then allowing it to dry completely. The particle size was calculated by measuring the size of 50 NPs from the

TEM micrographs using ImageJ software. The mean particle size as well as the respective standard deviation were later evaluated by applying a Gaussian function to the size distribution using Origin software.

2.2.5. Dynamic light scattering (DLS)

Hydrodynamic nanoparticle diameters were measured by a dynamic light scattering (DLS) technique with a solid-state He-Ne laser (λ = 633 nm) by a Malvern Zetasizer Nano ZS™. This technique provides information about the size of the particles in suspension in a short time. Samples obtained by thermal decomposition technique were diluted in dichloromethane and analyzed at 25 ºC, whereas samples obtained by molten salts methodology were diluted in water after nanoparticle surface stabilization. It is important to refer that particle concentration should be low in order to minimize the magnetic dipolar interaction, resulting in a clear, brown-colored solution after sample dilution.[64]

2.2.6. Zeta Potential

To assess surface modification of MNPs with citric acid or EDTA, the zeta potential was measured using disposable DTS1070 cells also with a Malvern Zetasizer Nano ZS™ instrument. Isoelectric point of pure and stabilized samples was obtained through electrophoretic mobility in water. The results were obtained with 3 measurements and a maximum of 100 runs using the Smoluchowski model. Aforementioned, after diluting the samples, the particle concentration should be low, to consequently reduce the magnetic dipolar interaction and obtain a clear, brown-colored solution.[64]

2.2.7. Magnetic characterization

Magnetization measurements in function of temperature reveal how the materials magnetization change with the evolution of temperature. The magnetic properties of the samples were acquired by a Superconducting Quantum Interference Device (SQUID) magnetometer from Quantum design (MPMS-7 K). The measurements were carried out using dried NPs held into a sample holder with cotton and reenforced with Kapton tape. Powder samples were weighted with high precision (*ca.* 20 mg) in order to normalize all magnetization to the sample mass to obtain the magnetization per mass.[31,186] The DC magnetic susceptibility as a function of temperature, $M(T)$, was achieved down to 5 K

using ZFC and FC protocols, at $H = 50$ Oe. The plot of ZFC and FC curves was obtained using Origin software.

2.3. Synthesis of $Mn_{\varkappa}Zn_{1-\varkappa}Fe_2O_4$ NPs

2.3.1. Thermal decomposition methodology

Iron oxide nanoparticles doped with manganese and zinc were synthetized by thermal decomposition method according to a procedure previously described by [187] and [122] with some modifications. Noteworthy, all the synthesis were performed in a 50 mL three neck round bottom flask equipped with a water-cooled condenser connected to a standard Schlenk line. Different amounts of $Mn(acac)_2$, $Zn(acac)_2$ and $Fe(acac)_3$ reagents were mixed to form nanoparticles with the formula $Mn_{\varkappa}Zn_{1-\varkappa}Fe_2O_4$ ($\varkappa = 0.13, 0.35, 0.6$). The used reagent quantities used for the preparation of all samples are shown in Table 9 (Appendix). TD1 NPs, for example, were obtained by mixing $Mn(acac)_2$ (0.13 mmol, 0.0401 g) with $Zn(acac)_2$ (0.87 mmol, 0.2312 g) and $Fe(acac)_3$ (2 mmol, 0.7331 g), in conjunction with OA (3 mmol, 0.8821 g), OAm (3 mmol, 0.8158 g) and 1,2-HDO (1.5 mmol, 0.4003 g) were mixed and dissolved in 37.5 mL of DBE in a 50 mL three neck round bottom flask. Under nitrogen flow and vigorous stirring, the mixture with reddish brown color was purged for 15 min and heated at a rate of 10 ºC.min^{-1} until 220 ºC, where it remained for 2 h to favor nanoparticle nucleation. Then, the solution was heated to 300 ºC at 10 ºC.min^{-1} heating rate and maintained in reflux for 1 h to complete the nanoparticle growth. The black-brown mixture was cooled to room temperature by removing the heating source, and the obtained nanoparticles were precipitated with 20 mL of ethanol PA. In order to remove the reagents and solvent remainders, nanoparticles were resuspended in a mixture of 3:1 (ethanol PA:dichloromethane) and centrifuged at 6000 rpm over 15 min. The purification process was repeated six to ten times to obtain Mn-Zn ferrite nanoparticles. Thus, $Mn_{0.13}Zn_{0.87}Fe_2O_4$, $Mn_{0.35}Zn_{0.65}Fe_2O_4$ and $Mn_{0.60}Zn_{0.40}Fe_2O_4$ were obtained and stored in powder. Figure 25 demonstrates the thermal decomposition process for the as-prepared $Mn_{\varkappa}Zn_{1-\varkappa}Fe_2O_4$ NPs. In Table 9 (Appendix), all the obtained $Mn_{\varkappa}Zn_{1-\varkappa}Fe_2O_4$ NPs are described.

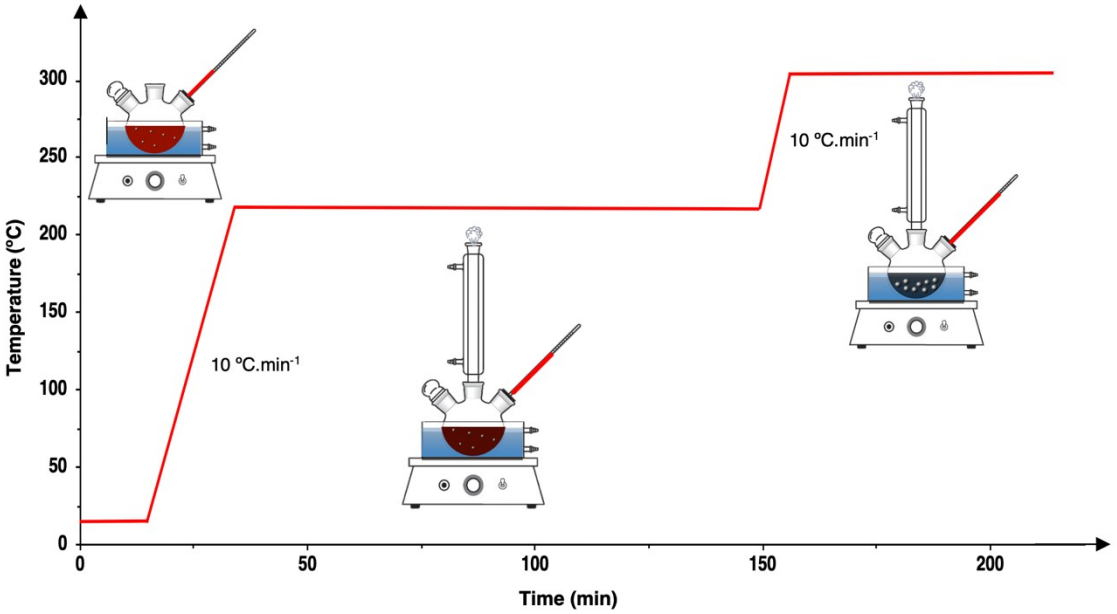

Figure 25. Illustration of the heating profile of thermal decomposition to obtain $Mn_xZn_{1-x}Fe_2O_4$ NPs.

There are multiple reports of Mn Zn ferrite NPs by thermal decompositions using different amounts of surfactants and DBE. However, in the present work, efforts were made to simplify the process and reduce the overall costs of this method. To this end, two distinct amounts of DBE were used, namely 37.5 and 20 mL[64,116,117], along with some variations in the surfactant concentrations, as shown in Table 9 (Appendix).

2.3.2. Molten salts methodology

The experimental design of the synthesis of iron oxide nanoparticles doped with manganese and zinc was based on the optimized synthesis method of manganite perovskite nanocubes (LSMO).[188] For sample MS1, for example, a mixture of $Mn(NO_3)_2{\bullet}xH_2O$ (0.10 mmol, 0.0248 g), $Zn(NO_3)_2{\bullet}6H_2O$ (0.90 mmol, 0.2627 g), $FeN_3O_9{\bullet}9H_2O$ (2 mmol, 0.7995 g) and KNO_3 (9.89 mmol, 1.0037 g) were milled inside a mortar with a few drops of absolute ethanol and a homogeneous mixture was obtained for approximately 10 min. This step allowed to melt the precursors into a “molten-salt” mixture that was further deposited in an alumina crucible. After drying, it was inserted in a tubular oven heated from RT to 500 °C at 5 °C.min^{-1} where it was treated under air flow for 1 h and 40 min. Then, the dark brown powder was maintained at 500 °C for more 20 min. The obtained powder was removed from the furnace and quenched at RT. It was washed with deionized water and the resulting dark brown precipitate was washed by five cycles of centrifugation-redispersion in deionized water. The last wash was performed with ethanol absolute and the powder was dried overnight at 75 °C. Figure 26

demonstrates the molten-salts process for the as-prepared $Mn_xZn_{1-x}Fe_2O_4$ NPs. In Table 11 (Appendix) all the obtained $Mn_xZn_{1-x}Fe_2O_4$ NPs are described.

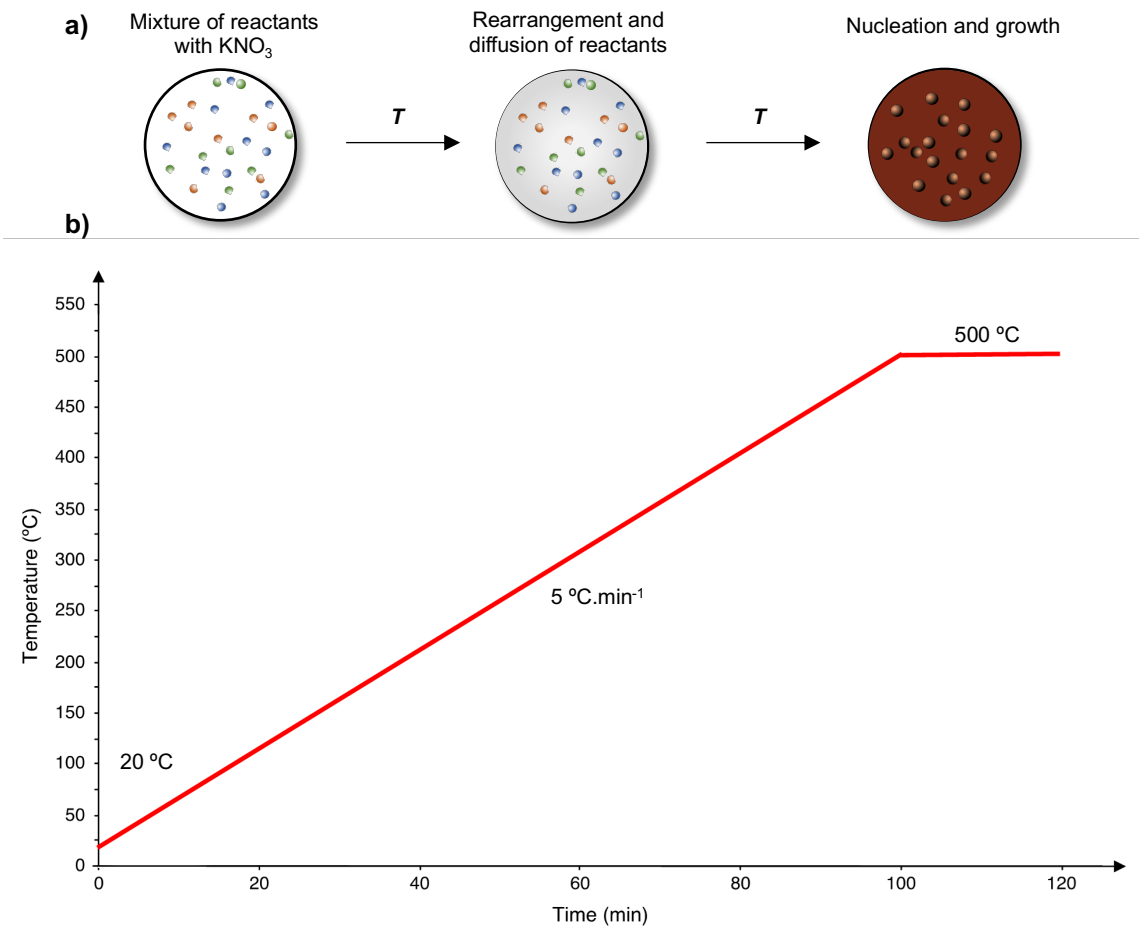

*Figure 26. Illustration of the **a)** mechanism of conventional molten salts method, and **b)** heating profile of molten-salts method to obtain $Mn_xZn_{1-x}Fe_2O_4$ NPs.*

2.4. Production of a magnetic ferrofluid

In order to produce ferrofluids, proper stabilization of the NPs is essential to avoid aggregation. To this end, two stabilization strategies were employed, with EDTA and citric acid (Figure 28). The chemical structure of citric acid and EDTA is demonstrated in Figure 27. In the first, aqueous ferrofluids of $Mn_xZn_{1-x}Fe_2O_4$ NPs were produced according to a procedure previously described by [189] with some alterations, where 25 mg of NPs were dispersed in 30 mL of 0.005 M EDTA solution along with NaOH by ultra-sonication for 30 min. After verifying a neutral pH, the mixture was left at 70 or 90 ºC for 4 h under vigorous stirring. The particles were collected by centrifugation at 6000 rpm for 15 min and washed four times with deionized water to remove unattached EDTA. The sample was then re-dispersed in 4 mL of deionized water without further washing. In the

other strategy, attempts to obtain aqueous ferrofluids of $Mn_xZn_{1-x}Fe_2O_4$ NPs were performed using citric acid according to a procedure previously described by [85], also with some alterations, in which 25 mg of NPs were dispersed in 30 mL of concentrations varying from 0.005 to 0.05 M citric acid solution. After adjusting pH by means of NaOH addition until pH ~ 7, the mixture was left at 70 or 90 ºC for 4 h under vigorous stirring. After that the particles were collected by centrifugation at 6000 rpm for 15 min and washed four times with deionized water to remove unattached citric acid. The sample was then re-dispersed in 4 mL of deionized water without further washing. The attempts to obtain a ferrofluid are depicted in Table 5. It is clear that, stabilization in water relies on the initial state of the NPs, for example, the longer the NPs remain in storage in powder form, the more difficulties would be encountered in this method.

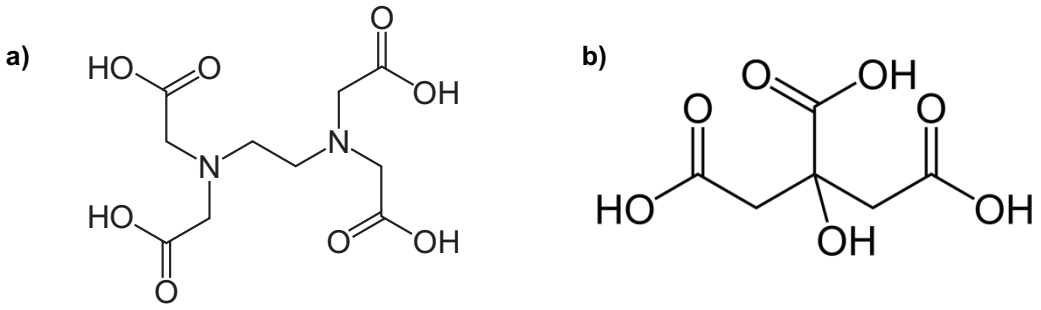

Figure 27. Structures of a) EDTA, and b) citric acid as alternative functionalization agents for the NPs.

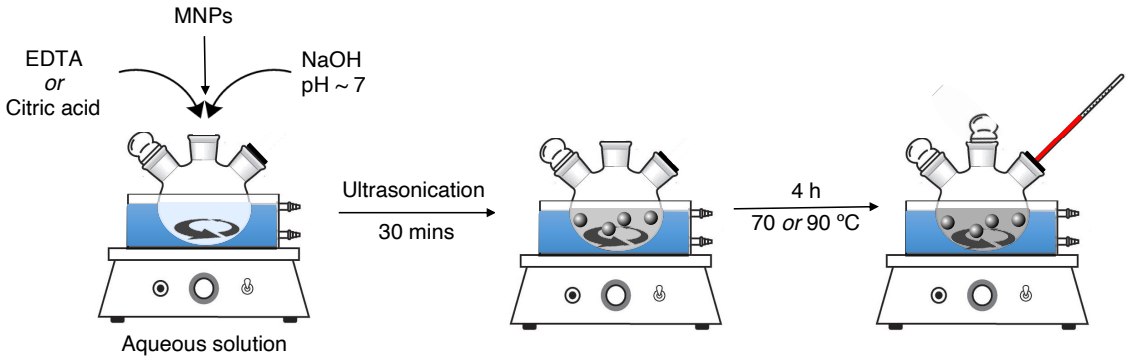

Figure 28. Dispersion of the MNPs in order to obtain a stable magnetic ferrofluid by using either EDTA or Citric acid, both for 70 and 90 ºC.

Table 5. Reaction conditions for the ferrofluids preparation.

Sample	Starting NPs	$\langle d \rangle_{TEM}$ (nm)	EDS	*t* (h)	*T* (ºC)	Dispersant	[C] (M)
FP14	TD11	5.8	0.42:0.65:2	4	70	Citric acid	0.05
FP16	MS4	3.9	0.42:0.62:2				
FP15	TD11	5.8	0.42:0.65:2			EDTA	0.005
FP17	MS4	3.9	0.42:0.62:2				
FP20	MS4	3.9	0.42:0.62:2		90	Citric acid	0.05
FP19	TD11	5.8	0.42:0.65:2				
FP18	TD11	5.8	0.42:0.65:2			EDTA	0.005
FP21	MS4	3.9	0.42:0.62:2				

$\langle d \rangle_{TEM}$: particle diameter estimated by TEM analysis, T: temperature, t: time, [C]: concentration

2.5. Ferrofluid encapsulation

Validating the precision of the temperature measurements obtained by the developed magnetic thermometers is of paramount importance to this work. To this end, a similar environment to the one intended to harbor the magnetic thermometers was successfully achieved by internalization of the ferrofluids in gelatin capsules, thus simulating a phantom tissue (Figure 29). Briefly, 100 μL of 1 %w/v gelatin (Gelatin from porcine skin, Type A, Sigma-Aldrich CAS: 9000-70-8) aqueous solution was added to 100 μL of ferrofluid. The mixture was then frozen overnight to allow gelation of the solution, using a round-shaped vessel. The external membrane was produced by subsequent immersion of the still frozen mixture in a 2 %w/v alginate (ALG) solution and then in a 0.2 M calcium chloride solution ($CaCl_2$). This procedure was repeated two times in order to obtain a stable and fully individualized capsule. After the assembly of the ALG membrane, the capsules were kept in distilled water to assure their stability. Afterwards, phantom simulation continued by building a bigger macrocapsule with an overall size of 1 cm of thickness using the first capsule. Firstly, capsules were immersed in 1.5 mL of 10 %w/v gelatin aqueous solution using a round-shaped vessel, and then the material was frozen overnight once again, similarly to the approaches made by [190,191]. The frozen macrocapsule was then immersed in a 2 %w/v alginate solution and then in a 0.2 M calcium chloride solution. This procedure was repeated three times to assure a stable 3-D model system. Finally, the gelatin macrocapsules were allowed to fully thaw at ambient temperature, with the system assuming an almost transparent appearance of liquid-within-liquid individualized compartments.

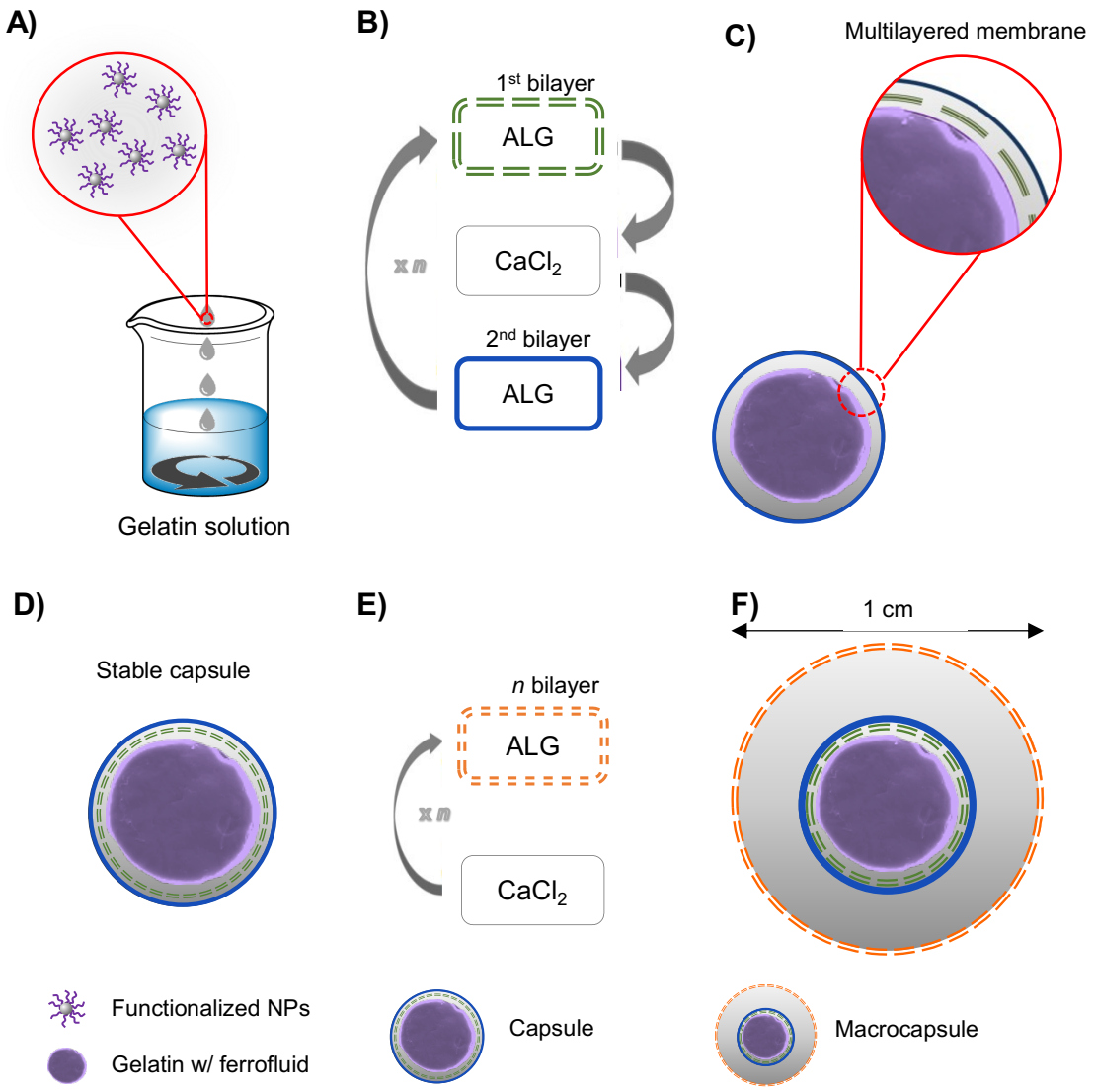

Figure 29. Internalization of the ferrofluids in gelatin capsules in order to simulate a phantom tissue. ***A)*** *Production of gelatin capsules containing an optimized suspension of NPs;* ***B)*** *Production of the multilayered membrane by dip coating, using alginate (ALG) and calcium chloride ($CaCl_2$);* ***C)*** *Representation of the obtained multilayered capsules;* ***D)*** *Production of gelatin macrocapsules containing the gelatin capsules with an optimized ferrofluid;* ***E)*** *Production of the multilayered membrane on gelatin macrocapsules by dip coating, using alginate (ALG) and calcium chloride ($CaCl_2$);* ***F)*** *Representation of the obtained multilayered gelatin macrocapsules.*

Chapter 3: Results and discussion

Mn-Zn ferrites have been extensively studied for a plethora of applications over the years. However, their use in thermometry applications is scarce, as reflected by the lack of literature regarding this matter.[38,39,51] The particular interest in nanothermometry arises from the fact that aforementioned Mn-Zn ferrites possess low inherent toxicity, high M_s and low H_c as well as high chemical stability.[31,102] However, as highlighted in the

introduction, such doping process is quite challenging since magnetic properties are strongly dependent on their chemical composition, size, synthesis methods, as well as the distribution of cations between tetrahedral and octahedral sites. Hence, the objective of this study is to prepare Mn-Zn ferrite nanoparticles by thermal decomposition and molten salts methodologies, with high M_s, lower H_c and high sensitivity regarding a suitable range of temperature for both cryogenic and hyperthermia applications.

3.1. Thermal decomposition methodology

3.1.1. Synthesis results analysis

Before proceeding further, the question arises on why thermal decomposition methodology has received great attention to date for sensing.[15,116] One important reason lies on the efficient separation of the nucleation and growth processes as they occur at different well-defined temperatures. This, in turn, provides an excellent control over size, shape and composition, thus allowing the precise adjustment of structural and magnetic properties. These findings are directly supported by literature as demonstrated by [15,74,83,192], for example. In this methodology, a constant flux of nitrogen is essential to remove reaction sub-products such as water, carbon dioxide, acetone, etc., and achieve highly-monodispersive MNPs. It is important to perform this step not only at RT but also until reaching 220 ºC to obtain a proper liquid dispersion of the powder reagents. In addition, to prevent an overly intense reflux, the magnetic stirring should not be excessively fast, or else it will cause considerable splashing and bubbling. With respect to centrifugation speed, higher speeds can originate MNP aggregates, while lower speeds can result in lower yields.[64]

Mn-Zn ferrite nanoparticles were synthetized *via* a colloidal thermal decomposition of $Fe(acac)_3$, $Mn(acac)_2$, $Zn(acac)_2$ by 1,2-HDO in a mixture of DBE as a solvent and in the presence of OA and OAm as surfactants. Regarding the choice of materials, metal-organic complexes are known to be one of the most used precursors for synthetizing nanoparticles. Among these complexes, $Fe(acac)_3$ and $Fe(oleate)_3$ showed themselves as promising candidates.[15,193] However, $Fe(oleate)_3$ is a multi-step synthesis precursor that originates a caramel-like compound which is hard to manage and weight.[194] Consequently, this evidence would hinder the method reproducibility, as well as possibly increase human error, thus the other candidate, $Fe(acac)_3$, was selected as an iron precursor due to its advantages, namely being a commercial powder precursor, easy to handle, and providing reproducible results.[194] The remaining precursors were chosen due to their low costs and high yields, making them suitable for

Mn-Zn ferrite synthesis by thermal decomposition method.[117] Regarding the other acetylacetonates precursors, it seems that Zn^{2+} ions are incorporated into the spinel more efficiently when compared to the zinc chloride precursor. A possible explanation may be attributed to the presence of water, introduced as bounded molecules to chloride salts, which has a negative impact on the method.[195] The same explanation can be extended to the $Mn(acac)_2$ precursor.

A brief description of the role and effects of each precursor in the synthesis conditions will now be provided. With respect to 1,2-HDO, its absence has shown not to affect the particle size although it influences the nanoparticle's polydispersity.[196] It is also known that a higher concentration of this compound leads to a wider size distribution of the NPs. This compound also appears to be able to assist in the decomposition of the acetylacetonates precursors, thus favoring the particle nucleation at lower temperatures.[196]

Concerning the indispensability of OA, some reports state that its key role on the reactional mixture is to tune the mean particle size. In fact, it has the effect of delaying nucleation towards higher temperatures, thus creating smaller nuclei while modulating the particle growth kinetics.[11] The standalone use of OA originates a viscous product which hinders purification and characterization.[117] In the absence of OA, however, there is a higher probability of nanoparticle aggregation.[196] It is believed that OA not only acts as a stabilizer but also as a reducing agent in the synthesis process.[54] Nevertheless, a minimum amount of OA, around 2 mmol to be specific, is required for it to partake in the formation of intermediate Fe^{3+}-complex. In addition, this intermediate complex arises around 200 ºC, temperature at which decomposition of $Fe(acac)_3$ occurs, independent of the present OA in the reaction.[196] As explained above, the step at 200 ºC is important to assure the total decomposition of $Fe(acac)_3$ and consequently obtain monodisperse NPs. Directly heating to 300 ºC from RT would lead to a slow nucleation and growth of nuclei, resulting in particles with a wide size distribution.[117] Now regarding OAm, it seems to act as a solvent, surfactant and reducing agent. However, there is a fundamental information gap for what concerns the detailed mechanisms of OAm in thermal decomposition.[111] Nonetheless, it is reported that in the absence of OAm, the particles present a poorly defined morphology and are highly polydispersive.[197] Moreover, the high boiling point of OAm (~ 364 ºC) offers a broad temperature range, enabling the realization of a complete study on the formation of MFe_2O_4 spinel ferrite dispersions in non-polar solvents.[118] Higher yields are obtained in presence of both OA and OAm, so typically, both are present.[117,198]

The heating ramp is also of crucial importance regarding the final particle size. A decrease in the heating ramp leads to a decrease in the nucleation rate, thus forming less nuclei and allowing their growth. Before nucleation, ligands are responsible for solubilizing the cations that will originate metal complexes, therefore stabilizing the oxidation state of the cation and avoiding undesired side reactions. Even after nuclei formation, ligands still regulate particle growth, their shape evolution, and stabilization in the solution. The absence of ligands bears the consequence of uncontrolled growth caused by the need to reduce the total surface energy as swiftly as possible, therefore originating large and irregular nanoparticles. Ligands dynamically adsorb on certain faces through interactions with the particle surface cations, thus diminishing their surface energy.[11] Heating ramps of 10 ºC.min^{-1} have demonstrated to be sufficient for obtaining highly monodispersive and spherical particles below 20 nm as reported in [64]. DBE was chosen in comparison to phenyl ether for example, due to its higher boiling point, being 298 ºC and 259 ºC, respectively.[117] This because higher reflux temperatures result in larger particles when compared with phenyl ether. Now regarding flux time, it is interesting to notice that an increase in reflux time results in a change of shape from spherical to cubic.[15,110] The thermal decomposition methodology reaction to obtain $Mn_xZn_{1-x}Fe_2O_4$ nanoparticles is described in Equation 2. A summary of the chemical composition as well as reaction conditions is shown in Table 9 (Appendix).

$$Mn(acac)_2 + Zn(acac)_2 + Fe(acac)_3 \longrightarrow Mn_xZn_{1-x}Fe_2O_4 + CH_3COCH_3 + CO_2 \quad \textbf{(Equation 2)}$$

Equation 2. Reaction of acetylacetonates precursors by thermal decomposition methodology.

According to the equation above, in the presence of OAm, OA, 1,2-HDO and DBE as solvent, the thermal decomposition of acetylacetonates results in the formation of the obtained $Mn_xZn_{1-x}Fe_2O_4$ nanoparticles, releasing acetone (CH_3COCH_3) and carbon dioxide (CO_2) as by-products. A similar equation was described in the synthesis of cobalt ferrites as demonstrated by Mahhouti and co-workers [197].

3.1.2. XRD pattern analysis

The diffractograms displayed in Figure 30 present well defined peaks of the spinel crystal structure of $Mn_xZn_{1-x}Fe_2O_4$ ferrite with their respective indexation, showing a predominant phase with the space group of $Fd\bar{3}m$ (ICDD no. 98002-8512 to 8516). XRD diffraction patterns of all compositions indicate a favorable growth along the (220), (311),

(400), (422), (511) and (400) directions, being in good agreement with the space group. From this diffractogram, it is deduced that all samples present a unique phase without detectable impurity phases within the detection limit of XRD. However, Fe_3O_4 can also be present since it belongs to the same space group and has approximately the same peak positions. The average crystallite sizes were calculated using Scherrer's formula and are listed in Table 9 (Appendix).

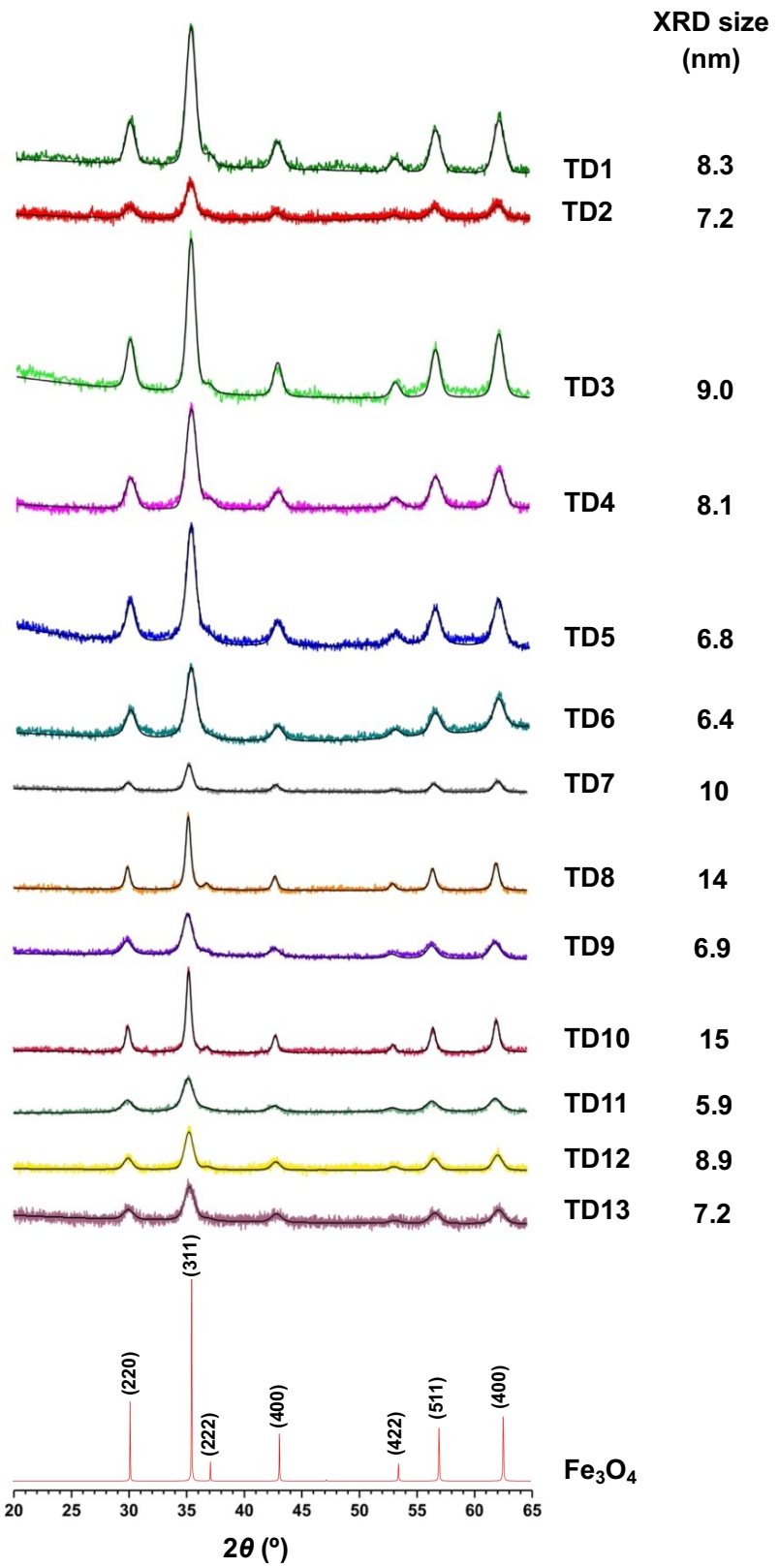

Figure 30. X-ray powder diffraction (XRD) patterns of $Mn_xZn_{1-x}Fe_2O_4$ and Fe_3O_4 NPs together with the indexation of Bragg peaks to a spinel structure. It is noteworthy that the colored lines correspond to experimental data collected whereas the black line represents the obtained Rietveld Refinement. Fe_3O_4 XRD pattern was obtained accessing Crystallography Open Database (COD), 9006189.

Comparing TD1 with TD3, and keeping in mind their synthesis conditions, it was expected to have similar sizes since the surfactants, as well as the solvent volume were the same. Despite TD2 possessing a higher concentration of zinc precursor, no unassigned reflection remains, thus not exhibiting zinc oxide formation within the limits of XRD which suggests a successful doping. Now establishing a comparison between TD5 and TD6, and knowing how they were synthetized, similar sizes were to be expected, since the same volume of solvents and surfactants were used. However, it was possible to conclude that although TD6 had zinc in excess, no zinc oxide was obtained indicating a well performed doping. Comparing TD8 with TD10 it is possible to conclude that while maintaining the surfactants concentration and the overall stoichiometric amounts of precursors, changing the volume of solvent did not influence the particle size. Comparing TD12 and TD13 it is possible to observe that maintaining the same precursors concentration, increasing OA and OAm results in smaller particle sizes, as reported in literature [116,196,197].

Lattice parameters (*a*) exhibit characteristic values of bulk magnetite (~8.4 Å)[118], and these suffer slight variations with changes in the composition, with a being between 8.3958 and 8.4427 Å (Table 10, Appendix). An increase in the lattice parameter suggests Zn^{2+} ions are incorporated into the tetrahedral coordinated A-sites in the spinel lattice, while a decrease of the lattice parameter implies that some of the Mn^{2+} ions are oxidized into Mn^{3+} ions, and therefore are incorporated at octahedral coordinated B-sites, substituting Fe^{2+} ions.[195] This information is in good agreement with the previously mentioned shift to higher angles.

In general, the apparent size obtained by Rietveld Refinement ranges from 5.9 to 15 nm as listed in (Table 10, Appendix). Since these NPs come in form of single domain, the apparent size can be considered the actual nanoparticle size. However, surface effects may hinder this conclusion, thus corroborating these findings with TEM is a better approach.

3.1.3. FT-IR spectroscopy analysis

Figure 31 evidences the FT-IR spectrum of a representative sample of $Mn_xZn_{1-x}Fe_2O_4$ NPs synthesized by thermal decomposition methodology (TD4 sample). FT-IR revealed the characteristic peaks of a spinel structure, in which metal-oxygen stretching modes of tetrahedral (A-site) and octahedral (B-site) symmetries are presented at 568 and 426 cm^{-1}, respectively.[172,199,200] Five absorption bands at 1411, 1549, 1598, 2851 and 2925 cm^{-1} appeared in FT-IR spectrum indicating the presence of OA.[199] The bands

at 2925 (ν_a C-H) , 2851 (ν_s C-H) and 1411 (δ_s C-H) cm^{-1} are known to be characteristic peaks of CH_2 chains present in OA. Specific to the OA spectrum is the carboxyl absorbance at 1710 cm^{-1}, which indicates that the molecule is present in dimmers held together by hydrogen-bonding.[201,202] However, it is worth noting that the band at 1710 cm^{-1}, corresponding to C=O asymmetric stretching vibration of OA was absent in the spectrum, which indicates that the molecules are chemisorbed onto MNPs surface as a carboxylate. Instead, two new bands at 1414 and 1549 cm^{-1} appeared and thus they were attributed to the asymmetric ($-COO^-$) and symmetric ($-COO^-$) stretch vibration band, respectively.[199,200,202,203] In the OAm spectrum the most characteristic peak is the 787 cm^{-1} absorbance which can be ascribed to a NH_2 wagging vibration[198,201], which shifted as a slight peak at 716 cm^{-1} probably caused by the absorption of N-H groups onto the MNPs surface due to Van der Waals interactions.[172,200,202] Two absorption bands at 1447 cm^{-1} and 1621 cm^{-1} were assigned to the bending vibrations of the $-CH_3$ and –C=C of oleylamine, in that order.[172,198] The broad peak from 2978 to 3669 cm^{-1} points to trace amounts of water in the pellet.[201]

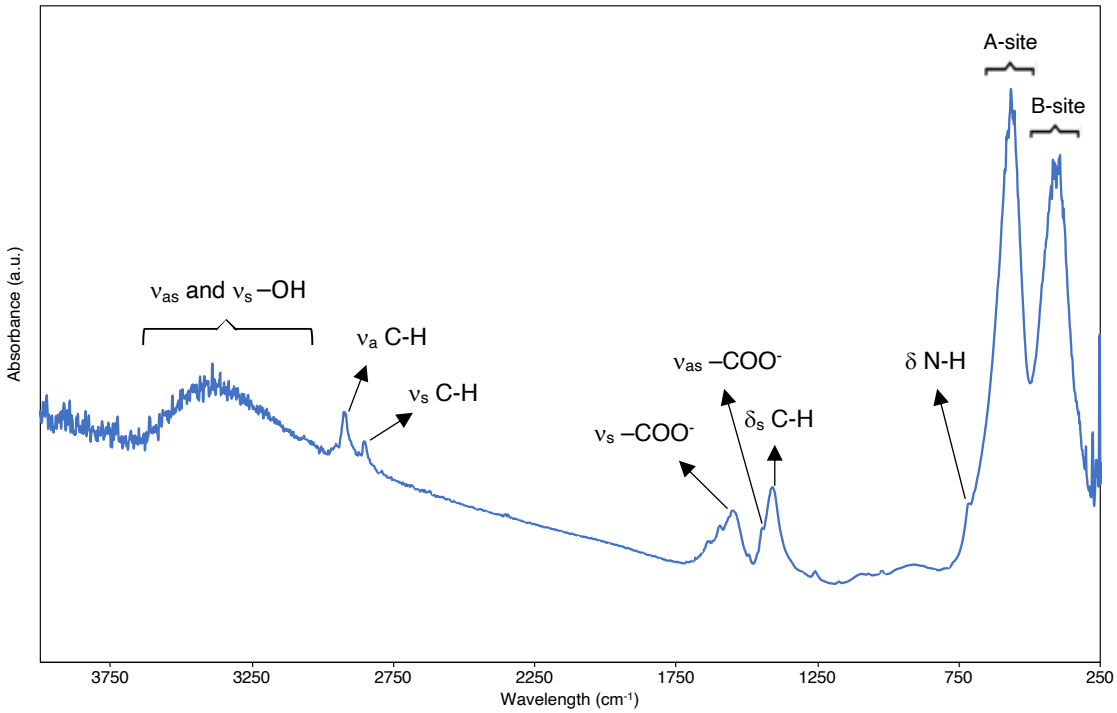

Figure 31. Infrared spectrum of a representative sample of $Mn_xZn_{1-x}Fe_2O_4$ nanoparticles synthesized by thermal decomposition (TD4 sample).

To conclude, the presence of OA and OAm coating was verified by FT-IR as shown on Figure 31. It is noteworthy that the washing methodology for these

nanoparticles should be optimized in terms of the type of solvents used or mixture of solvents as well as centrifugation time and/or rotation speed.

3.1.4. SEM-EDS analysis

SEM micrographs are displayed in Figure 32. Due to the challenging sample preparation, it is not possible to distinguish individual nanoparticles regardless of the amplification, thus agglomerates of nanoparticles are observed. Despite the agglomeration of NPs, they seem to present a spherical morphology with a smooth surface. To assess the presence of metals, EDS analysis has been performed. In Table 10 (Appendix) are reported the chemical formula, the equivalent number and the EDS results. It is known that EDS only reveals the presence of elements in a sample. As expected, the survey spectra demonstrated the presence of only Fe, O, Mn and Zn in the nanoparticles. By observing Table 10 (Appendix), it is clear that doping was achieved in all the samples. For $\varkappa$ = 0.13, the desired composition was obtained by adjusting the reagents ratio, whereby using $Mn_{0.12}Zn_{0.77}Fe_2O_4$ and $Mn_{0.17}Zn_{1.73}Fe_2O_4$, the final compositions of $Mn_{0.11}Zn_{0.78}Fe_2O_4$ and $Mn_{0.13}Zn_{0.77}Fe_2O_4$ were obtained, respectively. As for $\varkappa$ = 0.35, the desired compositions were obtained with regard to Zn by adjusting the reagents, with Zn as the excess. From these experiments, by using $Mn_{0.36}Zn_{0.82}Fe_2O_4$ and $Mn_{0.35}Zn_{0.64}Fe_2O_4$, the compositions of $Mn_{0.14}Zn_{0.54}Fe_2O_4$ and $Mn_{0.18}Zn_{0.58}Fe_2O_4$ were achieved. Lastly, for $\varkappa$ = 0.60 it can be said that achieving the desired compositions was significantly more difficult, as the closest final compositions to the intended were $Mn_{0.42}Zn_{0.65}Fe_2O_4$ and $Mn_{0.30}Zn_{0.47}Fe_2O_4$ by using an initial composition of $Mn_{0.80}Zn_{0.84}Fe_2O_4$ and $Mn_{0.64}Zn_{0.97}Fe_2O_4$, respectively. To conclude, it can be said that as the $\varkappa$ value increases, or in other words, attempting to increase the Mn content, more difficulty is encountered in the doping process.

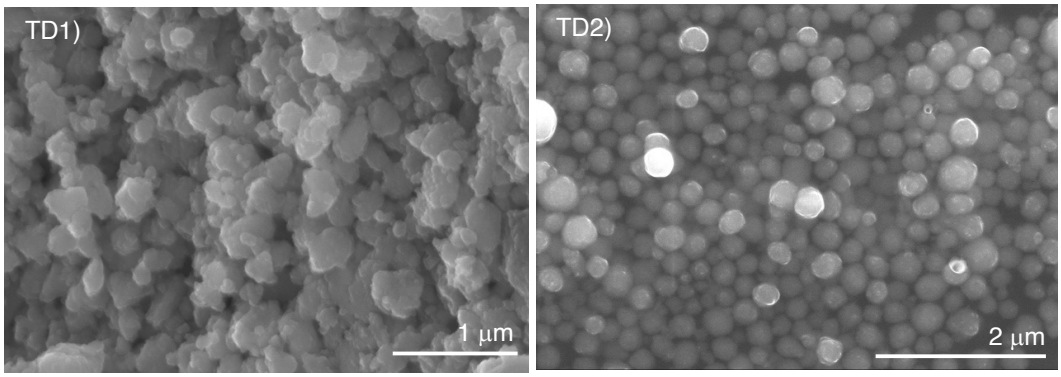

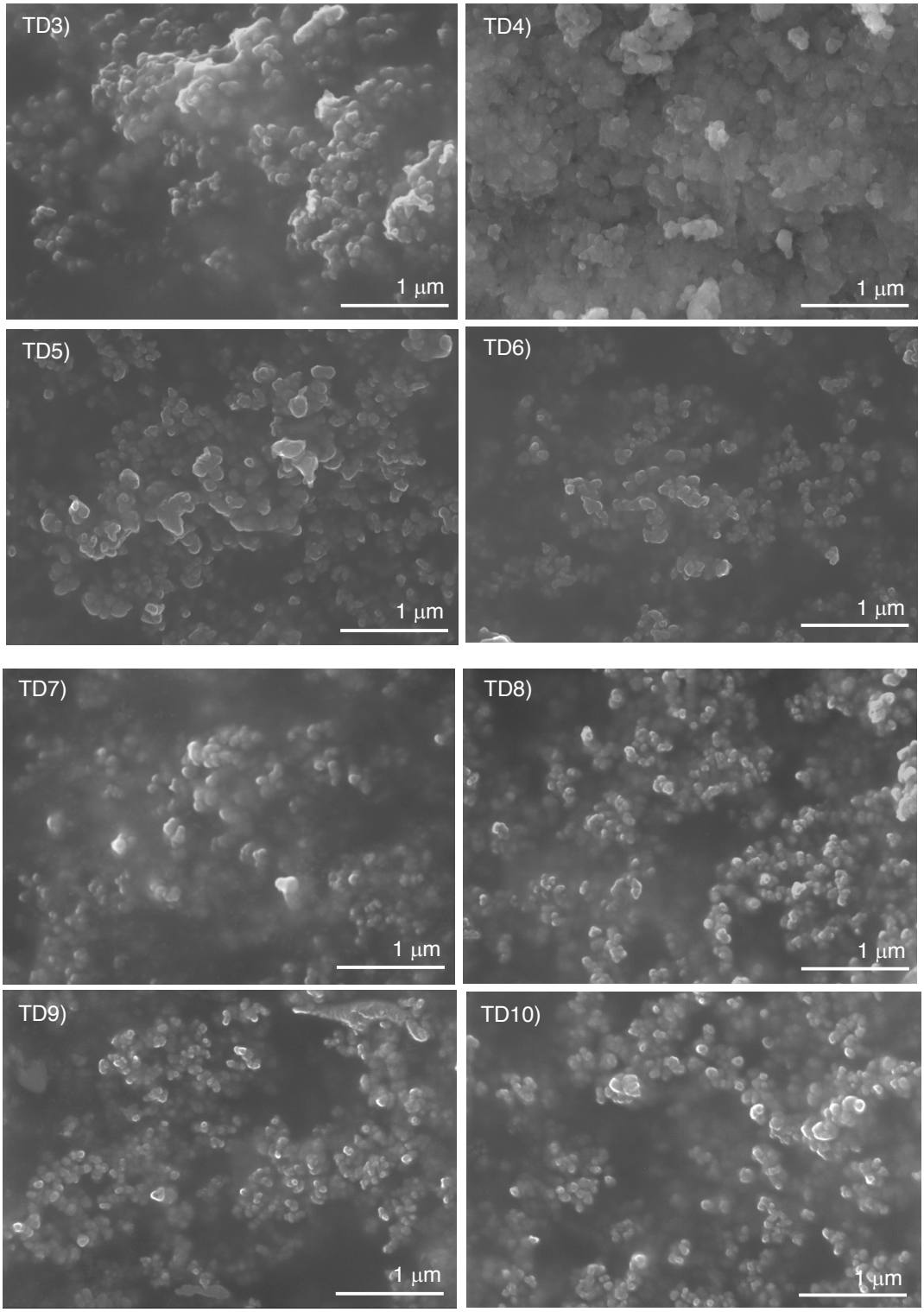
TD3)
1 μm
TD4)
1 μm
TD5)
1 μm
TD6)
1 μm
TD7)
1 μm
TD8)
1 μm
TD9)
1 μm
TD10)
1 μm

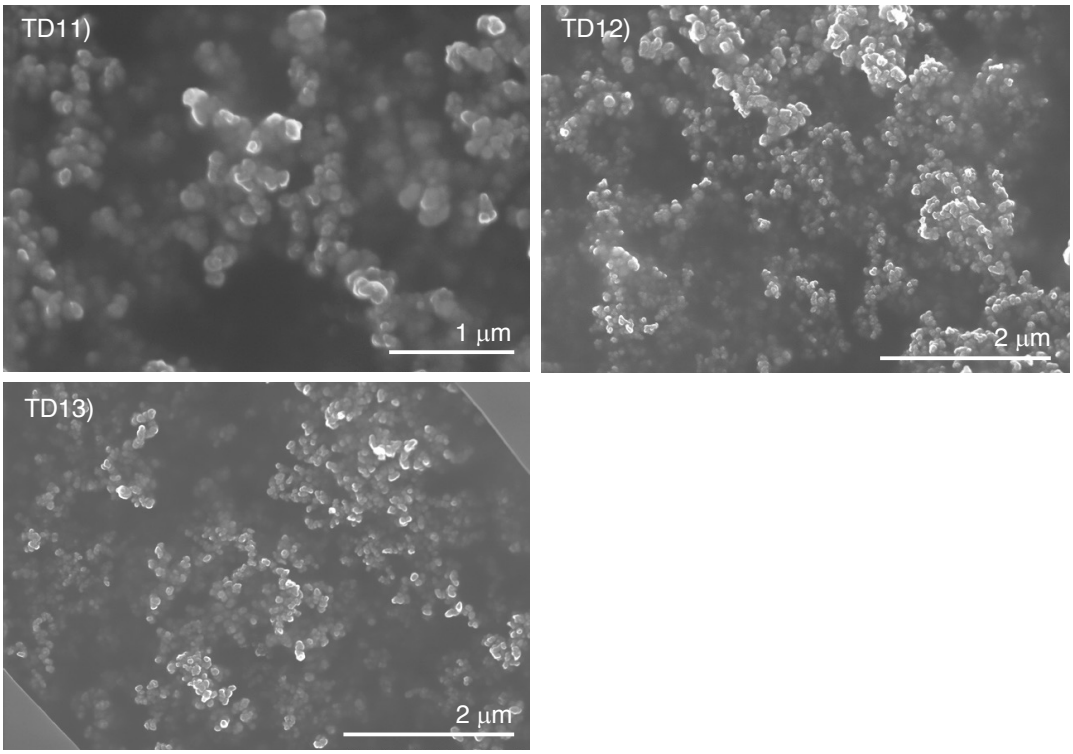

Figure 32. SEM micrographs of $Mn_xZn_{1-x}Fe_2O_4$ NPs: a) TD1, b) TD2, c) TD3, d) TD4, e) TD5, f) TD6, g) TD7, h) TD8, i) TD9, j) TD10, k) TD11, l) TD12 and TD13 sample.

3.1.5. TEM measurements analysis

The transmission electron microscopy (TEM) micrographs of the samples are shown in Figure 33. From them, it can be concluded that the NPs have a homogeneous size. It is also possible to conclude that this methodology provides great control over the NPs shape. In contrast with SEM analysis, the particles here appear well-individualized, suggesting that SEM may possess some technical limitations in comparison to TEM. The morphology of the nanoparticles is similar between compositions, possessing a spheric shape, also similar to the samples reported elsewhere.[121,122] Figure 33 shows that the NPs are highly crystalline, and the crystal lattice fringes are clear in throughout the whole nanoparticle. In addition, the average particle size obtained by TEM is nearly identical to that obtained from XRD measurements, suggesting that each nanoparticle has a single-domain structure. The results obtained were in agreement with the ones reported in literature.[57,102,172,203] The size distribution histogram was fitted to the Gaussian function and the derived average sizes were listed in Table 10 (Appendix).

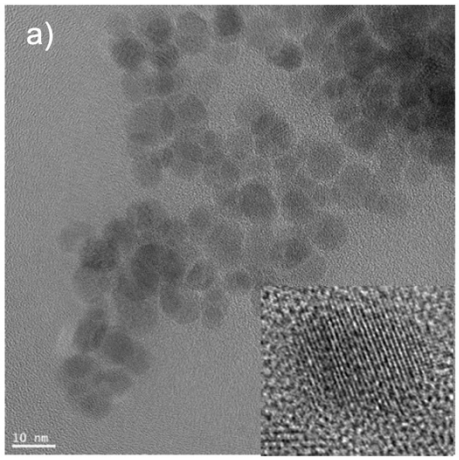
a)
10 nm

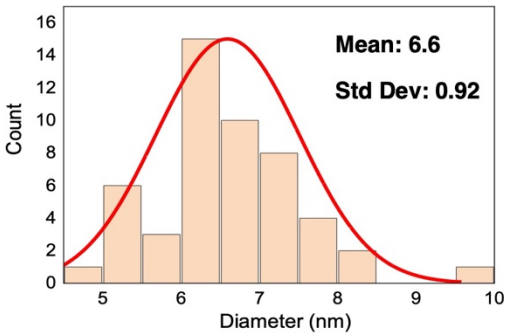
Mean: 6.6
Std Dev: 0.92
Count
Diameter (nm)

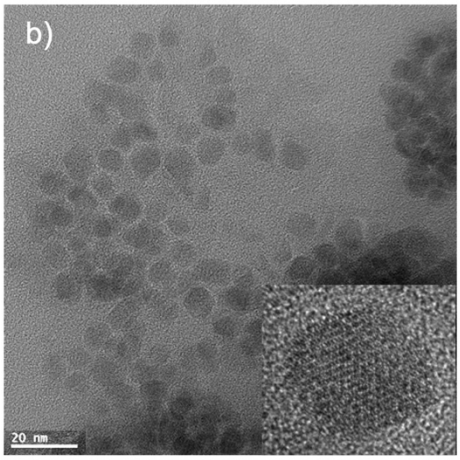
b)
20 nm

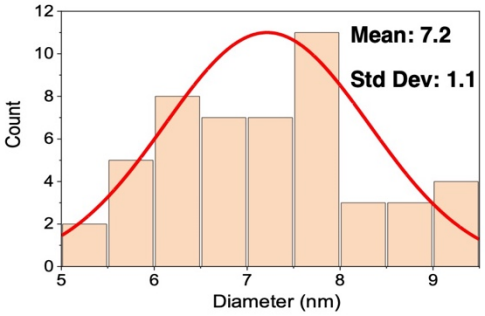
Mean: 7.2
Std Dev: 1.1
Count
Diameter (nm)

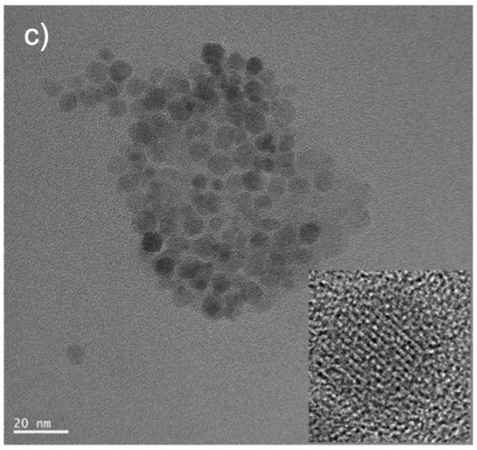
c)
20 nm

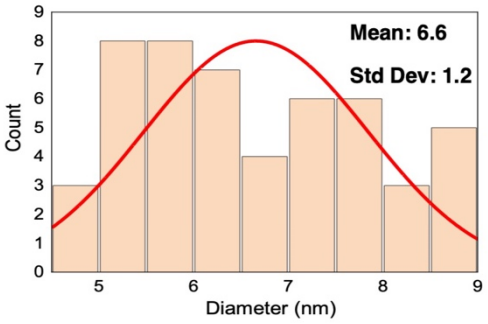
Mean: 6.6
Std Dev: 1.2
Count
Diameter (nm)

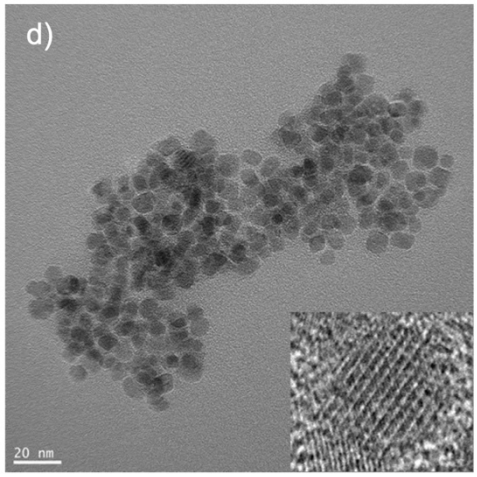
d)
20 nm

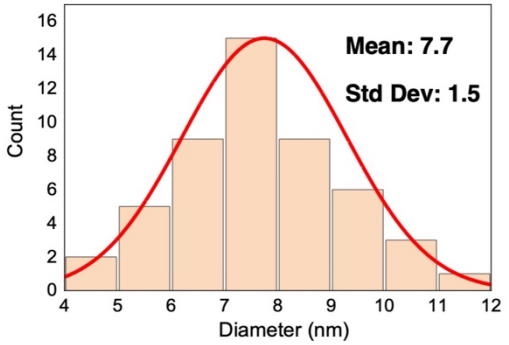
Mean: 7.7
Std Dev: 1.5
Count
Diameter (nm)

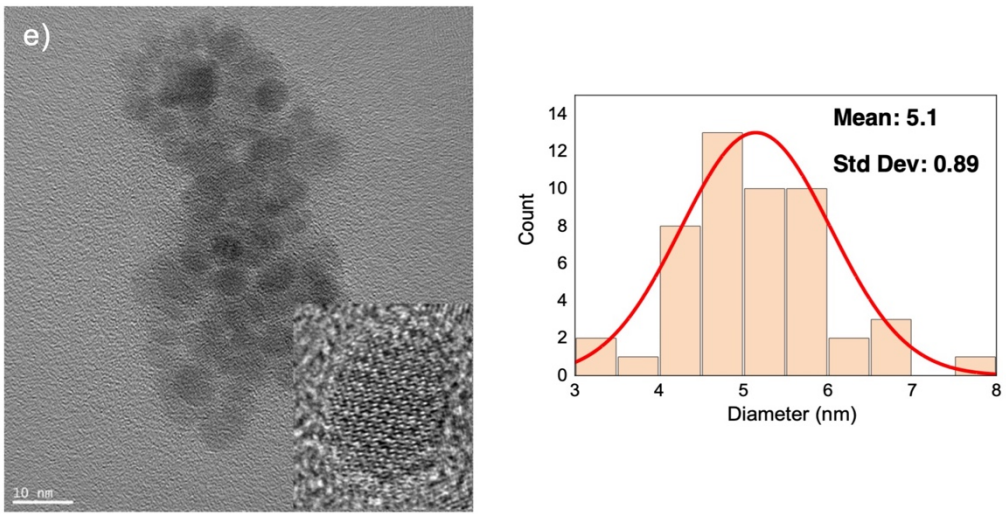

Figure 33. TEM micrographs of $Mn_xZn_{1-x}Fe_2O_4$ NPs synthesized by thermal decomposition methodology: a) TD4 sample, and b) TD9 sample, c) TD11, d) TD6, e) TD13. The inset shows the histogram of size distribution of MNPs which as obtained from TEM data to approximate a Gaussian distribution. The legend is supplemented by the mean diameters and the standard deviation, both evaluated from experimental values.

3.1.6. Magnetic measurements analysis

Interest in intracellular mapping through nanothermometers has bolstered the attention of the research community.[4,204–206] Nanothermometers present several advantages when compared to thermometers without micro and nanoscale such as: *(i)* easy synthesis and high controlled purity, since they are synthesized from pure precursors, *(ii)* low processing temperature and thus reduction of the synthesis costs, and *(iii)* improved mechanical stability.[4] As mentioned in the previous sections, hoping to gain a better understanding of cellular events based on nanothermometers, temperature dependent Mn-Zn ferrites NPs were developed by thermal decomposition methodology (samples TD9 and TD4). Regarding sample TD9, these NPs revealed to work in a range of 150 to 375 K with a maximum sensitivity value $|S_m|$ equal to 2.9 %.K^{-1} at 225 K as shown in Figure 34. Most luminescent-based thermometers possess temperature ranges above the ambient temperatures. However, a select few possess temperature ranges suitable for hyperthermia and cryopreservation applications. Such is the case of Eu^{3+}/Tb^{3+} b-diketonate complex embedded into silica-coated magnetic NPs, which possess the larger temperature range of 10 to 330 K with a S_m of 4.9 %.K^{-1} at 143 K.[4] As for the highest S_m value found in literature with a temperature range englobing room temperature, it results from a mutant of *lacI,* with a value of 19.6 %.K^{-1} at 318 K regarding a temperature range of 308 to 318 K.[4]

For the applications in question, however, the NPs require proper sensitivity within a broad temperature range englobing the temperatures experienced in both hyperthermia and cryopreservation procedures, which in turn can be considered in the following temperature intervals: 310 to 317 K for hyperthermia and 123 to 310 K for cryopreservation.

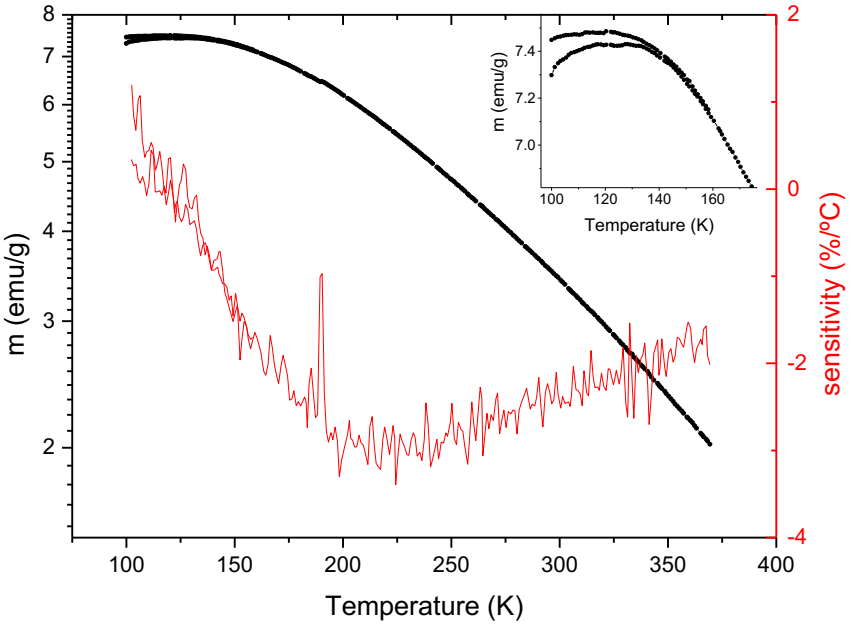

Figure 34. ZFC-FC susceptibility curves for TD9 sample as well as temperature dependence of the relativity sensitivity values. The minus signal gives an indication that the thermometric parameter (magnetization, in this case) is decreasing.

In the Figure 34 presented above, variation of magnetism according to temperature is displayed. The red line represents the calculated sensitivity of NPs with reversible behavior, while the black line represents the temperature dependence of magnetization. NPs with a normal superparamagnetic behavior exhibit a very small variation of magnetization over the established temperature range, while the produced NPs show a steep decrease in magnetism over the same temperature range, or in other words, a greater variation in magnetization in the same temperature interval. This leads to the conclusion that the produced NPs display a greater sensibility than standard superparamagnetic materials. In fact, the ability to control the composition of MIONs by doping is reflected by the direct improvement of magnetic behaviors, which in turn allows the development of high-sensitivity sensors with high M_S.[150]

Regarding FC and ZFC curves, displayed in the small box in the corner of Figure 34, these merge together after 150 K, meaning that the produced NPs exhibit a reversible

response above said temperature. This implies that whether the NPs have been heated after being previously cooled without the application of a magnetic field, or after cooling with an applied field, the response will be the same, which is constitutes a desirable property in nanothermometers. ZFC-FC curves analysis show that T_B is below RT, revealing that the particles are superparamagnetic at RT.[118] These findings are also supported by Pardo and colleagues.[64]

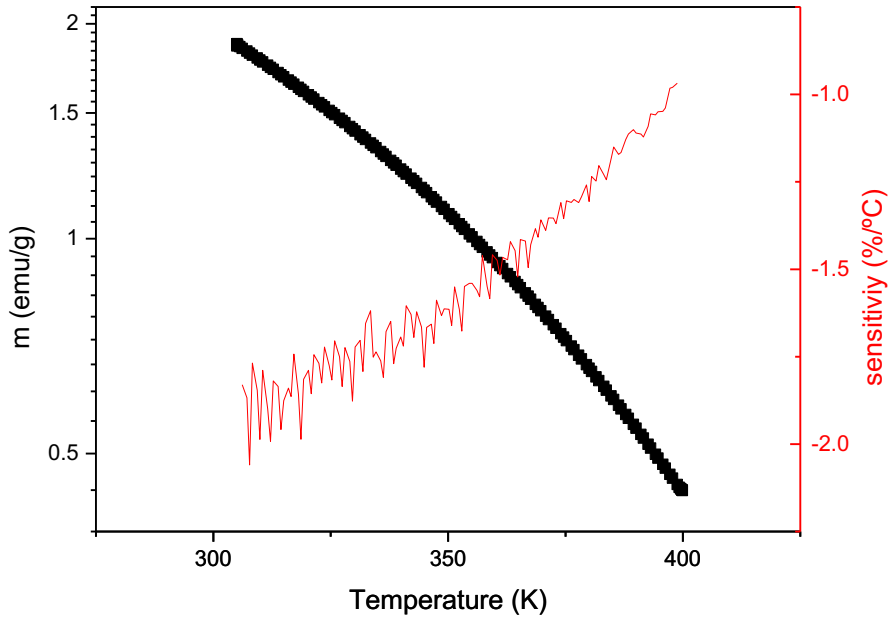

Figure 35. ZFC-FC susceptibility curves for TD4 sample as well as temperature dependence of the relativity sensitivity values. The minus signal gives an indication that the thermometric parameter (magnetization, in this case) is decreasing.

Now with respect to the TD4 sample, it revealed $|S_m|$ equal to approximately 2.1 $\%.K^{-1}$ at 300 K as shown in Figure 35.

Despite only two magnetic measurements being performed, it is expected that all the as-prepared particles show superparamagnetic behavior at RT. Additionally, in general MNPs with less zinc content are expected to have less sensitivity. A plausible explanation may rely on the fact that Zn^{2+} ions do not possess intrinsic magnetic moment, thus breaking the antiferromagnetic coupling between Fe^{3+} ions at tetrahedral and octahedral sites, which consequently increases the magnetization under applied magnetic fields, and since Zn^{2+} ions possess a smaller size in comparison to iron, an increase in H_c by zinc doping is not expected. This was also addressed by the work developed by Pardo and co-workers.[64]

To conclude, the hereby developed thermometers possess a relatively wide temperature range with proper sensitivity, showing promise for the evaluation of processes occurring within their temperature ranges. Moreover, their magnetic properties make them independent of optical transmission, enabling them to measure temperature at greater depths in a wireless manner. Regarding their intended applications, sample TD9 is suitable for hyperthermia and cryopreservation thermometry since it presents a reversible variation in magnetic response of *ca.* 1 %.K^{-1} between 300 and 350 K and a variation of *ca.* 2 %.K^{-1} between 150 and 225 K, respectively. Sample TD4 is also suitable for both applications, however, in comparison to sample TD9, it presents a lower sensibility as a thermometer, demonstrating a reversible magnetic response variation of *ca.* 1 %.K^{-1} between 300 and 400 K.

3.1.7. Final remarks

$Mn_{\varkappa}Zn_{1-\varkappa}Fe_2O_4$ NPs ($\varkappa$ = 0.13, $\varkappa$ = 0.35, and $\varkappa$ = 0.60) were successfully synthesized by a two-step thermal decomposition methodology. XRD patterns confirmed the formation of $Mn_{\varkappa}Zn_{1-\varkappa}Fe_2O_4$ NPs with cubic spinel structure in all samples. In addition, no impurities were detected within the XRD limits. The effect of different contents of surfactants and solvent volume were also tested, however, only differences on crystallinity and small variations in size were exhibited. In addition, the calculation of the crystallite size by XRD resulted in values ranging from 5.9 and 15 nm, while the NPs size from TEM proved to be between 6 and 7 nm. Moreover, the morphology of the NPs was studied by SEM and TEM, however, due to the limitations of SEM, TEM was a much more reliable tool for morphology assessment, where it can be concluded that the particles possessed a spherical shape.

3.2. Molten salts methodology

3.2.1. Synthesis results analysis

In comparison to the aforementioned conventional methodologies, molten salts technique possesses a lower product formation temperature as it enhances the fast movement of solids in liquid molten salt phase through convection and diffusion. This methodology distinguishes itself from other synthesis systems by the facile destabilization of ionic/covalent bonds through the use of solvents due to the strong polymerization caused by molten salts at high temperatures.[108] In addition, molten salts technique possess high aqueous solubility, thus favoring their removal at the end of

chemical reaction with ease and enabling an efficient product isolation from the synthesis reaction mixture. The molten salts methodology is widely explored in laboratory research by being a simple, green, scalable, cost efficient, versatile nanomaterial synthesis technique due to its low toxicity, cost effectiveness, low vapor pressure, easy availability, high heat capacity, large electrochemical range, and high conductivity. In addition to these appealing features, this technique stands out in comparison to its peers due to the reduction of product formation temperature and its efficiency in the synthesis of uniform particles. Salts such as KNO_3 play a very important role in molten salts processes by enhancing the chemical reactivity of reactant species, lowering synthesis temperature, decreasing the degree of agglomeration in the final product, and generating a homogeneous final product powder.[108] Thus, KNO_3 was chosen for this work due to its easy availability, low reactivity, and high aqueous stability so that it can be easily removed by simply washing the product of the synthesis with water.[108] In this procedure, 10 equivalents of KNO_3 were used for every equivalent of $Mn(NO_3)_2{\bullet}\varkappa H_2O$. During the calcination process the product will form a "film" which is deposited at the bottom of the crucible due to its rugosity. This "film" significantly decreases the final yield of the reaction and unfortunately its formation is impossible to prevent when using this type of crucible sample holder. However, through this work it could be observed that with less KNO_3 the removal of the powder from the crucible became more difficult. In addition, not only was the yield of the reaction greatly lowered, but other crystalline phases were obtained as well. Thus, suggesting that the adequate amount of KNO_3 improves the reaction outcome. The precursors were milled inside a mortar with a few drops of absolute ethanol since it will have great affinity to the water present in the "molten salt". Thus, during the evaporation of EtOH (when the crucible is placed on the hot plate), water will also "leave" the molten salt along with the EtOH. This prevents the formation of undesired metal oxides during the calcination process and the contamination of the nanoparticles with undesired phases.

Concerning the ferrites reported in literature (mentioned on the *Chapter 1.6.3*), to the best of our knowledge, there are no studies regarding Mn-Zn ferrite synthesis by molten salts, With this said, this work aimed to be the pioneer in this regard by combining a methodology that follows the Green Chemistry principles[108] leading to the development of ferrites at a relatively low temperature. In this experiment, raw materials such as $Mn(NO_3)_2{\bullet}\varkappa H_2O$, $Zn(NO_3)_2{\bullet}6H_2O$, and $Fe(NO_3)_3{\bullet}9H_2O$ were mixed according to the Mn and Zn content then calcinated at 500 ºC for 2 h to synthetize $Mn_{\varkappa}Zn_{1-\varkappa}Fe_2O_4$ NPs. The herein developed method for the production of Mn-Zn ferrites by molten salts presents a

relatively low reaction temperature in comparison to other reported molten salts works that use temperatures ranging from 800 – 1300 ºC.[125–127] In addition, a reaction time of 2 h at a temperature of 500 ºC is a promising factor regarding reaction times evidenced by other researchers, suggesting a more efficient approach. Lou *et al.* discussed the important role of temperature in molten salts synthesis of $MgFe_2O_4$ and how it affects the yield of the produced particles, verifying that for reactions occurring at different temperatures such as 760 and 860 ºC, yields of 60 and 75 % were obtained, respectively.[126] With this in mind, the herein obtained yields of the as-synthetized NPs ranges from 43.4 to 54.0 %, thus following the same line of thought, wherein lower reactional temperatures tend to result in lower yields.

3.2.2. XRD pattern analysis

The X-ray diffraction technique was used to determine the present phase on the $Mn_xZn_{1-x}Fe_2O_4$ NPs. The respective diffractograms of as-prepared NPs as well as the corresponding Rietveld Refinement are depicted in Figure 36. These results confirm that the molten-salt methodology is an effective method for the formation of the $Mn_xZn_{1-x}Fe_2O_4$ NPs at relatively low-temperature.

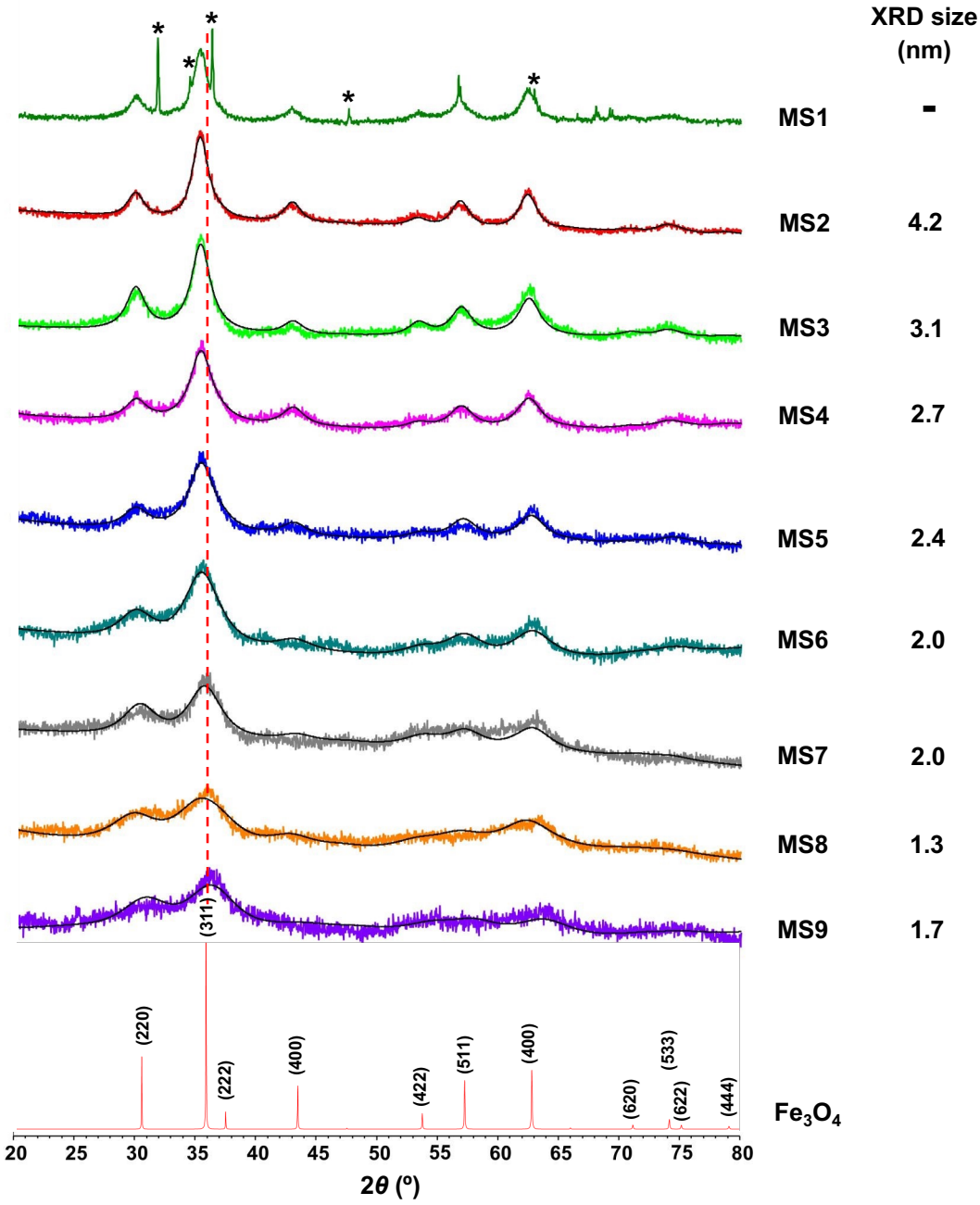

*Figure 36. X-ray diffractogram patterns of $Mn_xZn_{1-x}Fe_2O_4$ and Fe_3O_4 NPs together with the indexation of Bragg peaks to a spinel structure. The colored lines correspond to experimental data collected whereas the black line represents the obtained Rietveld Refinement. ZnO impurity peaks are represented by *. Fe_3O_4 XRD pattern was obtained accessing Crystallography Open Database (COD), 9006189.*

As displayed in Figure 36, all diffraction peaks can be indexed to a cubic lattice, matching the standard $Fd\bar{3}m$ cubic spinel structured Mn-Zn ferrite diffraction data (ICDD no. 98002-8512 to 8516). All samples present a unique phase, except for $Mn_{0.1}Zn_{0.9}Fe_2O_4$, meaning that they do not contain impurity phases within the detection limit of XRD. The sample $Mn_{0.1}Zn_{0.9}Fe_2O_4$ presented zinc oxide (ZnO), and thus we were

able to conclude that the maximum doping composition for zinc in Mn-Zn ferrite is *ca.* 0.8 when prepared by this method. Fe_3O_4 can also be present in the samples, but it is not distinguishable from Mn-Zn ferrite diffractogram, as previously mentioned. As the zinc composition increases, the diffraction peaks become narrower, indicating the increase of crystallinity as well as apparent size, which is in agreement with previous synthesis reports using the molten salts methodology.[207] However, the sample $Mn_{0.8}Zn_{0.2}Fe_2O_4$ has an apparent size of 1.3 nm while the sample $Mn_{0.9}Zn_{0.1}Fe_2O_4$ presented an apparent size of 1.7 nm, which can be explained by a weak fitting in the XRD diffractogram refinement calculations in both samples.

Now regarding the lattice parameters (*a*), these present the typical values of bulk magnetite (~8.4 Å)[118], varying slightly by changing the composition, with a exhibiting values between 8.3238 and 8.4176 Å (Table 12, Appendix). Aforementioned, an increase in the a value demonstrates that Zn^{2+} ions are incorporated into the tetrahedral coordinated A-sites in spinel lattice, whereas its decrease suggests Mn^{2+} ions are oxidized into Mn^{3+} ions, and incorporated into octahedral coordinated B-sites, replacing Fe^{2+} ions.[195] Again, this data is in accordance with the previously mentioned shift to higher angles.

Previously we mentioned that the peaks are sharper and more intense for nanoparticles with higher zinc content. A closer look at the (311) reflection in the XRD patterns (Figure 36) showed that it is slightly shifted to smaller angles, specially from MS1 to MS6 sample, which could be attributed to the difference of Zn^{2+} and Mn^{2+} ionic radii, being 0.74 nm and 0.83 nm, respectively.[192] However, the shifting distances of the peaks are not equal, suggesting that the shifts are not originated by baseline drift during data collection.[208] This structural results are also in concordance with the synthesis of Mn-Zn ferrites performed by Liu and co-workers.[207] Noteworthy, the diffractogram shows broad and overlapping diffraction peaks for higher manganese content. Mamani *et al.* also experienced a similar occurrence regarding the synthesis of Fe_3O_4 NPs, due to the low crystallinity of the as-prepared NPs.[209] For these reasons, alternatives such as the Mössbauer spectroscopy[210] or X-ray photoelectron spectroscopy (XPS)[211] technique can give insight on the cation distribution and the electronic state of each constituting atom, respectively. Furthermore, these techniques are sought out as they can individualize these oxides and gather measures with sensitivity to the surrounding chemical elements, thus improving the identification of the formed phases.[212,213]

In general, the average crystallite sizes obtained by Rietveld Refinement ranges from 3.0 to 7.8 nm as listed in Table 12 (Appendix). Since these NPs come in form of

single domain, the apparent size can be considered the actual nanoparticle size. However, surface effects may hinder this conclusion, thus corroborating these findings with TEM is a better approach.

3.2.3. FT-IR spectroscopy analysis

The FT-IR spectra of all as-synthesized $Mn_xZn_{1-x}Fe_2O_4$ NPs by molten salts methodology are shown in Figure 37 and reveals the characteristic peaks of a spinel structure, in which metal-oxygen stretching modes of tetrahedral (A-site) and octahedral (B-site) symmetries are presented at 572 and 459 cm^{-1}, respectively. Of note, the band around 1548 cm^{-1} and the broad peak from 2664 to 3647 cm^{-1} represent the characteristic hydroxyl group (–OH), pointing to trace amounts of water absorbed after calcinations. It is also worth to mention that a shift on the intrinsic absorption bands may occur due to the substitution Zn^{2+} ions with Mn^{2+} ions, which possess an ionic radius of 0.74 and 0.83 nm[192], respectively. This substitution leads to a decrease in the bond length at tetrahedral sites, and it is known that the frequency of vibration varies inversely with the bond length.[192] With all this taken into consideration, these results are in good agreement with the work performed by Wu *et al.*, which also experienced a similar shift, as described here.[214], as well as with the work done by Varshney and co-workers[215]. The band situated around 1620 cm^{-1} can be attributed to the characteristic hydroxyl groups (–OH) due to humidity in the samples.[214] Now regarding the bands around 1420 and 1550 cm^{-1}, these can be assigned to the presence of trapped NO^{3-} in the produced NPs, although a notable shift from the expected wavenumber is displayed.[215]

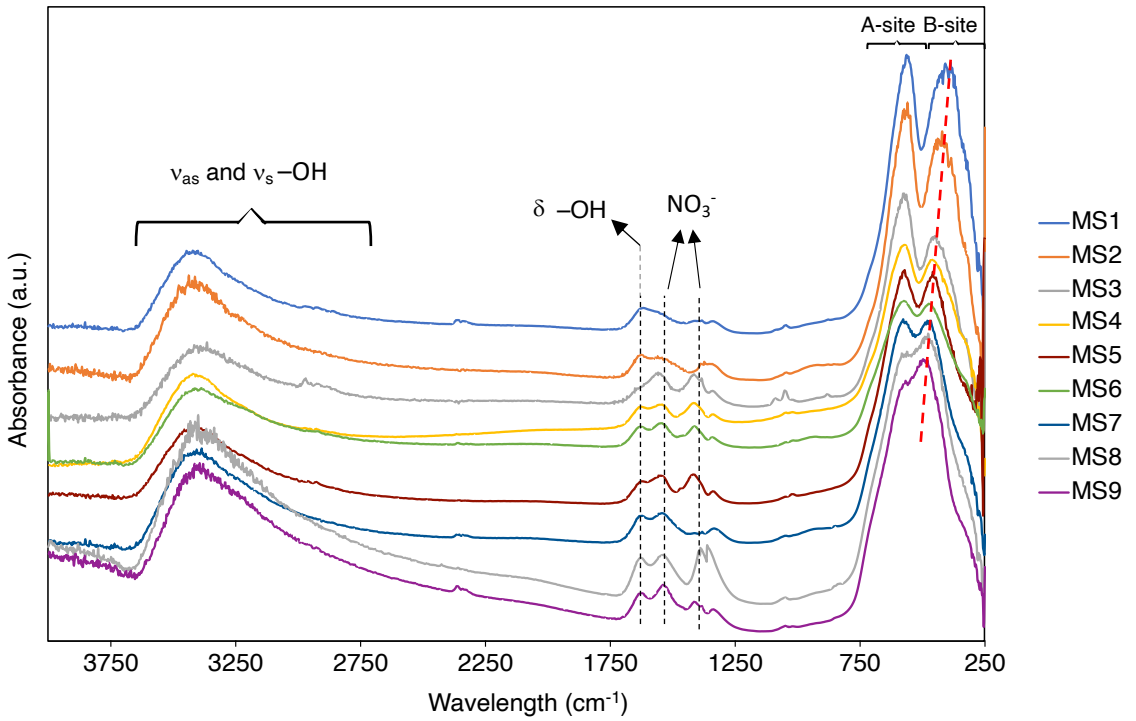

Figure 37. Infrared spectra of $Mn_xZn_{1-x}Fe_2O_4$ nanoparticles synthesized by molten salts methodology.

3.2.4. SEM-EDS analysis

SEM micrographs are displayed in Figure 38. As evidenced, due to the difficulties inherent to sample preparation, individual nanoparticles cannot be distinguished regardless of amplification, and although agglomerates of nanoparticles are shown, they seem to exhibit a spherical morphology and a smooth surface.

The elemental chemical composition of the $Mn_xZn_{1-x}Fe_2O_4$ NPs was evaluated by EDS analysis. By analyzing Table 12 (Appendix) it is notable that the chemical composition inferred from EDS is similar to the expected stoichiometry. Both Mn and Zn obtained by this technique were easily incorporated, with almost no deviation from the expected stoichiometry.

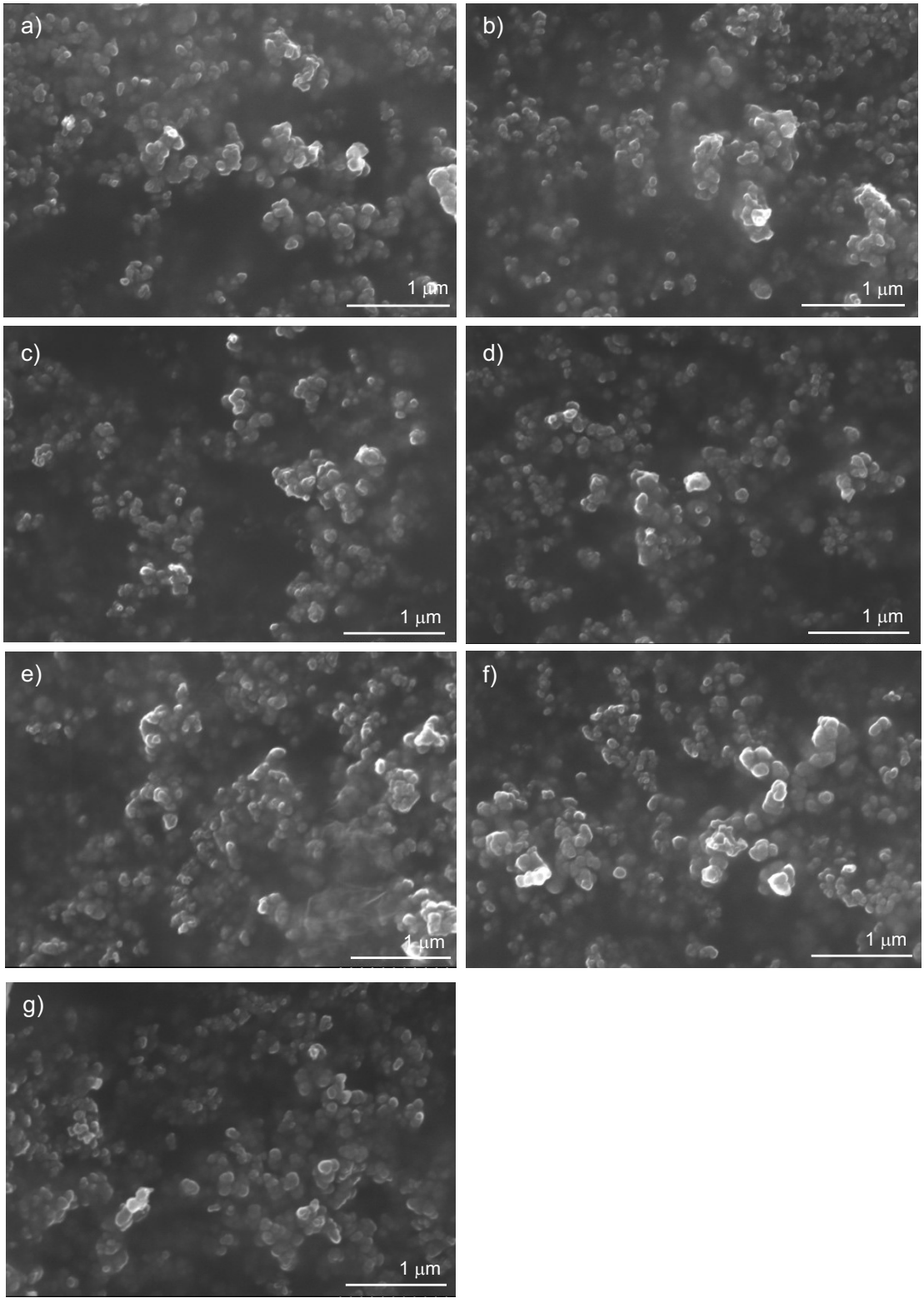

Figure 38. SEM micrographs of a) MS2, b) MS3, c) MS4, d) MS5, e) MS6, f) MS7, g) MS8, and h) MS9 NPs samples.

3.2.5. TEM measurement analysis

TEM micrographs of the samples are displayed in Figure 39 and the average particle sizes are listed in Table 12 (Appendix). The presented micrographs only served to confirm the presence of NPs. However, regardless of amplification, it is observed that the images do not allow a clear view of individualized NPs, and although they mostly show a spherical shape, some tend to be elongated. This may be due to the extremely small size of the NPs, or also due to the fact that in this synthesis, no surfactants such as OAm and OA were used, since they prevent NP aggregation. In addition, in these micrographs we cannot visualize crystal lattice fringes, which is in accordance with the analysis presented by XRD, since the samples exhibit small crystallites. When comparing SEM and TEM analysis, it is evident that with TEM conclusions regarding particle individualization can be made, while in SEM this is not possible.

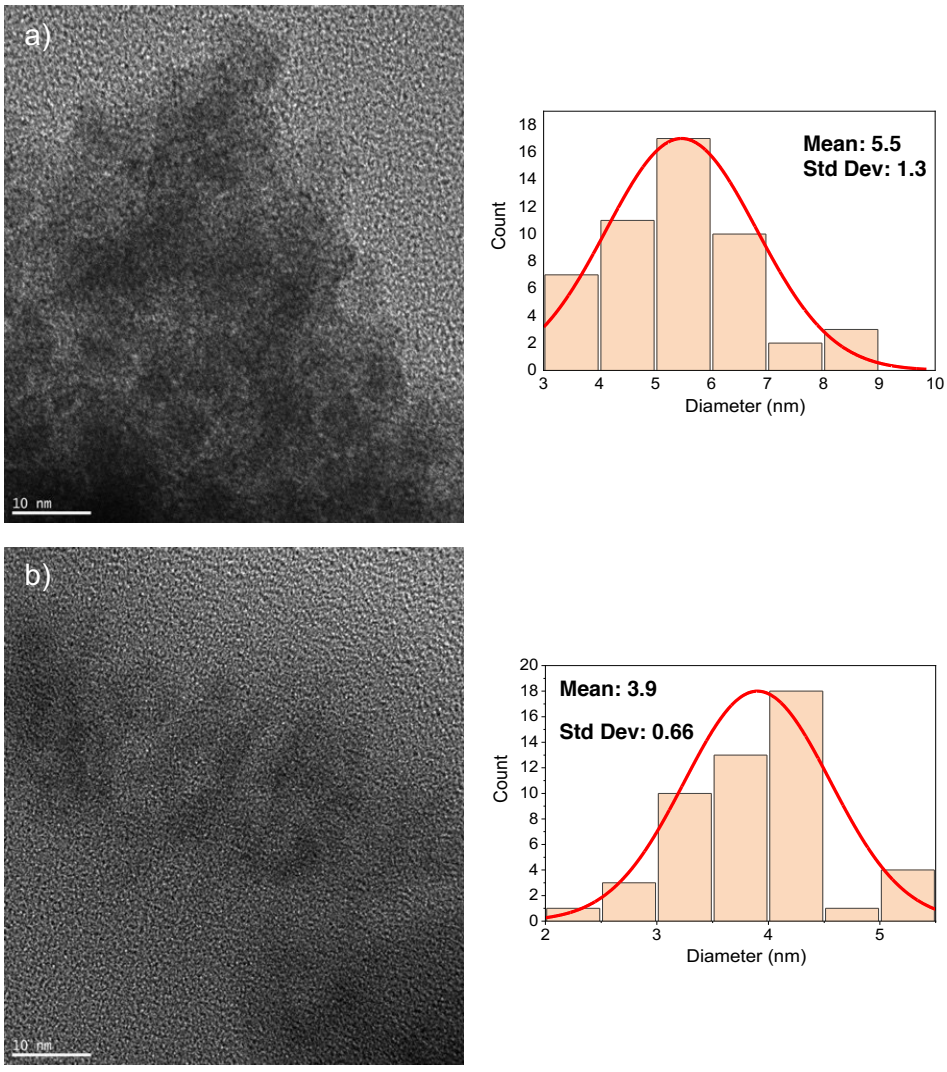

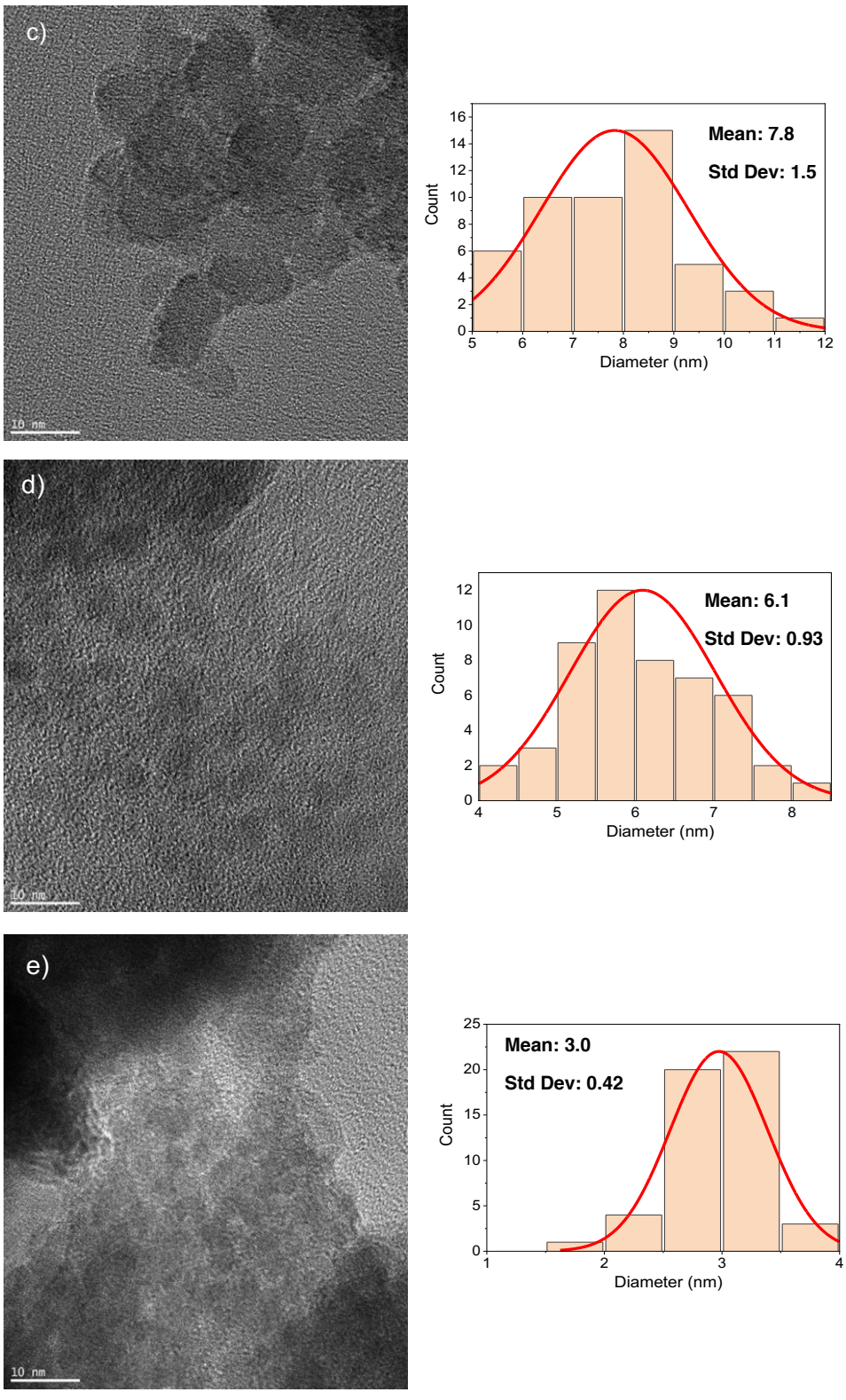

Figure 39. TEM micrographs of representative $Mn_xZn_{1-x}Fe_2O_4$ NPs synthesized by molten-salts methodology: a) MS3, b) MS4, c) MS5, d) MS6, and e) MS9 sample.

3.2.6. Final remarks

Motivated by the lack of thermal decomposition methods for the synthesis of Mn-Zn ferrites, a novel method was developed to synthetize Mn-Zn ferrites designated molten salts-assisted thermal decomposition. This method is advantageous as the synthesis does not require neither solvents or surfactants, and the washing of the NPs can be done solely with distilled water, thus improving practical efficiency. In turn, the temperatures used in this novel strategy may be explored at much higher values than possible in a thermal decomposition methodology, which in turn is limited either the melting point or boiling points of the surfactants and solvents involved. In truth, despite the fact that this is the first synthesis of Mn-Zn ferrites by this methodology, in comparison to other already developed MNPs, this methodology presents much lower reactional temperatures than those mentioned in other reports.[125–127] With this in mind, $Mn_xZn_{1-x}Fe_2O_4$ NPs with narrow sizes distribution were successfully synthesized by this innovative molten salts methodology, in which XRD patterns, further supported by TEM analysis, confirmed a homogeneous size, and a decrease in crystallinity when the manganese content increases. However, the crystallinity of the produced NPs by this method warrants improvement. This may be possible by increasing the reaction time, or by using a slower heating ramp, for example, where bigger crystals grow at expense of the smaller ones due to the difference of energy among them, previously described by the Ostwald ripening effect mentioned in *Chapter 1.5*. In addition, reactional time presents a greater relevance towards this end, than the annealing temperature, for example, due to the fact that the final particle size is achieved after the nucleation, independently of the temperature.[118] In sum, the present work demonstrates a novel molten salts synthesis, owing to the unprecedented reaction times and low reaction temperatures.

3.3. Comparison of thermal decomposition and molten salt methodologies

From thermal decomposition it is possible to conclude that the produced Mn-Zn ferrites present higher crystallinity in comparison to the ones produced by molten salts methodology. This inherent crystallinity consequently allows the visualization of crystal lattice fringe on the samples. Moreover, the samples obtained by thermal decomposition displayed a defined morphology and a good size distribution without the need to stabilize the NPs with citric acid or EDTA, as demonstrated by the TEM analysis. This contrasts

with the results obtained by molten salts, where the samples exhibited a poorly defined morphology, as well as broad size distributions. However, thermal decomposition methodology sufferers from using costly solvents and surfactants, as well as the need to use a reducing agent in the process. Now addressing some practical concerns, the washing procedure used in thermal decomposition does not allow the use of water due to the presence of surfactants, whereas in molten salts the washes can be performed just with water. Also regarding thermal decomposition methodology, adjustments had to be made concerning the composition of the initial mixture of metallic ions due to the fact that surfactants tend to complex with metal ions, hindering their participation in the nucleation of NPs. Now referring to the strengths of the molten salts methodology, it is noteworthy that in this approach, all the precursors are incorporated into the particles, as shown by EDS analysis. Thus, in this method, it is easier to perform doping in comparison to thermal decomposition methodology. Regarding stirring, thermal decomposition presents a clear advantage in comparison to molten salts methodology, as it performs the synthesis under constant stirring, which consequently improves the interaction between the precursors, providing a better control over nanoparticle size homogeneity and particle morphology, wherein the molten salts methodology, the precursors are mixed without any source of constant stirring.

Overall, both methodologies constitute a valuable approach for the synthesis of Mn-Zn ferrites, where thermal decomposition allows better size distributions and well-defined spherical morphologies, while molten salts constitute a more facile synthesis, from a practical point of view, as well as being considered more a cost-effective methodology.

3.4. Stabilization of MNPs

Both the colloidal and physical stability of the MNPs in water, are of crucial importance for their application in biomedical purposes. Herein, NPs produced by thermal-decomposition methodology are considered hydrophobic because of the adsorption of organic solvents to the NPs surface.[24] With this in mind, two different stabilization strategies were used, namely, with citric acid and EDTA. Regarding the former, citric acid is a biocompatible compound revealed to be efficient for stabilization of ferrites. Noteworthy, the strategy adopted here, follows the Green Chemistry principles, by avoiding the use of organic solvents.[216] From the TEM and DLS data exhibited in Table 6, it is clear that the hydrodynamic diameters determined by DLS are much higher than those observed by TEM. This indicates that there is significant NP

aggregation and suggesting that the stabilization was not successful in obtaining individualized particles. This hypothesis is corroborated by FT-IR and ξ-potential analyses, which confirmed the presence of citric acid in the NPs surface[64], meaning that the issue does not lie in an inefficient stabilization procedure, but rather due to the fact that the NPs were stored in its dried state, which constitutes a practical inconvenience that may be responsible for this occurrence. Now regarding EDTA, the same conclusions can be made regarding size differences between TEM and DLS analysis, which also suggest the stabilization was unsuccessful, since FT-IR and ξ-potential also confirmed the presence of EDTA in the surface of the NPs. It is important to refer that within the current time scope of this thesis, it was not possible to optimize these stabilization methodologies. However, it is possible to conclude that for the stabilization procedure with citric acid at 70 ºC the initial composition of the NPs is affected regardless of the concentration, whereas with 90 ºC and 0.05 M, the initial structure is only slightly affected. Now with respect to EDTA, at 70 ºC it is notable that the initial composition is slightly altered, whereas for 90 ºC with a concentration of 0.005 M, the initial composition is almost the same. Overall, experimental conditions for dispersion are adequate, although at least 3 experiments should be performed under the same reactional conditions to properly conclude about the method's reproducibility.

Table 6. Comparison of the core size and the chemical composition between bare NPs and their subsequent stabilization with citric acid and EDTA.

Sample	Starting NPs	$\langle d \rangle_{TEM}$ (nm)	EDS	*t* (h)	*T* (ºC)	Dispersant	[C] (M)	Mn:Zn:Fe	d_{DLS} (nm)
FP14	TD11	5.8	0.42:0.65:2	4	70	Citric acid	0.05	0.15:0.32:2	2 *dist*
FP16	MS4	3.9	0.42:0.62:2					0.23:0.49:2	177.4
FP15	TD11	5.8	0.42:0.65:2			EDTA	0.005	0.17:0.28:2	259.5
FP17	MS4	3.9	0.42:0.62:2					0.33:0.50:2	245.6
FP20	MS4	3.9	0.42:0.62:2		90	Citric acid	0.05	0.28:0.41:2	612.6
FP19	TD11	5.8	0.42:0.65:2					0.15:0.24:2	153.2
FP18	TD11	5.8	0.42:0.65:2			EDTA	0.005	0.48:0.66:2	173.7
FP21	MS4	3.9	0.42:0.62:2					0.36:0.55:2	284.6

$\langle d \rangle_{TEM}$: particle diameter estimated by TEM analysis, T: temperature, t: time, [C]: concentration, d_{DLS}: hydrodynamic particle diameter, dist: distributions

3.4.1. FT-IR spectroscopy analysis

The stabilization of the as-prepared Mn-Zn ferrites with citric acid and EDTA was evaluated FT-IR vibrational spectroscopy, providing insight regarding their functional

groups. The following spectra of the samples FP16 and FP18 relate to the Mn-Zn ferrites stabilized with citric acid and EDTA, presented in Figure 40 and Figure 41, respectively.

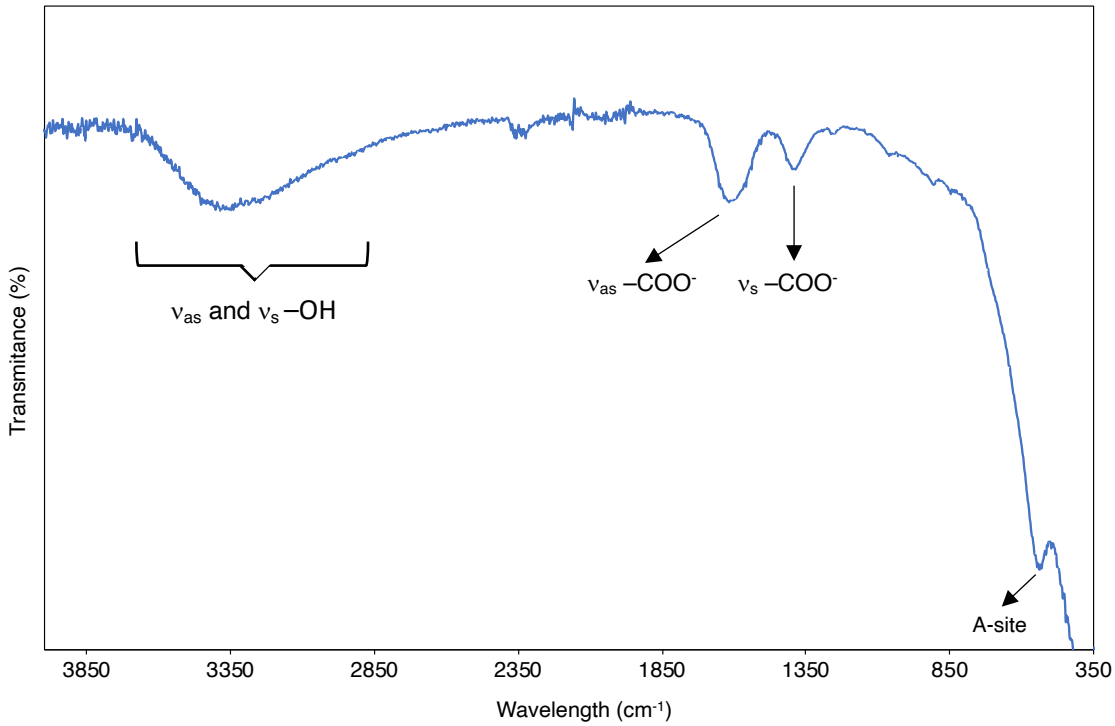

Figure 40. Infrared spectrum of $Mn_xZn_{1-x}Fe_2O_4$ nanoparticles stabilized by citric acid.

Figure 40 display the infrared spectra concerning the citric acid stabilization. The peak at 468 cm^{-1}, it is attributed to the metal-oxygen stretching vibrations in tetrahedral sites (A-site). Notably, this peak is slightly shifted to lower wavelengths in comparison to reports in literature that state that in the absence of citric acid, this peak should be located around 550 cm^{-1}.[172,199,200] As for octahedral symmetry (B-site) related peaks, it is expected that this peak is present, although outside the current wavelength range evaluated in the this analysis. This is claim is supported by the fact that the A-site peak appeared shifted from its expected position, and thus it is possible the same occurs regarding the B-site peak. Therefore, this shift may be explained by the presence of citric acid.[130,168] The absorption band around 1387 cm^{-1} is attributed to asymmetric stretching of $–COO^-$ group of citric acid.[130,168] In addition, the band at 1607 cm^{-1} is attributed to the C=O symmetric stretching vibration from the $–COO^-$ group of citric acid, which confirms the binding of citric acid radicals onto the surface of these Mn-Zn ferrites.[130,168,217,218] The intense absorption band around 3300 cm^{-1} can be assigned to the presence of hydroxyl groups (–OH) on the surface of the NPs.[130,168] According to literature, when the NPs are not properly washed, a citric acid absorption band at 1050 cm^{-1} is expected. This claim is supported by the fact that the FT-IR spectrum of pure citric acid possesses a strong

band around this same region.[218] As evidenced, this peak is not present in the current spectrum, thus it is possible to conclude that the hereby presented NPs are properly washed.

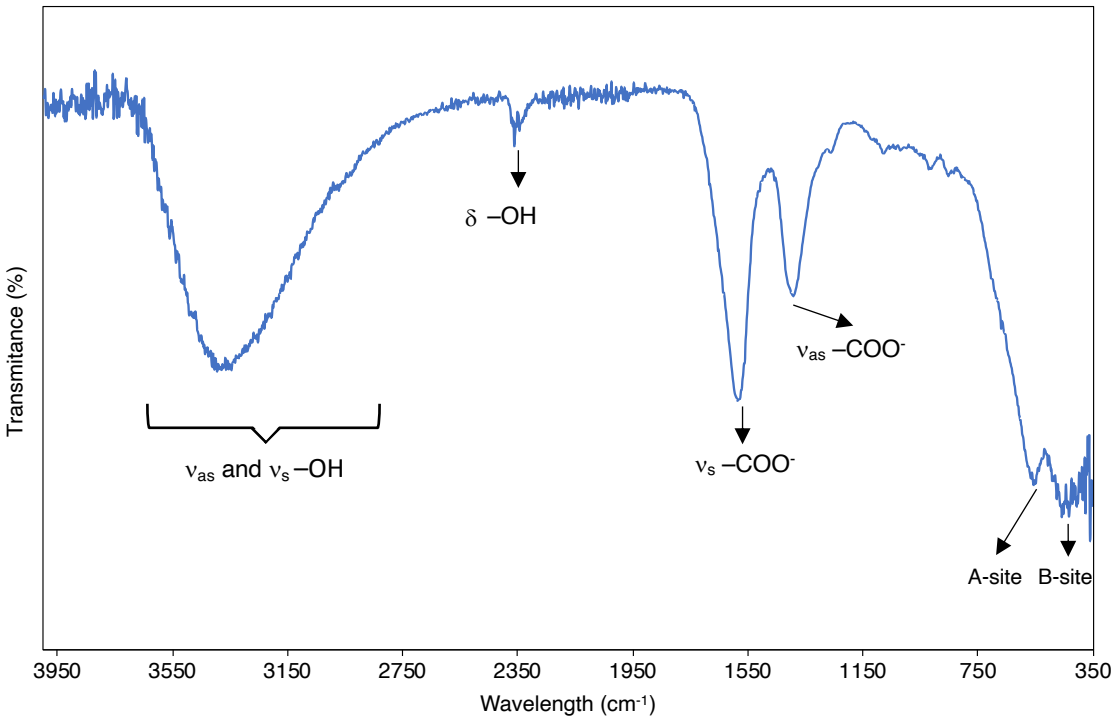

Figure 41. Infrared spectrum of $Mn_xZn_{1-x}Fe_2O_4$ nanoparticles stabilized by EDTA.

With respect to EDTA stabilization, as shown in Figure 41, the peak around 550 cm^{-1} is assigned to the metal-oxygen stretching vibrations in tetrahedral sites (A-site), whereas the peak around 444 cm^{-1} is assigned to the metal-oxygen stretching vibrations in octahedral sites (B-site).[130] The absorption bands at 1584 and 1390 cm^{-1} are allocated to the asymmetric ($–COO^-$) and symmetric ($–COO^-$) stretching vibration band, respectively.[219] Based on the reports from [220,221], these results confirm the functionalization of Mn-Zn ferrites with EDTA. It is important to refer that slight deviations from the wavenumbers present in literature may occur due to differences in the adopted methodologies to obtain the NPs. As for the absorption band present at 3300 cm^{-1} it is attributed to the surface hydroxyl groups (–OH) on the NPs.[130,168]

3.4.2. Zeta Potential analysis

Zeta Potential (ξ-potential) analysis was conducted at a neutral pH to allow the determination of the surface charge of NPs. In Table 7 the results of the two types of NPs with different functionalization are presented, namely the sample FP16 and FP18. These results demonstrate that the NPs coated with citric acid (Figure 42) and EDTA

(Figure 43) possess negative (-) charge, which is in accordance with the expected since carboxylic groups (–COO^-) are available at the surface of the NPs and these can be easily deprotonated (–COO^-) when in an aqueous solution, thus providing negative (-) charge.

Table 7. ξ-potential values for the $Mn_xZn_{1-x}Fe_2O_4$@Citric acid sample (FP16) and for the $Mn_xZn_{1-x}Fe_2O_4$@EDTA sample (FP18).

Sample	ξ-potential (mV)
$Mn_xZn_{1-x}Fe_2O_4$@Citric acid	-14.4
$Mn_xZn_{1-x}Fe_2O_4$@EDTA	-7.49

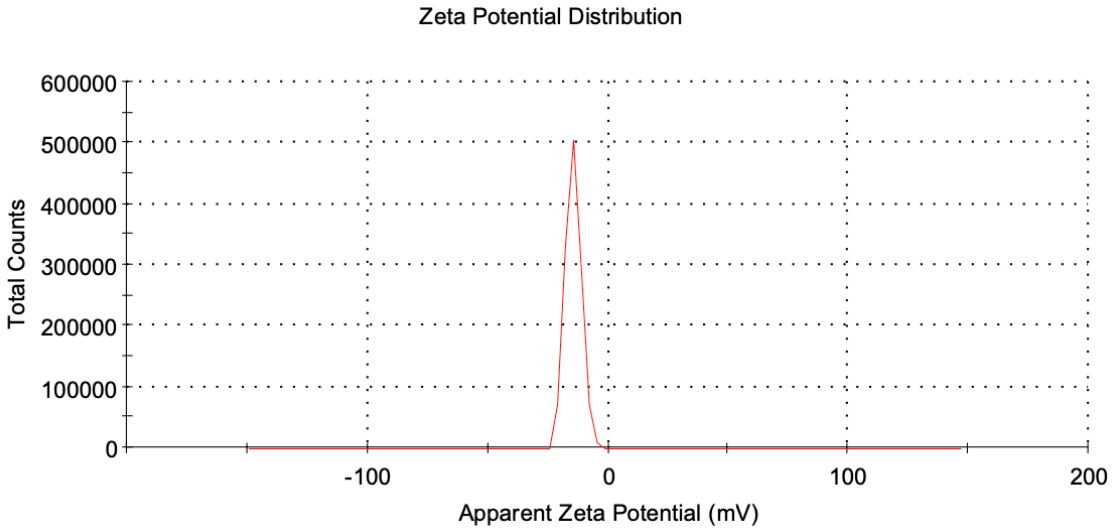

Figure 42. ξ-potential measurement for $Mn_xZn_{1-x}Fe_2O_4$@Citric acid sample (FP16).

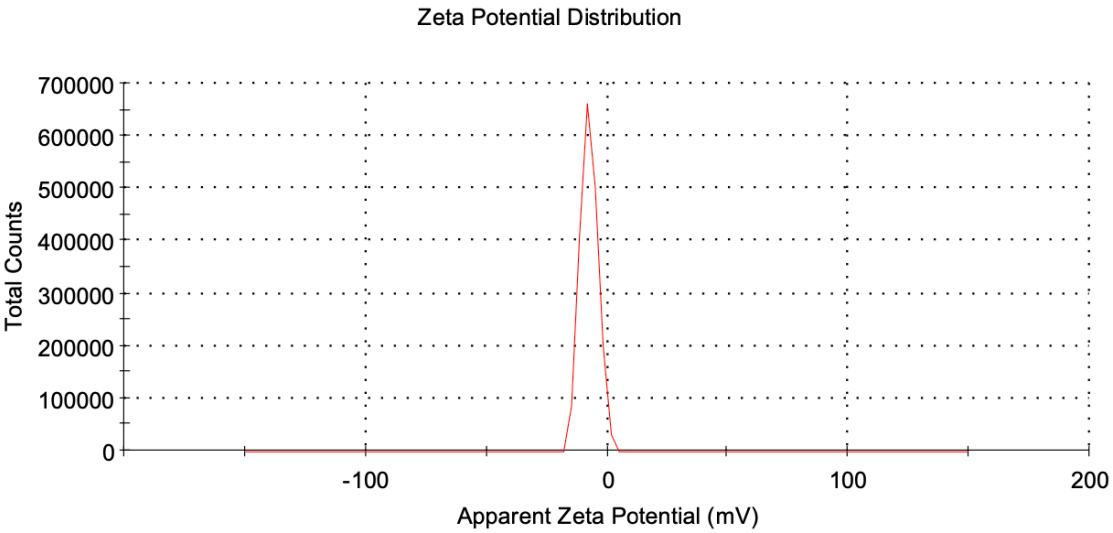

Figure 43. ξ-potential measurement for $Mn_xZn_{1-x}Fe_2O_4$@EDTA sample (FP18).

3.4.3. DLS analysis

The hydrodynamic sizes of the stabilized nanoparticles were measured using DLS (Figure 44). Table 8 shows that the particle size measurements obtained by XRD and TEM do not match, thus verifying that the particles are not well-individualized. Polydispersity index (PdI) measures the homogeneity of the particles, whereas the smaller the value, the more unimodal distribution of NPs. Regarding MNPs, the PdI should not be higher than 0.2.[222,223]

Table 8. Polydispersity index of the as-prepared ferrofluid for both $Mn_xZn_{1-x}Fe_2O_4$@Citric acid sample (FP16) and $Mn_xZn_{1-x}Fe_2O_4$@EDTA sample (FP18).

Sample	PdI_1	PdI_2	PdI_3
$Mn_xZn_{1-x}Fe_2O_4$@Citric acid	0.439	0.438	0.335
$Mn_xZn_{1-x}Fe_2O_4$@EDTA	0.410	0.383	0.365

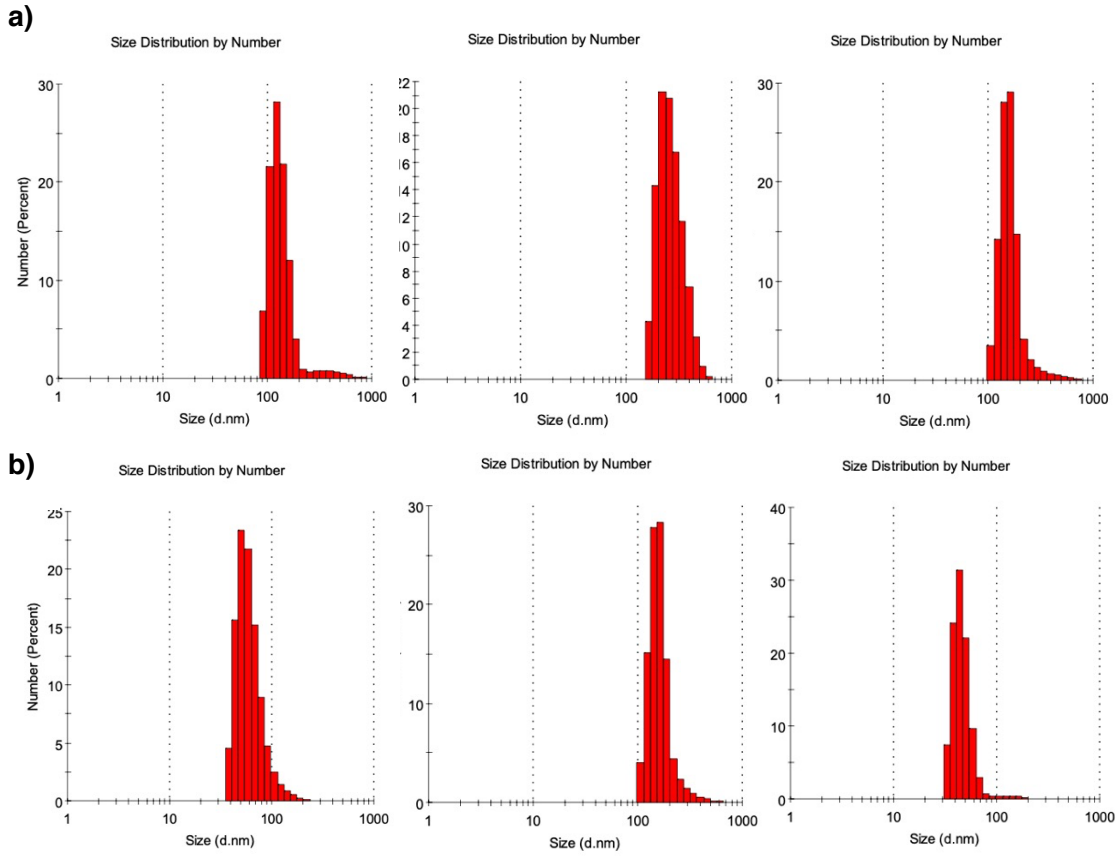

Figure 44. Hydrodynamic diameter of the as-prepared a) $Mn_xZn_{1-x}Fe_2O_4$@Citric acid sample and b) $Mn_xZn_{1-x}Fe_2O_4$@EDTA sample.

3.4.4. SEM analysis

For simplification, only SEM micrographs of FP16 and FP18 sample are depicted in Figure 45, as they correspond NPs stabilized with citric acid and EDTA, respectively. The herein presented micrographs serve to evaluate the stabilization of the MNPs, in which notable particle aggregation is shown. Moreover, comparing with the data from DLS, a higher hydrodynamic diameter was exhibited, suggesting that the NPs, although successfully stabilized with these compounds still are not devoid of aggregation.

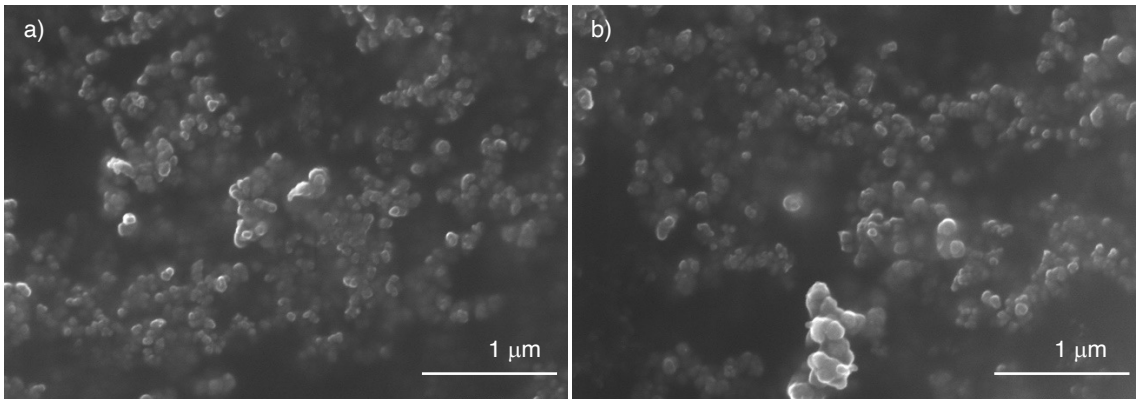

Figure 45. SEM micrographs of a) $Mn_xZn_{1-x}Fe_2O_4$@Citric acid sample and b) $Mn_xZn_{1-x}Fe_2O_4$@EDTA sample.

3.4.5. Internalization of the stabilized NPs

Envisaging the ultimate goal of these NPs, concerns arise regarding the efficient uptake of these particles by the cells to properly create a 3D temperature map. To this end, there are three main factors to consider, namely the size of the NPs, their surface charge, and hydrophobicity.[224,225] Regarding the first, ideally nanoparticles should possess a size higher than 10 nm to avoid renal filtration, but less than 200 nm to prevent liver and spleen accumulation. In addition, it is noteworthy that NPs with less than 100 nm are thought to possess longer circulation times since they show reduced protein attachment.[19,78,86] Now with respect to surface charge, slightly negative charged NPs are less susceptible to be captured by the liver or spleen due to electrostatic repulsion between the NPs and the cells surface.[224] As for hydrophobicity, its influence on this matter is more ambiguous. On one hand, the hydrophobic NP surfaces can improve cellular uptake due to their affinity to the cell membrane lipid bilayer. On the other, hydrophobicity can increase the interaction with proteins in the blood, leading to premature clearance.[225] With this in mind, the hereby presented NPs possess a size range from 5.9 to 15 nm, hydrophobic character and a negative surface charge. As far as size is concerned, these are considered acceptable for being internalized by the cells,

although this would have to be confirmed with more practical studies in the future. However, to address cell internalization issues, a common approach relies on establishing a coating for the NPs, which can simultaneously increase its size, change its surface charge and hydrophobicity, depending on the used material. Some studies show it is possible to achieve cellular uptake without a coating, such as the work done by Iacovita *et al.,* where $Mn_xZn_{1-x}Fe_2O_4$ NPs with an average size of 30 nm demonstrated effective cell penetration through endocytosis.[138] Nevertheless, there are also reports of employing a mesoporous SiO_2 coating on the NPs, as demonstrated by Wang and coworkers, having developed NPs with 7 nm, that with the coating possessed an effective size of 55 nm, displaying good cellular internalization.[179] Yet another example is given by Kandasamy and colleagues, who produced amine-functionalized MIONs, increasing its size from 11.5 to 120 nm and providing a hydrophilic character to the particles, which showed excellent intra-cellular uptake.[226] This opens new pathways for future works where, if needed, similar strategies may be pursued to ensure proper size, surface charge and hydrophobicity to allow a successful cellular uptake and thus enable the creation of a temperature map with these nanothermometers.

3.4.6. Final remarks

In sum, it can be concluded that the stabilization of the herein produced NPs was successfully achieved, as demonstrated by FT-IR spectra and ξ-potential measurements, which confirmed the presence of citric acid and EDTA on the NPs surface. The negative surface charge of FP16 and FP18 sample is associated with the presence of carboxylic groups ($–COO^-$), which are exposed to the solvent. However, both SEM and DLS analysis indicated considerable particle aggregation regardless of the concentration and stabilization agent used, thus suggesting that this approach should be optimized in order to obtain a colloidal suspension capable of remaining stable for long periods of time, as well as present well-individualized particles. Moreover, as was mentioned before, increasing the number of experiments under the same reactional conditions may lead to new conclusions regarding the method's reproducibility.

3.5. 3-D liquified compartmentalized systems as disease models

This developed ferrofluid encapsulation system aims to establish a temperature responsive medium in which temperature measurements by the magnetic thermometers are compared to an external thermometer inserted in both the gelatin core and in the thick gelatin outer layer. This 3-D liquefied compartment will allow us to conclude if the

magnetic thermometers are able to display an accurate temperature measurement. There are several reports in literature concerning the encapsulation of ferrofluids for different purposes. For example, Martina and colleagues took advantage of liposomes and their vesicular structure to encapsulate a maghemite ferrofluid through extrusion of a phospholipid-ferrofluid mixture through porous polycarbonate filters. Alternatively, calcium sodium alginate matrix capsules with an aqueous core also can contribute to the encapsulation of active compounds, providing shielding functions and enabling controlled release.[227] Obeid *et al*. produced magnetic alginate beads by dropping a mixture of sodium alginate and a maghemite ferrofluid through a syringe into a $CaCl_2$ solution. In this case alginate acts as an adsorbent for pollutants gathered through the magnetic pull of the encapsulated MNPs for water decontamination purposes.[228] In a different study, Mosafer and his team produced poly(lactic-co-glycolic acid) (PLGA)-encapsulated superparamagnetic iron oxide NPs for theragnostic applications using various water/oil emulsion strategies with (PLGA).[229] In addition, Rahman *et al.* prepared core-shell magnetic polymer seeds aimed to be used in the separation of biomolecules for biotechnology applications. The researchers used emulsion polymerization of styrene using potassium persulfate (KPS) as an initiator and divinylbenzene (DVB) as a cross-linker in the presence of oil-in-water magnetic emulsion, which produced organic ferrofluid droplets.[230]

As evidenced, there are several approaches to encapsulating ferrofluids. In the present work however, gelatin was chosen as the encapsulating material to acts as a temperature-responsive phantom and, in the liquefied core, serve as a temperature homogenization medium, avoiding the formation of temperature gradients which would hinder precise measurements.[183,231,232] This choice is justified by gelatin cost-effectiveness and its ease of access, making it a suitable choice for the aforementioned purposes.[233,234] It is noteworthy to mention that to achieve a stable capsule, only two dip coatings with alginate were enough, whereas to obtain a stable macrocapsule, three dip coatings were necessary. This experiment also served to verify the mechanical stability of the system. Upon inserting the thermometer inside the microcapsule, as well as inside the core, no protrusions from the inside occurred, suggesting a stable assembly.

Chapter 4: Conclusion and future perspectives

This dissertation focused on the development of magnetic Mn-Zn nanoparticles to act as a temperature sensor for hyperthermia and cryopreservation applications, with

the ultimate goal being the internalization of this system within cells to create real-time, wireless 3-D temperature maps with the aid of a GMR sensor, to monitor processes requiring a thorough temperature control. Hence, monodispersive $Mn_xZn_{1-x}Fe_2O_4$ NPs of different compositions were successfully synthesized and characterized. The synthesis of monodispersive $Mn_xZn_{1-x}Fe_2O_4$ is currently under study by researchers all over the world, however, none was focused in the development on nanothermometers, neither by thermal decomposition nor molten-salts methodologies. Particle diameter was tuned from 5.9 to 15 nm, depending on the reaction conditions and the magnetic properties presented by the TD4 and TD9 samples showed a temperature dependence in a wide range of temperature, which proved suitable to be used in nanothermometry. On the other hand, the herein developed molten salts technique represents an unprecedented, simple and green methodology for the synthesis of $Mn_xZn_{1-x}Fe_2O_4$ NPs.

The surface stabilization of the MNPs obtained by both thermal decomposition methodology and MS methodology was successfully achieved with two stabilizing agents, namely, EDTA and citric acid. Despite almost maintaining their initial chemical composition, the stabilized NPs were not well-individualized and only demonstrated to be stable in a short time period, thus hinting that the concentrations of both these compounds should be optimized to obtain a more stable colloidal suspension for longer periods of time.

Regarding the nanothermometry application, it was not possible to measure the magnetic properties of all the synthetized magnetic particles, although the measurements made for a select few show promising features for hyperthermia and cryogeny applications. In addition, a phantom tissue was successfully fabricated using a simple layer-by-layer technique. Although no temperature measurements could be performed within the current time scope of this thesis, this is already a starting point for future work, where the temperature sensitivity of these nanothermometer will be assessed. With all this in mind, the planned future work includes (Figure 46):

i) Optimize the crystallinity and size of the particles obtained with the molten salts methodology, for example, by increase the reaction time at the annealing temperature or use a slower heating ramp;

ii) Selection of the best suited $Mn_xZn_{1-x}Fe_2O_4$ nanoparticles to act as nanothermometers, *i.e.*, those that show a strong temperature dependence with the magnetization;

iii) Optimization of the concentrations of the biological compounds chosen for functionalization (e.g., SiO_2, PEG) while maintaining the structure composition;

iv) Selection of the optimal ferrofluids for further studies of their magnetic properties, *i.e.*, verify that even in form of ferrofluid they still show a strong temperature dependence with the magnetization;

v) Conduct cytotoxicity assays in order to validate the usage of these systems in biological tissues for *in vivo* real time assessment of temperature changes during hyperthermia and/or cryopreservation.

vi) Internalization of the optimal ferrofluids in gelatin capsules in order to simulate a phantom tissue and evaluate once again the temperature dependence with magnetization, as well as the sensitivity of the thermometers regarding their exterior environment;

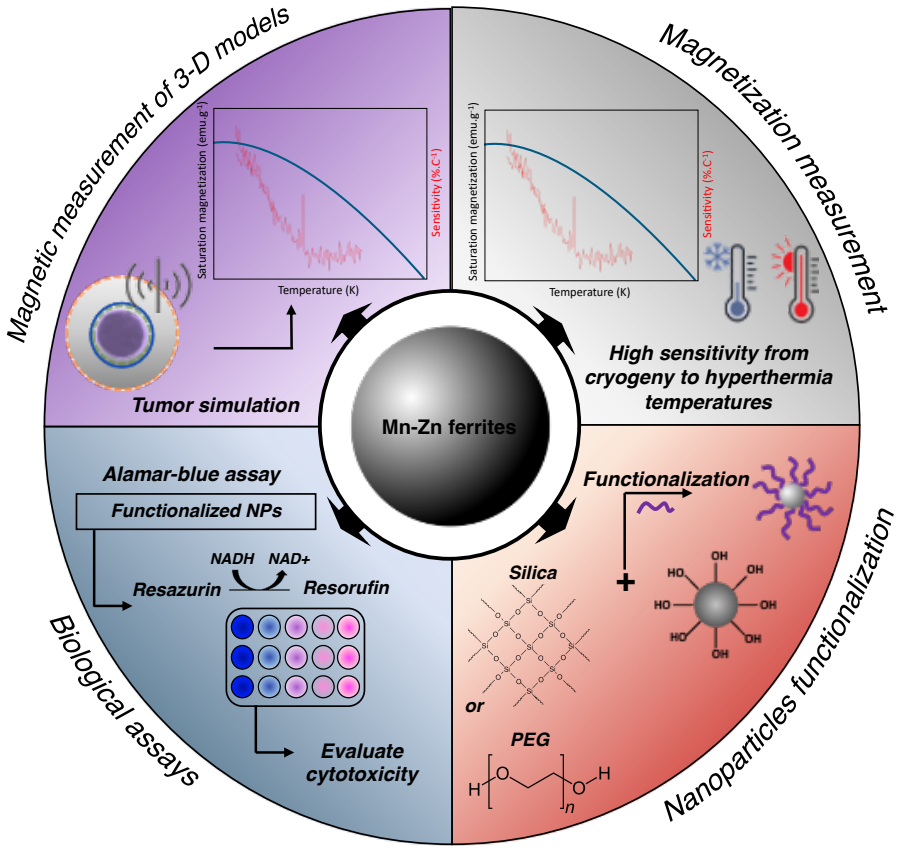

Figure 46. Schematic representation of the possible future work approaches to pursue.

Overall, the results presented in this thesis led to the development of optimized synthesis methodologies for $Mn_xZn_{1-x}Fe_2O_4$ nanoparticles, giving rise to unprecedented applications, namely in nanothermometry and hopefully being used as a platform for the development of new projects regarding temperature mapping at cellular level.

Appendix

Table 9. Reaction conditions of $Mn_{\varkappa}Zn_{1-\varkappa}Fe_2O_4$ NPs obtained by thermal decomposition methodology as well as chemical composition. $\varkappa$ indicates the desired stoichiometric content of Mn in the final composition.

Sample	"$\varkappa$" value	$Mn_{II}(acac)_2$ (g)	$Zn_{II}(acac)_2$ (g)	$Fe_{III}(acac)_3$ (g)	OAm		OA		1,2-HDO		DBE (mL)	Chemical composition
					(g)	(mol)	(g)	(mol)	(g)	(mol)		
TD1	0.13	0.0401	0.2312	0.7331	0.8158	3	0.8821	3	0.4003	1.5	37.5	$Mn_{0.15}Zn_{0.79}Fe_2O_4$
TD2		0.0319	0.2247	0.7209	0.8137	3	0.8454	3	1.2527	1.5	37.5	$Mn_{0.17}Zn_{1.73}Fe_2O_4$
TD3		0.0327	0.2291	0.7102	0.8031	3	0.9034	3	0.3900	1.5	37.5	$Mn_{0.13}Zn_{0.81}Fe_2O_4$
TD4		0.0437	0.4923	0.7121	0.8108	3	0.8671	3	0.3923	5.0	37.5	$Mn_{0.12}Zn_{0.77}Fe_2O_4$
TD5	0.35	0.0907	0.2324	0.7082	0.8221	3	1.0005	3	0.3871	1.5	37.5	$Mn_{0.36}Zn_{0.82}Fe_2O_4$
TD6		0.0901	0.1879	0.7138	0.8115	3	0.8634	3	0.3941	1.5	37.5	$Mn_{0.35}Zn_{0.64}Fe_2O_4$
TD7	0.60	0.1539	0.1086	0.7210	0.8039	3	0.8661	3	0.4125	1.5	37.5	$Mn_{0.60}Zn_{0.38}Fe_2O_4$
TD8		0.1571	0.3178	0.7076	0.8054	3	0.8693	3	0.3849	1.5	37.5	$Mn_{0.62}Zn_{1.13}Fe_2O_4$
TD9		0.1638	0.2761	0.7168	0.8124	3	0.8543	3	0.3918	1.5	20	$Mn_{0.64}Zn_{0.97}Fe_2O_4$
TD10		0.1784	0.3169	0.7070	0.8152	3	0.8656	3	0.3885	1.5	20	$Mn_{0.71}Zn_{1.13}Fe_2O_4$
TD11		0.2041	0.2390	0.7117	0.8039	3	0.8039	3	0.3895	1.5	20	$Mn_{0.80}Zn_{0.84}Fe_2O_4$
TD12		0.1610	0.1246	1.1217	0.8777	3	0.9265	3	1.3025	5.0	20	$Mn_{0.40}Zn_{0.28}Fe_2O_4$
TD13		0.1523	0.1068	0.7243	1.5992	6	1.7100	6	2.6091	10	20	$Mn_{0.59}Zn_{0.37}Fe_2O_4$

Table 10. Chemical composition and structural properties of $Mn_{\varkappa}Zn_{1-\varkappa}Fe_2O_4$ NPs based on XRD and ImageJ measurements. $\varkappa$ indicates the desired stoichiometric content of Mn in the final composition, and a is the lattice parameter of the cubic cell.

Sample	"$\varkappa$" value	Chemical composition	Mn:Zn:Fe	d_{XRD} (nm)	a (Å)	$\langle d \rangle_{TEM}$ (nm)
TD1	0.13	$Mn_{0.15}Zn_{0.79}Fe_2O_4$	0.15:0.47:2	8.3	8.4223	
TD2		$Mn_{0.17}Zn_{1.73}Fe_2O_4$	0.13:0.77:2	7.2	8.4427	
TD3		$Mn_{0.13}Zn_{0.81}Fe_2O_4$	0.07:0.56:2	9.0	8.4262	
TD4		$Mn_{0.12}Zn_{0.77}Fe_2O_4$	0.11:0.78:2	8.0	8.4308	6.6
TD5	0.35	$Mn_{0.36}Zn_{0.82}Fe_2O_4$	0.14:0.54:2	6.8	8.4349	
TD6		$Mn_{0.35}Zn_{0.64}Fe_2O_4$	0.18:0.58:2	6.4	8.4335	7.7
TD7	0.60	$Mn_{0.60}Zn_{0.38}Fe_2O_4$	0.23.0.20:2	10	8.4086	
TD8		$Mn_{0.62}Zn_{1.13}Fe_2O_4$	0.15:0.34:2	14	8.4264	
TD9		$Mn_{0.64}Zn_{0.97}Fe_2O_4$	0.30:0.47:2	6.9	8.4388	7.2
TD10		$Mn_{0.71}Zn_{1.13}Fe_2O_4$	0.21:0.45:2	15	8.4282	6.6
TD11		$Mn_{0.80}Zn_{0.84}Fe_2O_4$	0.42:0.65:2	5.9	8.4366	
TD12		$Mn_{0.40}Zn_{0.28}Fe_2O_4$	0.25:0.22:2	8.9	8.4085	
TD13		$Mn_{0.59}Zn_{0.37}Fe_2O_4$	0.21:0.20:2	7.2	8.3958	5.1

d_{XRD}: particle diameter obtained by XRD data, a: lattice parameter of the cubic cell, $\langle d \rangle_{TEM}$: particle diameter estimated by TEM analysis

Table 11. Reaction conditions of $Mn_{\varkappa}Zn_{1-\varkappa}Fe_2O_4$ NPs obtained by molten salts methodology. $\varkappa$ indicates the desired stoichiometric content of Mn in the final composition.

Sample	"$\varkappa$" value	$Mn(NO_3)_2{\cdot}4H_2O$ (g)	$Fe(NO_3)_3{\cdot}9H_2O$ (g)	$Zn(NO_3)_2{\cdot}6H_2O$ (g)	KNO_3 (g)	Chemical composition
MS1	0.1	0.0248	0.7995	0.2627	1.0001	$Mn_{0.10}Zn_{0.89}Fe_2O_4$
MS2	0.2	0.0497	0.7992	0.2355	1.0000	$Mn_{0.20}Zn_{0.80}Fe_2O_4$
MS3	0.3	0.0754	0.7991	0.2060	1.0010	$Mn_{0.30}Zn_{0.70}Fe_2O_4$
MS4	0.4	0.0992	0.7997	0.1767	1.0010	$Mn_{0.40}Zn_{0.60}Fe_2O_4$
MS5	0.5	0.1245	0.7992	0.1471	1.0037	$Mn_{0.50}Zn_{0.50}Fe_2O_4$
MS6	0.6	0.1491	0.7992	0.1178	1.0023	$Mn_{0.60}Zn_{0.40}Fe_2O_4$
MS7	0.7	0.1739	0.7991	0.0883	1.0008	$Mn_{0.70}Zn_{0.30}Fe_2O_4$
MS8	0.8	0.1989	0.7994	0.0587	0.9996	$Mn_{0.80}Zn_{0.20}Fe_2O_4$
MS9	0.9	0.2238	0.7992	0.0297	1.0002	$Mn_{0.90}Zn_{0.10}Fe_2O_4$

Table 12. Chemical composition, and EDS results of $Mn_{\varkappa}Zn_{1-\varkappa}Fe_2O_4$ NPs synthesized by molten salts methodology. $\varkappa$ indicates the desired stoichiometric content of Mn in the final composition, and a is the lattice parameter of the cubic cell.

Sample	Chemical composition	Mn:Zn:Fe	d_{XRD} (nm)	*a* (Å)	$\langle d \rangle_{TEM}$ (nm)	η (%)
MS1	$Mn_{0.10}Zn_{0.89}Fe_2O_4$	-	-	-	-	-
MS2	$Mn_{0.20}Zn_{0.80}Fe_2O_4$	0.21:0.74:2	4.2	8.4176		48.8
MS3	$Mn_{0.30}Zn_{0.70}Fe_2O_4$	0.31:0.52:2	3.1	8.4005	5.5	49.0
MS4	$Mn_{0.40}Zn_{0.60}Fe_2O_4$	0.42:0.62:2	2.7	8.4115	3.9	45.0
MS5	$Mn_{0.50}Zn_{0.50}Fe_2O_4$	0.52:0.48:2	2.4	8.3628	7.8	49.7
MS6	$Mn_{0.60}Zn_{0.40}Fe_2O_4$	0.63:0.40:2	2.0	8.3461	6.1	43.4
MS7	$Mn_{0.70}Zn_{0.30}Fe_2O_4$	0.62:0.28:2	2.0	8.4125		49.4
MS8	$Mn_{0.80}Zn_{0.20}Fe_2O_4$	0.74:0.18:2	1.3	8.3677		50.0
MS9	$Mn_{0.90}Zn_{0.10}Fe_2O_4$	0.94:0.10:2	1.7	8.3238	3.0	54.0

d_{XRD}: particle diameter obtained by XRD data, $\langle d \rangle_{TEM}$: particle diameter estimated by TEM analysis

Bibliography

(1) Lohmann, K. J.; Lohmann, C. M. F.; Putman, N. F. Magnetic Maps in Animals: Nature's GPS. *J. Exp. Biol.* **2007**, *210* (21), 3697–3705. https://doi.org/10.1242/jeb.001313.

(2) Zhao, Q.; Wang, Y.; Cui, H.; Du, X. Bio-Inspired Sensing and Actuating Materials. *J. Mater. Chem. C* **2019**, *7* (22), 6493–6511. https://doi.org/10.1039/C9TC01483G.

(3) Kwon, O. S.; Song, H. S.; Park, T. H.; Jang, J. Conducting Nanomaterial Sensor Using Natural Receptors. *Chem. Rev.* **2019**, *119* (1), 36–93. https://doi.org/10.1021/acs.chemrev.8b00159.

(4) Brites, C. D. S. S.; Lima, P. P.; Silva, N. J. O. O.; Millán, A.; Amaral, V. S.; Palacio, F.; Carlos, L. D. Thermometry at the Nanoscale. *Nanoscale* **2012**, *4* (16), 4799. https://doi.org/10.1039/c2nr30663h.

(5) Sharma, S. K.; Shrivastava, N.; Rossi, F.; Tung, L. D.; Thanh, N. T. K. Nanoparticles-Based Magnetic and Photo Induced Hyperthermia for Cancer Treatment. *Nano Today* **2019**, *29*, 100795. https://doi.org/10.1016/j.nantod.2019.100795.

(6) Smith, B. T.; Santoro, M.; Grosfeld, E. C.; Shah, S. R.; van den Beucken, J. J. J. P.; Jansen, J. A.; Mikos., A. G. Incorporation of Fast Dissolving Glucose Porogens into an Injectable Calcium Phosphate Cement for Bone Tissue Engineering. *Acta Biomater.* **2017**, *50*, 68–77. https://doi.org/10.1016/j.actbio.2016.12.024.

(7) Size-comparison-Bio-nanoparticles nanometer scale comparison nanoparticle size comparison nanotechnology chart ruler.

(8) Chen, G.; Roy, I.; Yang, C.; Prasad, P. N. Nanochemistry and Nanomedicine for Nanoparticle-Based Diagnostics and Therapy. *Chem. Rev.* **2016**, *116* (5), 2826–2885. https://doi.org/10.1021/acs.chemrev.5b00148.

(9) Wong, X. Y.; Sena-Torralba, A.; Álvarez-Diduk, R.; Muthoosamy, K.; Merkoçi, A. Nanomaterials for Nanotheranostics: Tuning Their Properties According to Disease Needs. *ACS Nano* **2020**, *14* (3), 2585–2627. https://doi.org/10.1021/acsnano.9b08133.

(10) Park, J.; An, K.; Hwang, Y.; Park, J.-G.; Noh, H.-J.; Kim, J.-Y.; Park, J.-H.; Hwang, N.-M.; Hyeon, T. Ultra-Large-Scale Syntheses of Monodisperse Nanocrystals. *Nat. Mater.* **2004**, *3* (12), 891–895. https://doi.org/10.1038/nmat1251.

(11) Roca, A. G.; Gutiérrez, L.; Gavilán, H.; Fortes Brollo, M. E.; Veintemillas-Verdaguer, S.; Morales, M. del P. Design Strategies for Shape-Controlled Magnetic Iron Oxide Nanoparticles. *Adv. Drug Deliv. Rev.* **2019**, *138*, 68–104. https://doi.org/10.1016/j.addr.2018.12.008.

(12) Kinnear, C.; Moore, T. L.; Rodriguez-Lorenzo, L.; Rothen-Rutishauser, B.; Petri-Fink, A. Form Follows Function: Nanoparticle Shape and Its Implications for Nanomedicine. *Chem. Rev.* **2017**, *117* (17), 11476–11521. https://doi.org/10.1021/acs.chemrev.7b00194.

(13) Ding, B.; Zheng, P.; Ma, P.; Lin, J. Manganese Oxide Nanomaterials: Synthesis, Properties, and Theranostic Applications. *Adv. Mater.* **2020**, *32* (10), 1905823. https://doi.org/10.1002/adma.201905823.

(14) Limo, M. J.; Sola-Rabada, A.; Boix, E.; Thota, V.; Westcott, Z. C.; Puddu, V.; Perry, C. C. Interactions between Metal Oxides and Biomolecules: From Fundamental Understanding to Applications. *Chem. Rev.* **2018**, *118* (22), 11118–11193. https://doi.org/10.1021/acs.chemrev.7b00660.

(15) Gloag, L.; Mehdipour, M.; Chen, D.; Tilley, R. D.; Gooding, J. J. Advances in the Application of Magnetic Nanoparticles for Sensing. *Adv. Mater.* **2019**, *31* (48), 1904385. https://doi.org/10.1002/adma.201904385.

(16) Yang, L.; Sun, C.; Lin, H.; Gong, X.; Zhou, T.; Deng, W.; Chen, Z.; Gao, J. Sensitive Contrast-Enhanced Magnetic Resonance Imaging of Orthotopic and Metastatic Hepatic Tumors by Ultralow Doses of Zinc Ferrite Octapods. *Chem. Mater.* **2019**, *31* (4), 1381–1390. https://doi.org/10.1021/acs.chemmater.8b04760.

(17) Saeed, M.; Ren, W.; Wu, A. Therapeutic Applications of Iron Oxide Based Nanoparticles in Cancer: Basic Concepts and Recent Advances. *Biomater. Sci.* **2018**, *6* (4), 708–725. https://doi.org/10.1039/C7BM00999B.

(18) Soares, P. I. P.; Romão, J.; Matos, R.; Silva, J. C.; Borges, J. P. Design and Engineering of Magneto-Responsive Devices for Cancer Theranostics: Nano to Macro Perspective. *Prog. Mater. Sci.* **2021**, *116* (July 2019), 100742. https://doi.org/10.1016/j.pmatsci.2020.100742.

(19) Vaughan, H. J.; Green, J. J.; Tzeng, S. Y. Cancer-Targeting Nanoparticles for Combinatorial Nucleic Acid Delivery. *Adv. Mater.* **2020**, *32* (13), 1901081. https://doi.org/10.1002/adma.201901081.

(20) Kim, D.; Shin, K.; Kwon, S. G.; Hyeon, T. Synthesis and Biomedical Applications of Multifunctional Nanoparticles. *Adv. Mater.* **2018**, *30* (49), 1802309. https://doi.org/10.1002/adma.201802309.

(21) Wu, L.; Mendoza-Garcia, A.; Li, Q.; Sun, S. Organic Phase Syntheses of Magnetic Nanoparticles and Their Applications. *Chem. Rev.* **2016**, *116* (18), 10473–10512. https://doi.org/10.1021/acs.chemrev.5b00687.

(22) Coey, J. M. D. *Magnetism and Magnetic Materials*; Cambridge University Press: Cambridge, 2001. https://doi.org/10.1017/CBO9780511845000.

(23) Callister Jr, W. D.; Rethwisch, D. G. *Materials Science and Engineering - An Introduction*, 10th ed.; Hoboken, NJ : Wiley, 2018.

(24) Das, P.; Colombo, M.; Prosperi, D. Recent Advances in Magnetic Fluid Hyperthermia for Cancer Therapy. *Colloids Surfaces B Biointerfaces* **2019**, *174*, 42–55. https://doi.org/10.1016/j.colsurfb.2018.10.051.

(25) Oliveira-Silva, R.; Pereira, R. A.; Silva, F. M.; Gaspar, V. M.; Ibarra, A.; Millán, Á.; Sousa, F. L.; Mano, J. F.; Silva, N. J. O. O. Temperature-Responsive Nanomagnetic Logic Gates for Cellular Hyperthermia. *Mater. Horizons* **2019**, *6* (3), 524–530. https://doi.org/10.1039/C8MH01510D.

(26) Liu, F.; Hou, Y.; Gao, S. Exchange-Coupled Nanocomposites: Chemical Synthesis, Characterization and Applications. *Chem. Soc. Rev.* **2014**, *43* (23), 8098–8113. https://doi.org/10.1039/C4CS00162A.

(27) Pellicer, E.; Rossinyol, E.; Cabo, M.; Lopez-Ortega, A.; Estrader, M.; Surinach, S.; Dolors, M.; Nogues, J.; Sort, J. Oxide-Matrix Based Nanocomposite Materials for Advanced Magnetic and Optical Functionalities. In *Advances in Nanocomposites - Synthesis, Characterization and Industrial Applications*; InTech, 2011; pp 343–

357. https://doi.org/10.5772/13987.
(28) Colombo, M.; Carregal-Romero, S.; Casula, M. F.; Gutiérrez, L.; Morales, M. P.; Böhm, I. B.; Heverhagen, J. T.; Prosperi, D.; Parak, W. J. Biological Applications of Magnetic Nanoparticles. *Chem. Soc. Rev.* **2012**, *41* (11), 4306. https://doi.org/10.1039/c2cs15337h.
(29) Wu, W.; Jiang, C. Z.; Roy, V. A. L. L. Designed Synthesis and Surface Engineering Strategies of Magnetic Iron Oxide Nanoparticles for Biomedical Applications. *Nanoscale* **2016**, *8* (47), 19421–19474. https://doi.org/10.1039/C6NR07542H.
(30) Reddy, L. H.; Arias, J. L.; Nicolas, J.; Couvreur, P. Magnetic Nanoparticles: Design and Characterization, Toxicity and Biocompatibility, Pharmaceutical and Biomedical Applications. *Chem. Rev.* **2012**, *112* (11), 5818–5878. https://doi.org/10.1021/cr300068p.
(31) Lasheras, X.; Insausti, M.; de la Fuente, J. M.; Gil de Muro, I.; Castellanos-Rubio, I.; Marcano, L.; Fernández-Gubieda, M. L.; Serrano, A.; Martín-Rodríguez, R.; Garaio, E.; et al. Mn-Doping Level Dependence on the Magnetic Response of $Mn_xFe_{3-x}O_4$ Ferrite Nanoparticles. *Dalt. Trans.* **2019**, *48* (30), 11480–11491. https://doi.org/10.1039/C9DT01620A.
(32) Arteaga-Cardona, F.; Pal, U.; María Alonso, J.; de la Presa, P.; Mendoza-Álvarez, M.-E.; Salazar-Kuri, U.; Méndez-Rojas, M. Á. Tuning Magnetic and Structural Properties of $MnFe_2O_4$ Nanostructures by Systematic Introduction of Transition Metal Ions M^{2+} (M = Zn, Fe, Ni, Co). *J. Magn. Magn. Mater.* **2019**, *490*, 165496. https://doi.org/10.1016/j.jmmm.2019.165496.
(33) Silva, N. J. O. Estudos Magnéticos e Estruturais Em Nanopartículas de Óxidos de Ferro Em Matrizes Híbridas, Universidade de Aveiro, 2006.
(34) Noh, S.; Moon, S. H.; Shin, T.-H.; Lim, Y.; Cheon, J. Recent Advances of Magneto-Thermal Capabilities of Nanoparticles: From Design Principles to Biomedical Applications. *Nano Today* **2017**, *13*, 61–76. https://doi.org/10.1016/j.nantod.2017.02.006.
(35) Pi, S.; Zhong, J.; Wei, K.; Liu, W. Optimal Anti-Noise Ability and High Sensitivity in Magnetic Nanothermometry. *IEEE Trans. Nanotechnol.* **2016**, *15* (3), 409–415. https://doi.org/10.1109/TNANO.2016.2538263.
(36) Cotin, G.; Perton, F.; Blanco-Andujar, C.; Pichon, B.; Mertz, D.; Bégin-Colin, S. Design of Anisotropic Iron-Oxide-Based Nanoparticles for Magnetic Hyperthermia. In *Nanomaterials for Magnetic and Optical Hyperthermia Applications*; Elsevier, 2019; pp 41–60. https://doi.org/10.1016/B978-0-12-813928-8.00002-8.
(37) Kucsko, G.; Maurer, P. C.; Yao, N. Y.; Kubo, M.; Noh, H. J.; Lo, P. K.; Park, H.; Lukin, M. D. Nanometre-Scale Thermometry in a Living Cell. *Nature* **2013**, *500* (7460), 54–58. https://doi.org/10.1038/nature12373.
(38) Hankiewicz, J. H.; Celinski, Z.; Stupic, K. F.; Anderson, N. R.; Camley, R. E. Ferromagnetic Particles as Magnetic Resonance Imaging Temperature Sensors. *Nat. Commun.* **2016**, *7* (1), 12415. https://doi.org/10.1038/ncomms12415.
(39) Xu, W.; Liu, W.; Zhang, P. Nanosecond-Resolved Temperature Measurements Using Magnetic Nanoparticles. *Rev. Sci. Instrum.* **2016**, *87* (5), 054902. https://doi.org/10.1063/1.4948737.
(40) Alghamdi, N. A.; Hankiewicz, J. H.; Anderson, N. R.; Stupic, K. F.; Camley, R. E.;

Przybylski, M.; Żukrowski, J.; Celinski, Z. Development of Ferrite-Based Temperature Sensors for Magnetic Resonance Imaging: A Study of $Cu_{1-x}Zn_xFe_2O_4$. *Phys. Rev. Appl.* **2018**, *9* (5), 054030. https://doi.org/10.1103/PhysRevApplied.9.054030.

(41) Zhong, J.; Schilling, M.; Ludwig, F. Spatial and Temperature Resolutions of Magnetic Nanoparticle Temperature Imaging with a Scanning Magnetic Particle Spectrometer. *Nanomaterials* **2018**, *8* (11), 115903. https://doi.org/10.3390/nano8110866.

(42) Wang, Z.; Ma, X.; Zong, S.; Wang, Y.; Chen, H.; Cui, Y. Preparation of a Magnetofluorescent Nano-Thermometer and Its Targeted Temperature Sensing Applications in Living Cells. *Talanta* **2015**, *131*, 259–265. https://doi.org/10.1016/j.talanta.2014.07.088.

(43) Zhong, J.; Dieckhoff, J.; Schilling, M.; Ludwig, F. Influence of Static Magnetic Field Strength on the Temperature Resolution of a Magnetic Nanoparticle Thermometer. *J. Appl. Phys.* **2016**, *120* (14), 143902. https://doi.org/10.1063/1.4964696.

(44) Zhong, J.; Liu, W.; Kong, L.; Morais, P. C. A New Approach for Highly Accurate, Remote Temperature Probing Using Magnetic Nanoparticles. *Sci. Rep.* **2015**, *4* (1), 6338. https://doi.org/10.1038/srep06338.

(45) Li, Z.; Lopez-Ortega, A.; Aranda-Ramos, A.; Tajada, J. L.; Sort, J.; Nogues, C.; Vavassori, P.; Nogues, J.; Sepulveda, B. Simultaneous Local Heating/Thermometry Based on Plasmonic Magnetochromic Nanoheaters. *Small* **2018**, *14* (24), 1–10. https://doi.org/10.1002/smll.201800868.

(46) Zhong, J.; Lucht, N.; Hankiewicz, B.; Schilling, M.; Ludwig, F. Magnetic Field Orientation Dependent Dynamic Susceptibility and Brownian Relaxation Time of Magnetic Nanoparticles. *Appl. Phys. Lett.* **2019**, *115* (13). https://doi.org/10.1063/1.5120609.

(47) Liu, W.; Pi, S. AC Magnetic Nanothermometry: The Influence of Particle Size Distribution. *Proc. Int. Conf. Sens. Technol. ICST* **2016**, 1–3. https://doi.org/10.1109/ICSensT.2016.7796321.

(48) Du, Z.; Sun, Y.; Liu, J.; Su, R.; Yang, M.; Li, N.; Gan, Y.; Ye, N. Design of a Temperature Measurement and Feedback Control System Based on an Improved Magnetic Nanoparticle Thermometer. *Meas. Sci. Technol.* **2018**, *29* (4). https://doi.org/10.1088/1361-6501/aaab00.

(49) Zhong, J.; Liu, W.; Du, Z.; César de Morais, P.; Xiang, Q.; Xie, Q. A Noninvasive, Remote and Precise Method for Temperature and Concentration Estimation Using Magnetic Nanoparticles. *Nanotechnology* **2012**, *23* (7), 075703. https://doi.org/10.1088/0957-4484/23/7/075703.

(50) Zahraei, M.; Monshi, A.; Morales, M. del P.; Shahbazi-Gahrouei, D.; Amirnasr, M.; Behdadfar, B. Hydrothermal Synthesis of Fine Stabilized Superparamagnetic Nanoparticles of Zn^{2+} Substituted Manganese Ferrite. *J. Magn. Magn. Mater.* **2015**, *393* (4), 429–436. https://doi.org/10.1016/j.jmmm.2015.06.006.

(51) Du, Z.; Su, R.; Wei, K.; Gan, Y.; Liu, W. Design and Use of a Very Stable Magnetic Nanothermometer. *Meas. Sci. Technol.* **2016**, *27* (4), 045901. https://doi.org/10.1088/0957-0233/27/4/045901.

(52) Hankiewicz, J. H.; Stoll, J. A.; Stroud, J.; Davidson, J.; Livesey, K. L.; Tvrdy, K.;

Roshko, A.; Russek, S. E.; Stupic, K.; Bilski, P.; et al. Nano-Sized Ferrite Particles for Magnetic Resonance Imaging Thermometry. *J. Magn. Magn. Mater.* **2019**, *469* (September 2018), 550–557. https://doi.org/10.1016/j.jmmm.2018.09.037.

(53) Ivanovskaya, M. I.; Tolstik, A. I.; Pan'kov, V. V. Synthesis of $Zn_{0.5}Mn_{0.5}Fe_2O_4$ by Low-Temperature Spray Pyrolysis. *Inorg. Mater.* **2009**, *45* (11), 1309–1313. https://doi.org/10.1134/S0020168509110223.

(54) Yang, Y. Y.; Liu, X.; Yang, Y. Y.; Xiao, W.; Li, Z.; Xue, D.; Li, F.; Ding, J. Synthesis of Nonstoichiometric Zinc Ferrite Nanoparticles with Extraordinary Room Temperature Magnetism and Their Diverse Applications. *J. Mater. Chem. C* **2013**, *1* (16), 2875. https://doi.org/10.1039/c3tc00790a.

(55) Szczygieł, I.; Winiarska, K.; Bieńko, A.; Suracka, K.; Gaworska-Koniarek, D. The Effect of the Sol-Gel Autocombustion Synthesis Conditions on the Mn-Zn Ferrite Magnetic Properties. *J. Alloys Compd.* **2014**, *604*, 1–7. https://doi.org/10.1016/j.jallcom.2014.03.109.

(56) Zhang, H.; Li, L.; Liu, X. L.; Jiao, J.; Ng, C.; Yi, J. B.; Luo, Y. E.; Bay, B.; Zhao, L. Y.; Peng, M. L.; et al. Ultrasmall Ferrite Nanoparticles Synthesized via Dynamic Simultaneous Thermal Decomposition for High-Performance and Multifunctional T_1 Magnetic Resonance Imaging Contrast Agent. *ACS Nano* **2017**, *11* (4), 3614–3631. https://doi.org/10.1021/acsnano.6b07684.

(57) Phong, P. T.; Nam, P. H.; Manh, D. H.; Lee, I.-J. Mn 0.5 Zn 0.5 Fe 2 O 4 Nanoparticles with High Intrinsic Loss Power for Hyperthermia Therapy. *J. Magn. Magn. Mater.* **2017**, *433*, 76–83. https://doi.org/10.1016/j.jmmm.2017.03.001.

(58) Almessiere, M. A.; Slimani, Y.; Rehman, S.; Khan, F. A.; Polat, E. G.; Sadaqat, A.; Shirsath, S. E.; Baykal, A. Synthesis of Dy-Y Co-Substituted Manganese-zinc Spinel Nanoferrites Induced Anti-Bacterial and Anti-Cancer Activities: Comparison between Sonochemical and Sol-Gel Auto-Combustion Methods. *Mater. Sci. Eng. C* **2020**, *116* (1982), 111186. https://doi.org/10.1016/j.msec.2020.111186.

(59) Pereira, C.; Pereira, A. M.; Fernandes, C.; Rocha, M.; Mendes, R.; Fernández-García, M. P.; Guedes, A.; Tavares, P. B.; Grenèche, J.-M.; Araújo, J. P.; et al. Superparamagnetic MFe_2O_4 (M = Fe, Co, Mn) Nanoparticles: Tuning the Particle Size and Magnetic Properties through a Novel One-Step Coprecipitation Route. *Chem. Mater.* **2012**, *24* (8), 1496–1504. https://doi.org/10.1021/cm300301c.

(60) Zins, D.; Cabuil, V.; Massart, R. New Aqueous Magnetic Fluids. *J. Mol. Liq.* **1999**, *83* (1–3), 217–232. https://doi.org/10.1016/S0167-7322(99)00087-2.

(61) Grasset, F.; Labhsetwar, N.; Li, D.; Park, D. C.; Saito, N.; Haneda, H.; Cador, O.; Roisnel, T.; Mornet, S.; Duguet, E.; et al. Synthesis and Magnetic Characterization of Zinc Ferrite Nanoparticles with Different Environments: Powder, Colloidal Solution, and Zinc Ferrite–Silica Core–Shell Nanoparticles. *Langmuir* **2002**, *18* (21), 8209–8216. https://doi.org/10.1021/la020322b.

(62) Tadic, M.; Milosevic, I.; Kralj, S.; Mitric, M.; Makovec, D.; Sabougni, M.-L.; Motte, L. Synthesis of Metastable Hard-Magnetic ε-Fe_2O_3 Nanoparticles from Silica-Coated Akaganeite Nanorods. *Nanoscale* **2017**, *9* (30), 10579–10584. https://doi.org/10.1039/C7NR03639F.

(63) Gavrilov-Isaac, V.; Neveu, S.; Dupuis, V.; Taverna, D.; Gloter, A.; Cabuil, V. Synthesis of Trimagnetic Multishell $MnFe_2O_4$@$CoFe_2O_4$@$NiFe_2O_4$ Nanoparticles.

Small **2015**, *11* (22), 2614–2618. https://doi.org/10.1002/smll.201402845.

(64) Pardo, A.; Pelaz, B.; Gallo, J.; Bañobre-López, M.; Parak, W. J.; Barbosa, S.; del Pino, P.; Taboada, P. Synthesis, Characterization, and Evaluation of Superparamagnetic Doped Ferrites as Potential Therapeutic Nanotools. *Chem. Mater.* **2020**, *32* (6), 2220–2231. https://doi.org/10.1021/acs.chemmater.9b04848.

(65) Kačenka, M.; Kaman, O.; Jirák, Z.; Maryško, M.; Veverka, P.; Veverka, M.; Vratislav, S. The Magnetic and Neutron Diffraction Studies of $La_{1-x}Sr_xMnO_3$ Nanoparticles Prepared via Molten Salt Synthesis. *J. Solid State Chem.* **2015**, *221*, 364–372. https://doi.org/10.1016/j.jssc.2014.10.024.

(66) Unni, M.; Uhl, A. M.; Savliwala, S.; Savitzky, B. H.; Dhavalikar, R.; Garraud, N.; Arnold, D. P.; Kourkoutis, L. F.; Andrew, J. S.; Rinaldi, C. Thermal Decomposition Synthesis of Iron Oxide Nanoparticles with Diminished Magnetic Dead Layer by Controlled Addition of Oxygen. *ACS Nano* **2017**, *11* (2), 2284–2303. https://doi.org/10.1021/acsnano.7b00609.

(67) Gonell, F.; Alem, N.; Dunne, P.; Crochet, G.; Beaunier, P.; Méthivier, C.; Montero, D.; Laberty-Robert, C.; Doudin, B.; Portehault, D. Versatile Molten Salt Synthesis of Manganite Perovskite Oxide Nanocrystals and Their Magnetic Properties. *ChemNanoMat* **2019**, *5* (3), 358–363. https://doi.org/10.1002/cnma.201800632.

(68) Gubbala, S.; Nathani, H.; Koizol, K.; Misra, R. D. K. Magnetic Properties of Nanocrystalline Ni–Zn, Zn–Mn, and Ni–Mn Ferrites Synthesized by Reverse Micelle Technique. *Phys. B Condens. Matter* **2004**, *348* (1–4), 317–328. https://doi.org/10.1016/j.physb.2003.12.017.

(69) Bram, S.; Gordon, M. N.; Carbonell, M. A.; Pink, M.; Stein, B. D.; Morgan, D. G.; Aguilà, D.; Aromí, G.; Skrabalak, S. E.; Losovyj, Y.; et al. Zn^{2+} Ion Surface Enrichment in Doped Iron Oxide Nanoparticles Leads to Charge Carrier Density Enhancement. *ACS Omega* **2018**, *3* (11), 16328–16337. https://doi.org/10.1021/acsomega.8b02411.

(70) Mdlalose, W. B.; Msomi, J. Z.; Moyo, T. Magnetic Properties of Mn-Substituted Zn–Mg- and Zn–Co-Nanosized Compounds. *J. Supercond. Nov. Magn.* **2019**, *32* (6), 1821–1826. https://doi.org/10.1007/s10948-018-4889-z.

(71) Zhang, Y.; Shi, Q.; Schliesser, J.; Woodfield, B. F.; Nan, Z. Magnetic and Thermodynamic Properties of Nanosized Zn Ferrite with Normal Spinal Structure Synthesized Using a Facile Method. *Inorg. Chem.* **2014**, *53* (19), 10463–10470. https://doi.org/10.1021/ic501487c.

(72) Mamiya, H.; Fukumoto, H.; Cuya Huaman, J. L.; Suzuki, K.; Miyamura, H.; Balachandran, J. Estimation of Magnetic Anisotropy of Individual Magnetite Nanoparticles for Magnetic Hyperthermia. *ACS Nano* **2020**, *14* (7), 8421–8432. https://doi.org/10.1021/acsnano.0c02521.

(73) Sharifi Dehsari, H.; Asadi, K. Impact of Stoichiometry and Size on the Magnetic Properties of Cobalt Ferrite Nanoparticles. *J. Phys. Chem. C* **2018**, *122* (51), 29106–29121. https://doi.org/10.1021/acs.jpcc.8b09276.

(74) Lohr, J.; de Almeida, A. A.; Moreno, M. S.; Troiani, H.; Goya, G. F.; Torres Molina, T. E.; Fernandez-Pacheco, R.; Winkler, E. L.; Vasquez Mansilla, M.; Cohen, R.; et al. Effects of Zn Substitution in the Magnetic and Morphological Properties of Fe-Oxide-Based Core–Shell Nanoparticles Produced in a Single Chemical

Synthesis. *J. Phys. Chem. C* **2019**, *123* (2), 1444–1453. https://doi.org/10.1021/acs.jpcc.8b08988.

(75) Del Bianco, L.; Spizzo, F.; Sgarbossa, P.; Sieni, E.; Barucca, G.; Ruggiero, M. R.; Geninatti Crich, S. Dipolar Magnetic Interactions in Mn-Doped Magnetite Nanoparticles Loaded into PLGA Nanocapsules for Nanomedicine Applications. *J. Phys. Chem. C* **2019**, *123* (49), 30007–30020. https://doi.org/10.1021/acs.jpcc.9b09146.

(76) Harada, M.; Kuwa, M.; Sato, R.; Teranishi, T.; Takahashi, M.; Maenosono, S. Cation Distribution in Monodispersed MFe_2O_4 (M = Mn, Fe, Co, Ni, and Zn) Nanoparticles Investigated by X-Ray Absorption Fine Structure Spectroscopy: Implications for Magnetic Data Storage, Catalysts, Sensors, and Ferrofluids. *ACS Appl. Nano Mater.* **2020**, *3* (8), 8389–8402. https://doi.org/10.1021/acsanm.0c01810.

(77) Kudr, J.; Haddad, Y.; Richtera, L.; Heger, Z.; Cernak, M.; Adam, V.; Zitka, O. Magnetic Nanoparticles: From Design and Synthesis to Real World Applications. *Nanomaterials* **2017**, *7* (9), 243. https://doi.org/10.3390/nano7090243.

(78) Ju, Y.; Dong, B.; Yu, J.; Hou, Y. Inherent Multifunctional Inorganic Nanomaterials for Imaging-Guided Cancer Therapy. *Nano Today* **2019**, *26*, 108–122. https://doi.org/10.1016/j.nantod.2019.03.006.

(79) Qu, Y.; Li, J.; Ren, J.; Leng, J.; Lin, C.; Shi, D. Enhanced Magnetic Fluid Hyperthermia by Micellar Magnetic Nanoclusters Composed of $Mn_xZn_{1-x}Fe_2O_4$ Nanoparticles for Induced Tumor Cell Apoptosis. *ACS Appl. Mater. Interfaces* **2014**, *6* (19), 16867–16879. https://doi.org/10.1021/am5042934.

(80) Moreno Maldonado, A. C.; Winkler, E. L.; Raineri, M.; Toro Córdova, A.; Rodríguez, L. M.; Troiani, H. E.; Mojica Pisciotti, M. L.; Mansilla, M. V.; Tobia, D.; Nadal, M. S.; et al. Free-Radical Formation by the Peroxidase-Like Catalytic Activity of MFe_2O_4 (M = Fe, Ni, and Mn) Nanoparticles. *J. Phys. Chem. C* **2019**, *123* (33), 20617–20627. https://doi.org/10.1021/acs.jpcc.9b05371.

(81) Del Sol-Fernández, S.; Portilla-Tundidor, Y.; Gutiérrez, L.; Odio, O. F.; Reguera, E.; Barber, D. F.; Morales, M. P. Flower-like Mn-Doped Magnetic Nanoparticles Functionalized with $\alpha_v\beta_3$-Integrin-Ligand to Efficiently Induce Intracellular Heat after Alternating Magnetic Field Exposition, Triggering Glioma Cell Death. *ACS Appl. Mater. Interfaces* **2019**, *11* (30), 26648–26663. https://doi.org/10.1021/acsami.9b08318.

(82) Al-Ahmady, Z.; Kostarelos, K. Chemical Components for the Design of Temperature-Responsive Vesicles as Cancer Therapeutics. *Chem. Rev.* **2016**, *116* (6), 3883–3918. https://doi.org/10.1021/acs.chemrev.5b00578.

(83) Pardo, A.; Yáñez, S.; Piñeiro, Y.; Iglesias-Rey, R.; Al-Modlej, A.; Barbosa, S.; Rivas, J.; Taboada, P. Cubic Anisotropic Co- and Zn-Substituted Ferrite Nanoparticles as Multimodal Magnetic Agents. *ACS Appl. Mater. Interfaces* **2020**, *12* (8), 9017–9031. https://doi.org/10.1021/acsami.9b20496.

(84) Du, Y.; Liu, X.; Liang, Q.; Liang, X.; Tian, J. Optimization and Design of Magnetic Ferrite Nanoparticles with Uniform Tumor Distribution for Highly Sensitive MRI/MPI Performance and Improved Magnetic Hyperthermia Therapy. *Nano Lett.* **2019**, *19* (6), 3618–3626. https://doi.org/10.1021/acs.nanolett.9b00630.

(85) Mazario, E.; Menéndez, N.; Herrasti, P.; Cañete, M.; Connord, V.; Carrey, J.

Magnetic Hyperthermia Properties of Electrosynthesized Cobalt Ferrite Nanoparticles. *J. Phys. Chem. C* **2013**, *117* (21), 11405–11411. https://doi.org/10.1021/jp4023025.

(86) Dunne, M.; Hynynen, K.; Allen, C. Thermosensitive Nanomedicines Could Revolutionize Thermal Therapy in Oncology. *Nano Today* **2017**, *16*, 9–13. https://doi.org/10.1016/j.nantod.2017.08.001.

(87) van der Meel, R.; Sulheim, E.; Shi, Y.; Kiessling, F.; Mulder, W. J. M. M.; Lammers, T. Smart Cancer Nanomedicine. *Nat. Nanotechnol.* **2019**, *14* (11), 1007–1017. https://doi.org/10.1038/s41565-019-0567-y.

(88) Tasoglu, S.; Gurkan, U. A.; Wang, S.; Demirci, U. Manipulating Biological Agents and Cells in Micro-Scale Volumes for Applications in Medicine. *Chem. Soc. Rev.* **2013**, *42* (13), 5788–5808. https://doi.org/10.1039/c3cs60042d.

(89) Wang, J.; Zhao, G.; Zhang, Z.; Xu, X.; He, X. Magnetic Induction Heating of Superparamagnetic Nanoparticles during Rewarming Augments the Recovery of HUCM-MSCs Cryopreserved by Vitrification. *Acta Biomater.* **2016**, *33*, 264–274. https://doi.org/10.1016/j.actbio.2016.01.026.

(90) Zhang, Y.; Wang, H.; Stewart, S.; Jiang, B.; Ou, W.; Zhao, G.; He, X. Cold-Responsive Nanoparticle Enables Intracellular Delivery and Rapid Release of Trehalose for Organic-Solvent-Free Cryopreservation. *Nano Lett.* **2019**, *19* (12), 9051–9061. https://doi.org/10.1021/acs.nanolett.9b04109.

(91) Gao, Z.; Ring, H. L.; Sharma, A.; Namsrai, B.; Tran, N.; Finger, E. B.; Garwood, M.; Haynes, C. L.; Bischof, J. C. Preparation of Scalable Silica-Coated Iron Oxide Nanoparticles for Nanowarming. *Adv. Sci.* **2020**, *7* (4), 1901624. https://doi.org/10.1002/advs.201901624.

(92) Wolkers, W. F.; Oldenhof, H. *Cryopreservation and Freeze-Drying Protocols*; Wolkers, W. F., Oldenhof, H., Eds.; Methods in Molecular Biology; Springer US: New York, NY, 2021; Vol. 2180. https://doi.org/10.1007/978-1-0716-0783-1.

(93) Hou, Y.; Lu, C.; Dou, M.; Zhang, C.; Chang, H.; Liu, J.; Rao, W. Soft Liquid Metal Nanoparticles Achieve Reduced Crystal Nucleation and Ultrarapid Rewarming for Human Bone Marrow Stromal Cell and Blood Vessel Cryopreservation. *Acta Biomater.* **2020**, *102*, 403–415. https://doi.org/10.1016/j.actbio.2019.11.023.

(94) Taylor, M. J.; Weegman, B. P.; Baicu, S. C.; Giwa, S. E. New Approaches to Cryopreservation of Cells, Tissues, and Organs. *Transfus. Med. Hemotherapy* **2019**, *46* (3), 197–215. https://doi.org/10.1159/000499453.

(95) Manuchehrabadi, N.; Gao, Z.; Zhang, J.; Ring, H. L.; Shao, Q.; Liu, F.; McDermott, M.; Fok, A.; Rabin, Y.; Brockbank, K. G. M.; et al. Improved Tissue Cryopreservation Using Inductive Heating of Magnetic Nanoparticles. *Sci. Transl. Med.* **2017**, *9* (379), eaah4586. https://doi.org/10.1126/scitranslmed.aah4586.

(96) Shore, D.; Ghemes, A.; Dragos-Pinzaru, O.; Gao, Z.; Shao, Q.; Sharma, A.; Um, J.; Tabakovic, I.; Bischof, J. C.; Stadler, B. J. H. Nanowarming Using Au-Tipped $Co_{35}Fe_{65}$ Ferromagnetic Nanowires. *Nanoscale* **2019**, *11* (31), 14607–14615. https://doi.org/10.1039/C9NR01182J.

(97) Hu, Y.; Mignani, S.; Majoral, J.-P.; Shen, M.; Shi, X. Construction of Iron Oxide Nanoparticle-Based Hybrid Platforms for Tumor Imaging and Therapy. *Chem. Soc. Rev.* **2018**, *47* (5), 1874–1900. https://doi.org/10.1039/C7CS00657H.

(98) Liébana-Viñas, S.; Simeonidis, K.; Wiedwald, U.; Li, Z.-A.; Ma, Z.; Myrovali, E.;

Makridis, A.; Sakellari, D.; Vourlias, G.; Spasova, M.; et al. Optimum Nanoscale Design in Ferrite Based Nanoparticles for Magnetic Particle Hyperthermia. *RSC Adv.* **2016**, *6* (77), 72918–72925. https://doi.org/10.1039/C6RA17892H.

(99) Blanco-Gutiérrez, V.; Andrada-Chacón, A.; Sánchez-Benítez, J.; Urones-Garrote, E.; Sáez-Puche, R.; Torralvo-Fernández, M. J. Superparamagnetic Behavior at Room Temperature through Crystal Chemistry Modification and Particle Assembly Formation: Zinc and Nickel Ferrite Systems. *J. Phys. Chem. C* **2019**, *123* (27), 16973–16981. https://doi.org/10.1021/acs.jpcc.9b01898.

(100) Yang, Y.; Liu, L.; Zhu, H.; Bao, N.; Ding, J.; Chen, J.; Yu, K. Critical Control of Highly Stable Nonstoichiometric Mn–Zn Ferrites with Outstanding Magnetic and Electromagnetic Performance for Gigahertz High-Frequency Applications. *ACS Appl. Mater. Interfaces* **2020**, *12* (14), 16609–16619. https://doi.org/10.1021/acsami.0c00920.

(101) Zhao, Q.; Yan, Z.; Chen, C.; Chen, J. Spinels: Controlled Preparation, Oxygen Reduction/Evolution Reaction Application, and Beyond. *Chem. Rev.* **2017**, *117* (15), 10121–10211. https://doi.org/10.1021/acs.chemrev.7b00051.

(102) Bersweiler, M.; Bender, P.; Vivas, L. G.; Albino, M.; Petrecca, M.; Mühlbauer, S.; Erokhin, S.; Berkov, D.; Sangregorio, C.; Michels, A. Size-Dependent Spatial Magnetization Profile of Manganese-Zinc Ferrite Nanoparticles. *Phys. Rev. B* **2019**, *100* (14), 144434. https://doi.org/10.1103/PhysRevB.100.144434.

(103) Thirupathi, G.; Singh, R. Crystal Structure and Magnetic Properties of Mn-Doped Zn-Ferrite Nanoparticles. *IEEE Trans. Magn.* **2014**, *50* (11), 1–4. https://doi.org/10.1109/TMAG.2014.2329313.

(104) Lak, A.; Kahmann, T.; Schaper, S. J.; Obel, J.; Ludwig, F.; Müller-Buschbaum, P.; Lipfert, J. The Dissociation Rate of Acetylacetonate Ligands Governs the Size of Ferrimagnetic Zinc Ferrite Nanocubes. *ACS Appl. Mater. Interfaces* **2020**, *12* (1), 217–226. https://doi.org/10.1021/acsami.9b17714.

(105) van der Zaag, P. J. Ferrites. In *Encyclopedia of Materials: Science and Technology*; Elsevier, 2001; pp 3033–3037. https://doi.org/10.1016/B0-08-043152-6/00542-8.

(106) Momma, K.; Izumi, F. VESTA 3 for Three-Dimensional Visualization of Crystal, Volumetric and Morphology Data. *J. Appl. Crystallogr.* **2011**, *44* (6), 1272–1276. https://doi.org/10.1107/S0021889811038970.

(107) Graulis, S.; Chateigner, D.; Downs, R. T.; Yokochi, A. F. T.; Quirós, M.; Lutterotti, L.; Manakova, E.; Butkus, J.; Moeck, P.; Le Bail, A. Crystallography Open Database - An Open-Access Collection of Crystal Structures. *J. Appl. Crystallogr.* **2009**, *42* (4), 726–729. https://doi.org/10.1107/S0021889809016690.

(108) Gupta, S. K.; Mao, Y. A Review on Molten Salt Synthesis of Metal Oxide Nanomaterials: Status, Opportunity, and Challenge. *Prog. Mater. Sci.* **2020**, No. January 2019, 100734. https://doi.org/10.1016/j.pmatsci.2020.100734.

(109) Lee, H.; Shin, T.-H.; Cheon, J.; Weissleder, R. Recent Developments in Magnetic Diagnostic Systems. *Chem. Rev.* **2015**, *115* (19), 10690–10724. https://doi.org/10.1021/cr500698d.

(110) Laurent, S.; Forge, D.; Port, M.; Roch, A.; Robic, C.; Vander Elst, L.; Muller, R. N. Magnetic Iron Oxide Nanoparticles: Synthesis, Stabilization, Vectorization, Physicochemical Characterizations, and Biological Applications. *Chem. Rev.*

2010, *110* (4), 2574–2574. https://doi.org/10.1021/cr900197g.

(111) Piché, D.; Tavernaro, I.; Fleddermann, J.; Lozano, J. G.; Varambhia, A.; Maguire, M. L.; Koch, M.; Ukai, T.; Hernández Rodríguez, A. J.; Jones, L.; et al. Targeted T_1 Magnetic Resonance Imaging Contrast Enhancement with Extraordinarily Small $CoFe_2O_4$ Nanoparticles. *ACS Appl. Mater. Interfaces* **2019**, *11* (7), 6724–6740. https://doi.org/10.1021/acsami.8b17162.

(112) Dadfar, S. M.; Roemhild, K.; Drude, N. I.; von Stillfried, S.; Knüchel, R.; Kiessling, F.; Lammers, T. Iron Oxide Nanoparticles: Diagnostic, Therapeutic and Theranostic Applications. *Adv. Drug Deliv. Rev.* **2019**, *138*, 302–325. https://doi.org/10.1016/j.addr.2019.01.005.

(113) de Mello, L. B.; Varanda, L. C.; Sigoli, F. A.; Mazali, I. O. Co-Precipitation Synthesis of (Zn-Mn)-Co-Doped Magnetite Nanoparticles and Their Application in Magnetic Hyperthermia. *J. Alloys Compd.* **2019**, *779*, 698–705. https://doi.org/10.1016/j.jallcom.2018.11.280.

(114) Masud, M. K.; Na, J.; Younus, M.; Hossain, M. S. A.; Bando, Y.; Shiddiky, M. J. A.; Yamauchi, Y. Superparamagnetic Nanoarchitectures for Disease-Specific Biomarker Detection. *Chem. Soc. Rev.* **2019**, *48* (24), 5717–5751. https://doi.org/10.1039/C9CS00174C.

(115) Wu, W.; He, Q.; Jiang, C. Magnetic Iron Oxide Nanoparticles: Synthesis and Surface Functionalization Strategies. *Nanoscale Res. Lett.* **2008**, *3* (11), 397–415. https://doi.org/10.1007/s11671-008-9174-9.

(116) Sun, S.; Zeng, H. Size-Controlled Synthesis of Magnetite Nanoparticles. *J. Am. Chem. Soc.* **2002**, *124* (28), 8204–8205. https://doi.org/10.1021/ja026501x.

(117) Sun, S.; Zeng, H.; Robinson, D. B.; Raoux, S.; Rice, P. M.; Wang, S. X.; Li, G. Monodisperse MFe_2O_4 (M = Fe, Co, Mn) Nanoparticles. *J. Am. Chem. Soc.* **2004**, *126* (1), 273–279. https://doi.org/10.1021/ja0380852.

(118) Pérez-Mirabet, L.; Solano, E.; Martínez-Julián, F.; Guzmán, R.; Arbiol, J.; Puig, T.; Obradors, X.; Pomar, A.; Yáñez, R.; Ros, J.; et al. One-Pot Synthesis of Stable Colloidal Solutions of MFe2O4 Nanoparticles Using Oleylamine as Solvent and Stabilizer. *Mater. Res. Bull.* **2013**, *48* (3), 966–972. https://doi.org/10.1016/j.materresbull.2012.11.086.

(119) Jang, J.; Nah, H.; Lee, J.-H.; Moon, S. H.; Kim, M. G.; Cheon, J. Critical Enhancements of MRI Contrast and Hyperthermic Effects by Dopant-Controlled Magnetic Nanoparticles. *Angew. Chemie Int. Ed.* **2009**, *48* (7), 1234–1238. https://doi.org/10.1002/anie.200805149.

(120) Xie, J.; Yan, C.; Zhang, Y.; Gu, N. Shape Evolution of “Multibranched” Mn–Zn Ferrite Nanostructures with High Performance: A Transformation of Nanocrystals into Nanoclusters. *Chem. Mater.* **2013**, *25* (18), 3702–3709. https://doi.org/10.1021/cm402036d.

(121) Sun, Y.; Yan, C.; Xie, J.; Yan, D.; Hu, K.; Huang, S.; Liu, J.; Zhang, Y.; Gu, N.; Xiong, F. High-Performance Worm-like Mn–Zn Ferrite Theranostic Nanoagents and the Application on Tumor Theranostics. *ACS Appl. Mater. Interfaces* **2019**, *11* (33), 29536–29548. https://doi.org/10.1021/acsami.9b08948.

(122) Wang, Y.; Zou, L.; Qiang, Z.; Jiang, J.; Zhu, Z.; Ren, J. Enhancing Targeted Cancer Treatment by Combining Hyperthermia and Radiotherapy Using Mn–Zn Ferrite Magnetic Nanoparticles. *ACS Biomater. Sci. Eng.* **2020**, *6* (6), 3550–3562.

https://doi.org/10.1021/acsbiomaterials.0c00287.
(123) Torimoto, T.; Tsuda, T.; Okazaki, K.; Kuwabata, S. New Frontiers in Materials Science Opened by Ionic Liquids. *Adv. Mater.* **2010**, *22* (11), 1196–1221. https://doi.org/10.1002/adma.200902184.
(124) Einarsrud, M.-A.; Grande, T. 1D Oxide Nanostructures from Chemical Solutions. *Chem. Soc. Rev.* **2014**, *43* (7), 2187–2199. https://doi.org/10.1039/C3CS60219B.
(125) Okamoto, S.; Narumiya, Y.; Yamaguchi, T. Molten-Salt Synthesis of Flaky MnZn-Ferrite Powder for Electromagnetic Shielding Applications. *Ceram. Int.* **1986**, *12* (4), 209–212. https://doi.org/10.1016/0272-8842(86)90046-5.
(126) Lou, Z.; He, M.; Wang, R.; Qin, W.; Zhao, D.; Chen, C. Large-Scale Synthesis of Monodisperse Magnesium Ferrite via an Environmentally Friendly Molten Salt Route. *Inorg. Chem.* **2014**, *53* (4), 2053–2057. https://doi.org/10.1021/ic402558t.
(127) Yamada, S.; Shigesawa, R.; Latiff, H.; Kishimoto, M.; Kita, E.; Yanagihara, H. Magnetic Properties of Tetragonal Cobalt Manganese Ferrite Particles Prepared Using the Molten Salt Method. *IEEE Trans. Magn.* **2020**, *56* (4), 1–4. https://doi.org/10.1109/TMAG.2019.2962021.
(128) Chen, G.; Qiu, H.; Prasad, P. N.; Chen, X. Upconversion Nanoparticles: Design, Nanochemistry, and Applications in Theranostics. *Chem. Rev.* **2014**, *114* (10), 5161–5214. https://doi.org/10.1021/cr400425h.
(129) Rath, C.; Sahu, K. .; Anand, S.; Date, S. .; Mishra, N. .; Das, R. . Preparation and Characterization of Nanosize Mn–Zn Ferrite. *J. Magn. Magn. Mater.* **1999**, *202* (1), 77–84. https://doi.org/10.1016/S0304-8853(99)00217-6.
(130) Rezaei, B.; Kermanpur, A.; Labbaf, S. Effect of Mn Addition on the Structural and Magnetic Properties of Zn-Ferrite Nanoparticles. *J. Magn. Magn. Mater.* **2019**, *481* (January), 16–24. https://doi.org/10.1016/j.jmmm.2019.02.085.
(131) Kefeni, K. K.; Msagati, T. A. M.; Mamba, B. B. Ferrite Nanoparticles: Synthesis, Characterisation and Applications in Electronic Device. *Mater. Sci. Eng. B* **2017**, *215*, 37–55. https://doi.org/10.1016/j.mseb.2016.11.002.
(132) Kumar, M.; Singh Dosanjh, H.; Sonika; Singh, J.; Monir, K.; Singh, H. Review on Magnetic Nanoferrites and Their Composites as Alternatives in Waste Water Treatment: Synthesis, Modifications and Applications. *Environ. Sci. Water Res. Technol.* **2020**, *6* (3), 491–514. https://doi.org/10.1039/C9EW00858F.
(133) Chatterjee, A.; Das, D.; Pradhan, S. K.; Chakravorty, D. Synthesis of Nanocrystalline Nickel-Zinc Ferrite by the Sol-Gel Method. *J. Magn. Magn. Mater.* **1993**, *127* (1–2), 214–218. https://doi.org/10.1016/0304-8853(93)90217-P.
(134) Mandal, K.; Pan Mandal, S.; Agudo, P.; Pal, M. A Study of Nanocrystalline (Mn–Zn) Ferrite in SiO_2 Matrix. *Appl. Surf. Sci.* **2001**, *182* (3–4), 386–389. https://doi.org/10.1016/S0169-4332(01)00455-X.
(135) Aisida, S. O.; Alnasir, M. H.; Botha, S.; Bashir, A. K. H.; Bucher, R.; Ahmad, I.; Zhao, T.; Maaza, M.; Ezema, F. I. The Role of Polyethylene Glycol on the Microstructural, Magnetic and Specific Absorption Rate in Thermoablation Properties of Mn-Zn Ferrite Nanoparticles by Sol–Gel Protocol. *Eur. Polym. J.* **2020**, *132* (March), 109739. https://doi.org/10.1016/j.eurpolymj.2020.109739.
(136) Ammar, S.; Helfen, A.; Jouini, N.; Fiévet, F.; Rosenman, I.; Villain, F.; Molinié, P.; Danot, M. Magnetic Properties of Ultrafine Cobalt Ferrite Particles Synthesized by Hydrolysis in a Polyol Medium. *J. Mater. Chem.* **2001**, *11* (1), 186–192.

https://doi.org/10.1039/b003193n.
(137) Beji, Z.; Hanini, A.; Smiri, L. S.; Gavard, J.; Kacem, K.; Villain, F.; Grenèche, J.-M.; Chau, F.; Ammar, S. Magnetic Properties of Zn-Substituted $MnFe_2O_4$ Nanoparticles Synthesized in Polyol as Potential Heating Agents for Hyperthermia. Evaluation of Their Toxicity on Endothelial Cells. *Chem. Mater.* **2010**, *22* (19), 5420–5429. https://doi.org/10.1021/cm1001708.
(138) Iacovita, C.; Florea, A.; Scorus, L.; Pall, E.; Dudric, R.; Moldovan, A. I.; Stiufiuc, R.; Tetean, R.; Lucaciu, C. M. Hyperthermia, Cytotoxicity, and Cellular Uptake Properties of Manganese and Zinc Ferrite Magnetic Nanoparticles Synthesized by a Polyol-Mediated Process. *Nanomaterials* **2019**, *9* (10), 1489. https://doi.org/10.3390/nano9101489.
(139) Diodati, S.; Dolcet, P.; Casarin, M.; Gross, S. Pursuing the Crystallization of Mono- and Polymetallic Nanosized Crystalline Inorganic Compounds by Low-Temperature Wet-Chemistry and Colloidal Routes. *Chem. Rev.* **2015**, *115* (20), 11449–11502. https://doi.org/10.1021/acs.chemrev.5b00275.
(140) Shafi, K. V. P. M.; Gedanken, A.; Prozorov, R.; Balogh, J. Sonochemical Preparation and Size-Dependent Properties of Nanostructured $CoFe_2O_4$ Particles. *Chem. Mater.* **1998**, *10* (11), 3445–3450. https://doi.org/10.1021/cm980182k.
(141) Abbas, M.; Parvatheeswara Rao, B.; Nazrul Islam, M.; Kim, K. W.; Naga, S. M.; Takahashi, M.; Kim, C. Size-Controlled High Magnetization $CoFe_2O_4$ Nanospheres and Nanocubes Using Rapid One-Pot Sonochemical Technique. *Ceram. Int.* **2014**, *40* (2), 3269–3276. https://doi.org/10.1016/j.ceramint.2013.09.109.
(142) Almessiere, M. A.; Slimani, Y.; Demir Korkmaz, A.; Güner, S.; Baykal, A.; Shirsath, S. E.; Ercan, I.; Kögerler, P. Sonochemical Synthesis of Dy^{3+} Substituted $Mn_{0.5}Zn_{0.5}Fe_{2-x}O_4$ Nanoparticles: Structural, Magnetic and Optical Characterizations. *Ultrason. Sonochem.* **2020**, *61*, 104836. https://doi.org/10.1016/j.ultsonch.2019.104836.
(143) Baghbanzadeh, M.; Carbone, L.; Cozzoli, P. D.; Kappe, C. O. Microwave-Assisted Synthesis of Colloidal Inorganic Nanocrystals. *Angew. Chemie Int. Ed.* **2011**, *50* (48), 11312–11359. https://doi.org/10.1002/anie.201101274.
(144) Zhenyu, L.; Guangliang, X.; Yalin, Z. Microwave Assisted Low Temperature Synthesis of MnZn Ferrite Nanoparticles. *Nanoscale Res. Lett.* **2007**, *2* (1), 40–43. https://doi.org/10.1007/s11671-006-9027-3.
(145) Liu, J.; Zhang, J. Nanointerface Chemistry: Lattice-Mismatch-Directed Synthesis and Application of Hybrid Nanocrystals. *Chem. Rev.* **2020**, *120* (4), 2123–2170. https://doi.org/10.1021/acs.chemrev.9b00443.
(146) Rivest, J. B.; Jain, P. K. Cation Exchange on the Nanoscale: An Emerging Technique for New Material Synthesis, Device Fabrication, and Chemical Sensing. *Chem. Soc. Rev.* **2013**, *42* (1), 89–96. https://doi.org/10.1039/C2CS35241A.
(147) De Trizio, L.; Manna, L. Forging Colloidal Nanostructures via Cation Exchange Reactions. *Chem. Rev.* **2016**, *116* (18), 10852–10887. https://doi.org/10.1021/acs.chemrev.5b00739.
(148) Li, H.; Zanella, M.; Genovese, A.; Povia, M.; Falqui, A.; Giannini, C.; Manna, L. Sequential Cation Exchange in Nanocrystals: Preservation of Crystal Phase and

Formation of Metastable Phases. *Nano Lett.* **2011**, *11* (11), 4964–4970. https://doi.org/10.1021/nl202927a.

(149) Sytnyk, M.; Kirchschlager, R.; Bodnarchuk, M. I.; Primetzhofer, D.; Kriegner, D.; Enser, H.; Stangl, J.; Bauer, P.; Voith, M.; Hassel, A. W.; et al. Tuning the Magnetic Properties of Metal Oxide Nanocrystal Heterostructures by Cation Exchange. *Nano Lett.* **2013**, *13* (2), 586–593. https://doi.org/10.1021/nl304115r.

(150) Zhao, Z.; Chi, X.; Yang, L.; Yang, R.; Ren, B. W.; Zhu, X.; Zhang, P.; Gao, J. Cation Exchange of Anisotropic-Shaped Magnetite Nanoparticles Generates High-Relaxivity Contrast Agents for Liver Tumor Imaging. *Chem. Mater.* **2016**, *28* (10), 3497–3506. https://doi.org/10.1021/acs.chemmater.6b01256.

(151) Duan, H.; Wang, D.; Li, Y. Green Chemistry for Nanoparticle Synthesis. *Chem. Soc. Rev.* **2015**, *44* (16), 5778–5792. https://doi.org/10.1039/C4CS00363B.

(152) Korbekandi, H.; Iravani, S.; Abbasi, S. Production of Nanoparticles Using Organisms. *Crit. Rev. Biotechnol.* **2009**, *29* (4), 279–306. https://doi.org/10.3109/07388550903062462.

(153) Roh, Y.; Lauf, R. .; McMillan, A. .; Zhang, C.; Rawn, C. .; Bai, J.; Phelps, T. . Microbial Synthesis and the Characterization of Metal-Substituted Magnetites. *Solid State Commun.* **2001**, *118* (10), 529–534. https://doi.org/10.1016/S0038-1098(01)00146-6.

(154) Moon, J.-W.; Roh, Y.; Lauf, R. J.; Vali, H.; Yeary, L. W.; Phelps, T. J. Microbial Preparation of Metal-Substituted Magnetite Nanoparticles. *J. Microbiol. Methods* **2007**, *70* (1), 150–158. https://doi.org/10.1016/j.mimet.2007.04.012.

(155) Byrne, J. M.; Coker, V. S.; Cespedes, E.; Wincott, P. L.; Vaughan, D. J.; Pattrick, R. A. D.; van der Laan, G.; Arenholz, E.; Tuna, F.; Bencsik, M.; et al. Biosynthesis of Zinc Substituted Magnetite Nanoparticles with Enhanced Magnetic Properties. *Adv. Funct. Mater.* **2014**, *24* (17), 2518–2529. https://doi.org/10.1002/adfm.201303230.

(156) Andrade, R. G. D.; Veloso, S. R. S.; Castanheira, E. M. S. Shape Anisotropic Iron Oxide-Based Magnetic Nanoparticles: Synthesis and Biomedical Applications. *Int. J. Mol. Sci.* **2020**, *21* (7), 2455. https://doi.org/10.3390/ijms21072455.

(157) Phor, L.; Kumar, V. Self-Cooling Device Based on Thermomagnetic Effect of $Mn_xZn_{1-x}Fe_2O_4$ (x = 0.3, 0.4, 0.5, 0.6, 0.7)/Ferrofluid. *J. Mater. Sci. Mater. Electron.* **2019**, *30* (10), 9322–9333. https://doi.org/10.1007/s10854-019-01262-8.

(158) Ramimoghadam, D.; Bagheri, S.; Abd Hamid, S. B. Stable Monodisperse Nanomagnetic Colloidal Suspensions: An Overview. *Colloids Surfaces B Biointerfaces* **2015**, *133*, 388–411. https://doi.org/10.1016/j.colsurfb.2015.02.003.

(159) Lovell, P. A.; Schork, F. J. Fundamentals of Emulsion Polymerization. *Biomacromolecules* **2020**, *21* (11), 4396–4441. https://doi.org/10.1021/acs.biomac.0c00769.

(160) Gomes, J. D. A.; Sousa, M. H.; Tourinho, F. A.; Aquino, R.; da Silva, G. J.; Depeyrot, J.; Dubois, E.; Perzynski, R. Synthesis of Core–Shell Ferrite Nanoparticles for Ferrofluids: Chemical and Magnetic Analysis. *J. Phys. Chem. C* **2008**, *112* (16), 6220–6227. https://doi.org/10.1021/jp7097608.

(161) Laurent, S.; Henoumont, C.; Stanicki, D.; Boutry, S.; Lipani, E.; Belaid, S.; Muller, R. N.; Vander Elst, L. *MRI Contrast Agents*; SpringerBriefs in Applied Sciences and Technology; Springer Singapore: Singapore, 2017.

https://doi.org/10.1007/978-981-10-2529-7.

(162) Chen, Z.; Wu, C.; Zhang, Z.; Wu, W.; Wang, X.; Yu, Z. Synthesis, Functionalization, and Nanomedical Applications of Functional Magnetic Nanoparticles. *Chinese Chem. Lett.* **2018**, *29* (11), 1601–1608. https://doi.org/10.1016/j.cclet.2018.08.007.

(163) Khanna, L.; Verma, N. K.; Tripathi, S. K. Burgeoning Tool of Biomedical Applications - Superparamagnetic Nanoparticles. *J. Alloys Compd.* **2018**, *752*, 332–353. https://doi.org/10.1016/j.jallcom.2018.04.093.

(164) Xie, J.; Yan, C.; Yan, Y.; Chen, L.; Song, L.; Zang, F.; An, Y.; Teng, G.; Gu, N.; Zhang, Y. Multi-Modal Mn–Zn Ferrite Nanocrystals for Magnetically-Induced Cancer Targeted Hyperthermia: A Comparison of Passive and Active Targeting Effects. *Nanoscale* **2016**, *8* (38), 16902–16915. https://doi.org/10.1039/C6NR03916B.

(165) Palma, S. I. C. J.; Marciello, M.; Carvalho, A.; Veintemillas-Verdaguer, S.; Morales, M. del P.; Roque, A. C. A. Effects of Phase Transfer Ligands on Monodisperse Iron Oxide Magnetic Nanoparticles. *J. Colloid Interface Sci.* **2015**, *437*, 147–155. https://doi.org/10.1016/j.jcis.2014.09.019.

(166) Dheyab, M. A.; Aziz, A. A.; Jameel, M. S.; Noqta, O. A.; Khaniabadi, P. M.; Mehrdel, B. Simple Rapid Stabilization Method through Citric Acid Modification for Magnetite Nanoparticles. *Sci. Rep.* **2020**, *10* (1), 10793. https://doi.org/10.1038/s41598-020-67869-8.

(167) Ling, W.; Wang, M.; Xiong, C.; Xie, D.; Chen, Q.; Chu, X.; Qiu, X.; Li, Y.; Xiao, X. Synthesis, Surface Modification, and Applications of Magnetic Iron Oxide Nanoparticles. *J. Mater. Res.* **2019**, *34* (11), 1828–1844. https://doi.org/10.1557/jmr.2019.129.

(168) Zahraei, M.; Marciello, M.; Lazaro-Carrillo, A.; Villanueva, A.; Herranz, F.; Talelli, M.; Costo, R.; Monshi, A.; Shahbazi-Gahrouei, D.; Amirnasr, M.; et al. Versatile Theranostics Agents Designed by Coating Ferrite Nanoparticles with Biocompatible Polymers. *Nanotechnology* **2016**, *27* (25), 255702. https://doi.org/10.1088/0957-4484/27/25/255702.

(169) kanagesan, S.; Aziz, S.; Hashim, M.; Ismail, I.; Tamilselvan, S.; Alitheen, N.; Swamy, M.; Purna Chandra Rao, B. Synthesis, Characterization and in Vitro Evaluation of Manganese Ferrite ($MnFe_2O_4$) Nanoparticles for Their Biocompatibility with Murine Breast Cancer Cells (4T1). *Molecules* **2016**, *21* (3), 312. https://doi.org/10.3390/molecules21030312.

(170) Mehta, R. V. Synthesis of Magnetic Nanoparticles and Their Dispersions with Special Reference to Applications in Biomedicine and Biotechnology. *Mater. Sci. Eng. C* **2017**, *79*, 901–916. https://doi.org/10.1016/j.msec.2017.05.135.

(171) Aquino, V. R. R.; Vinícius-Araújo, M.; Shrivastava, N.; Sousa, M. H.; Coaquira, J. A. H.; Bakuzis, A. F. Role of the Fraction of Blocked Nanoparticles on the Hyperthermia Efficiency of Mn-Based Ferrites at Clinically Relevant Conditions. *J. Phys. Chem. C* **2019**, *123* (45), 27725–27734. https://doi.org/10.1021/acs.jpcc.9b06599.

(172) Monfared, A. H.; Zamanian, A.; Beygzadeh, M.; Sharifi, I.; Mozafari, M. A Rapid and Efficient Thermal Decomposition Approach for the Synthesis of Manganese-Zinc/Oleylamine Core/Shell Ferrite Nanoparticles. *J. Alloys Compd.* **2017**, *693*,

1090–1095. https://doi.org/10.1016/j.jallcom.2016.09.253.
(173) Ge, J.; Zhai, M.; Zhang, Y.; Bian, J.; Wu, J. Biocompatible Fe_3O_4/Chitosan Scaffolds with High Magnetism. *Int. J. Biol. Macromol.* **2019**, *128*, 406–413. https://doi.org/10.1016/j.ijbiomac.2019.01.077.
(174) Shete, P. B.; Patil, R. M.; Thorat, N. D.; Prasad, A.; Ningthoujam, R. S.; Ghosh, S. J.; Pawar, S. H. Magnetic Chitosan Nanocomposite for Hyperthermia Therapy Application: Preparation, Characterization and in Vitro Experiments. *Appl. Surf. Sci.* **2014**, *288*, 149–157. https://doi.org/10.1016/j.apsusc.2013.09.169.
(175) Yang, C.; Jie, R.; Jianbo, L.; Yan, L. Preparation and Characterization of Mn–Zn Ferrite/Poly(N,N′-Isopropyl Acrylamide) Core/Shell Nanocomposites via in-Situ Polymerization. *Mater. Lett.* **2010**, *64* (14), 1570–1573. https://doi.org/10.1016/j.matlet.2010.04.049.
(176) Wang, X.; Wang, L.; Lim, I.-I.; Bao, K.; Mott, D.; Park, H.-Y.; Luo, J.; Hao, S.; Zhong, C.-J. Synthesis, Characterization and Potential Application of MnZn Ferrite and MnZn Ferrite@Au Nanoparticles. *J. Nanosci. Nanotechnol.* **2009**, *9* (5), 3005–3012. https://doi.org/10.1166/jnn.2009.206.
(177) Ning, P.; Liu, C. C.; Wang, Y. J.; Li, X. Z.; Ranjithkumar, R.; Gan, Z. H.; Wu, Y. Y.; Fu, T. Facile Synthesis, Antibacterial Mechanisms and Cytocompatibility of Ag–$MnFe_2O_4$ Magnetic Nanoparticles. *Ceram. Int.* **2020**, *46* (12), 20105–20115. https://doi.org/10.1016/j.ceramint.2020.05.085.
(178) Kaman, O.; Dědourková, T.; Koktan, J.; Kuličková, J.; Maryško, M.; Veverka, P.; Havelek, R.; Královec, K.; Turnovcová, K.; Jendelová, P.; et al. Silica-Coated Manganite and Mn-Based Ferrite Nanoparticles: A Comparative Study Focused on Cytotoxicity. *J. Nanoparticle Res.* **2016**, *18* (4). https://doi.org/10.1007/s11051-016-3402-5.
(179) Wang, C.; Zhao, N.; Huang, Y.; He, R.; Xu, S.; Yuan, W. Coordination of Injectable Self-Healing Hydrogel with Mn-Zn Ferrite@mesoporous Silica Nanospheres for Tumor MR Imaging and Efficient Synergistic Magnetothermal-Chemo-Chemodynamic Therapy. *Chem. Eng. J.* **2020**, *401*, 126100. https://doi.org/10.1016/j.cej.2020.126100.
(180) Ring, H. L.; Sharma, A.; Ivkov, R.; Bischof, J. C. The Impact of Data Selection and Fitting on SAR Estimation for Magnetic Nanoparticle Heating. *Int. J. Hyperth.* **2020**, *37* (3), 100–107. https://doi.org/10.1080/02656736.2020.1810332.
(181) Ma, M.; Zhang, Y.; Gu, N. Estimation the Tumor Temperature in Magnetic Nanoparticle Hyperthermia by Infrared Thermography: Phantom and Numerical Studies. *J. Therm. Biol.* **2018**, *76* (March), 89–94. https://doi.org/10.1016/j.jtherbio.2018.07.004.
(182) Kaczmarek, K.; Mrówczyński, R.; Hornowski, T.; Bielas, R.; Józefczak, A. The Effect of Tissue-Mimicking Phantom Compressibility on Magnetic Hyperthermia. *Nanomaterials* **2019**, *9* (5), 803. https://doi.org/10.3390/nano9050803.
(183) Dabbagh, A.; Abdullah, B. J. J.; Ramasindarum, C.; Abu Kasim, N. H. Tissue-Mimicking Gel Phantoms for Thermal Therapy Studies. *Ultrason. Imaging* **2014**, *36* (4), 291–316. https://doi.org/10.1177/0161734614526372.
(184) Miaskowski, A.; Sawicki, B. Magnetic Fluid Hyperthermia Modeling Based on Phantom Measurements and Realistic Breast Model. *IEEE Trans. Biomed. Eng.* **2013**, *60* (7), 1806–1813. https://doi.org/10.1109/TBME.2013.2242071.

(185) Ashikbayeva, Z.; Aitkulov, A.; Jelbuldina, M.; Issatayeva, A.; Beisenova, A.; Molardi, C.; Saccomandi, P.; Blanc, W.; Inglezakis, V. J.; Tosi, D. Distributed 2D Temperature Sensing during Nanoparticles Assisted Laser Ablation by Means of High-Scattering Fiber Sensors. *Sci. Rep.* **2020**, *10* (1), 12593. https://doi.org/10.1038/s41598-020-69384-2.

(186) Albarqi, H. A.; Wong, L. H.; Schumann, C.; Sabei, F. Y.; Korzun, T.; Li, X.; Hansen, M. N.; Dhagat, P.; Moses, A. S.; Taratula, O.; et al. Biocompatible Nanoclusters with High Heating Efficiency for Systemically Delivered Magnetic Hyperthermia. *ACS Nano* **2019**, *13* (6), 6383–6395. https://doi.org/10.1021/acsnano.8b06542.

(187) Morrow, L.; Snow, B.; Ali, A.; Maguire-Boyle, S. J.; Almutairi, Z.; Potter, D. K.; Barron, A. R. Temperature Dependence on the Mass Susceptibility and Mass Magnetization of Superparamagnetic Mn–Zn–Ferrite Nanoparticles as Contrast Agents for Magnetic Imaging of Oil and Gas Reservoirs. *J. Exp. Nanosci.* **2018**, *13* (1), 107–118. https://doi.org/10.1080/17458080.2018.1426894.

(188) Thi N'Goc, H. Le; Mouafo, L. D. N.; Etrillard, C.; Torres-Pardo, A.; Dayen, J.-F.; Rano, S.; Rousse, G.; Laberty-Robert, C.; Calbet, J. G.; Drillon, M.; et al. Surface-Driven Magnetotransport in Perovskite Nanocrystals. *Adv. Mater.* **2017**, *29* (9), 1604745. https://doi.org/10.1002/adma.201604745.

(189) Shaw, S. K.; Biswas, A.; Gangwar, A.; Maiti, P.; Prajapat, C. L.; Meena, S. S.; Prasad, N. K. Synthesis of Exchange Coupled Nanoflowers for Efficient Magnetic Hyperthermia. *J. Magn. Magn. Mater.* **2019**, *484*, 437–444. https://doi.org/10.1016/j.jmmm.2019.04.056.

(190) Morelli, S.; Holdich, R. G.; Dragosavac, M. M. Microparticles for Cell Encapsulation and Colonic Delivery Produced by Membrane Emulsification. *J. Memb. Sci.* **2017**, *524*, 377–388. https://doi.org/10.1016/j.memsci.2016.11.058.

(191) Sakai, S.; Ito, S.; Inagaki, H.; Hirose, K.; Matsuyama, T.; Taya, M.; Kawakami, K. Cell-Enclosing Gelatin-Based Microcapsule Production for Tissue Engineering Using a Microfluidic Flow-Focusing System. *Biomicrofluidics* **2011**, *5* (1), 013402. https://doi.org/10.1063/1.3516657.

(192) Kaman, O.; Kuličková, J.; Herynek, V.; Koktan, J.; Maryško, M.; Dědourková, T.; Knížek, K.; Jirák, Z. Preparation of Mn-Zn Ferrite Nanoparticles and Their Silica-Coated Clusters: Magnetic Properties and Transverse Relaxivity. *J. Magn. Magn. Mater.* **2017**, *427* (June 2016), 251–257. https://doi.org/10.1016/j.jmmm.2016.10.095.

(193) Hao, R.; Xing, R.; Xu, Z.; Hou, Y.; Gao, S.; Sun, S. Synthesis, Functionalization, and Biomedical Applications of Multifunctional Magnetic Nanoparticles. *Adv. Mater.* **2010**, *22* (25), 2729–2742. https://doi.org/10.1002/adma.201000260.

(194) Pereira, R. A. Desenvolvimento de Nanopartículas Magnéticas Para Dispositivos Biomédicos, Aveiro, 2018.

(195) Jović Orsini, N.; Milić, M. M.; Torres, T. E. Zn- and (Mn, Zn)-Substituted versus Unsubstituted Magnetite Nanoparticles: Structural, Magnetic and Hyperthermic Properties. *Nanotechnology* **2020**, *31* (22), 225707. https://doi.org/10.1088/1361-6528/ab76e7.

(196) Moya, C.; Batlle, X.; Labarta, A. The Effect of Oleic Acid on the Synthesis of $Fe_{3-x}O_4$ Nanoparticles over a Wide Size Range. *Phys. Chem. Chem. Phys.* **2015**, *17* (41), 27373–27379. https://doi.org/10.1039/C5CP03395K.

(197) Mahhouti, Z.; El Moussaoui, H.; Mahfoud, T.; Hamedoun, M.; El Marssi, M.; Lahmar, A.; El Kenz, A.; Benyoussef, A. Chemical Synthesis and Magnetic Properties of Monodisperse Cobalt Ferrite Nanoparticles. *J. Mater. Sci. Mater. Electron.* **2019**, *30* (16), 14913–14922. https://doi.org/10.1007/s10854-019-01863-3.

(198) Mourdikoudis, S.; Liz-Marzán, L. M. Oleylamine in Nanoparticle Synthesis. *Chem. Mater.* **2013**, *25* (9), 1465–1476. https://doi.org/10.1021/cm4000476.

(199) Yang, K.; Peng, H.; Wen, Y.; Li, N. Re-Examination of Characteristic FTIR Spectrum of Secondary Layer in Bilayer Oleic Acid-Coated Fe3O4 Nanoparticles. *Appl. Surf. Sci.* **2010**, *256* (10), 3093–3097. https://doi.org/10.1016/j.apsusc.2009.11.079.

(200) Monfared, A. H.; Zamanian, A.; Sharifi, I.; Mozafari, M. Reversible Multistimuli-Responsive Manganese–Zinc Ferrite/P(NIPAAM-AAc-AAm) Core-Shell Nanoparticles: A Programmed Ferrogel System. *Mater. Chem. Phys.* **2019**, *226*, 44–50. https://doi.org/10.1016/j.matchemphys.2019.01.016.

(201) Klokkenburg, M.; Hilhorst, J.; Erné, B. H. Surface Analysis of Magnetite Nanoparticles in Cyclohexane Solutions of Oleic Acid and Oleylamine. *Vib. Spectrosc.* **2007**, *43* (1), 243–248. https://doi.org/10.1016/j.vibspec.2006.09.008.

(202) Harris, R. A.; Shumbula, P. M.; van der Walt, H. Analysis of the Interaction of Surfactants Oleic Acid and Oleylamine with Iron Oxide Nanoparticles through Molecular Mechanics Modeling. *Langmuir* **2015**, *31* (13), 3934–3943. https://doi.org/10.1021/acs.langmuir.5b00671.

(203) Wang, T.; Luan, Z.-Z.; Ge, J.-Y.; Liu, L.; Wu, D.; Lv, Z.-P.; Zuo, J.-L.; Sun, S. Enhancing Low-Field Magnetoresistance in Magnetite Nanoparticles via Zinc Substitution. *Phys. Chem. Chem. Phys.* **2018**, *20* (25), 17245–17252. https://doi.org/10.1039/C8CP00843D.

(204) Piñol, R.; Zeler, J.; Brites, C. D. S.; Gu, Y.; Téllez, P.; Carneiro Neto, A. N.; Da Silva, T. E.; Moreno-Loshuertos, R.; Fernandez-Silva, P.; Gallego, A. I.; et al. Real-Time Intracellular Temperature Imaging Using Lanthanide-Bearing Polymeric Micelles. *Nano Lett.* **2020**, *20* (9), 6466–6472. https://doi.org/10.1021/acs.nanolett.0c02163.

(205) Suzuki, M.; Plakhotnik, T. The Challenge of Intracellular Temperature. *Biophys. Rev.* **2020**, *12* (2), 593–600. https://doi.org/10.1007/s12551-020-00683-8.

(206) Aras, S.; Purandare, N.; Gladyck, S.; Somayajulu-Nitu, M.; Zhang, K.; Wallace, D. C.; Grossman, L. I. Mitochondrial Nuclear Retrograde Regulator 1 (MNRR1) Rescues the Cellular Phenotype of MELAS by Inducing Homeostatic Mechanisms. *Proc. Natl. Acad. Sci.* **2020**, *117* (50), 32056–32065. https://doi.org/10.1073/pnas.2005877117.

(207) Liu, S.; Li, S.; Wu, S.; Wang, L.; Chou, K. A Novel Method for Vanadium Slag Comprehensive Utilization to Synthesize Zn-Mn Ferrite and Fe-V-Cr Alloy. *J. Hazard. Mater.* **2018**, *354*, 99–106. https://doi.org/10.1016/j.jhazmat.2018.04.061.

(208) Yang, L.; Ma, L.; Xin, J.; Li, A.; Sun, C.; Wei, R.; Ren, B. W.; Chen, Z.; Lin, H.; Gao, J. Composition Tunable Manganese Ferrite Nanoparticles for Optimized T_2 Contrast Ability. *Chem. Mater.* **2017**, *29* (7), 3038–3047. https://doi.org/10.1021/acs.chemmater.7b00035.

(209) Mamani, J. B.; Gamarra, L. F.; Brito, G. E. de S. Synthesis and Characterization of Fe_3O_4 Nanoparticles with Perspectives in Biomedical Applications. *Mater. Res.* **2014**, *17* (3), 542–549. https://doi.org/10.1590/S1516-14392014005000050.

(210) Thota, S.; Kashyap, S. C.; Sharma, S. K.; Reddy, V. R. Micro Raman, Mossbauer and Magnetic Studies of Manganese Substituted Zinc Ferrite Nanoparticles: Role of Mn. *J. Phys. Chem. Solids* **2016**, *91*, 136–144. https://doi.org/10.1016/j.jpcs.2015.12.013.

(211) Beji, Z.; Sun, M.; Smiri, L. S.; Herbst, F.; Mangeney, C.; Ammar, S. Polyol Synthesis of Non-Stoichiometric Mn–Zn Ferrite Nanocrystals: Structural /Microstructural Characterization and Catalytic Application. *RSC Adv.* **2015**, *5* (80), 65010–65022. https://doi.org/10.1039/C5RA07562A.

(212) Mourdikoudis, S.; Pallares, R. M.; Thanh, N. T. K. K. Characterization Techniques for Nanoparticles: Comparison and Complementarity upon Studying Nanoparticle Properties. *Nanoscale* **2018**, *10* (27), 12871–12934. https://doi.org/10.1039/C8NR02278J.

(213) Simeonidis, K.; Martinez-Boubeta, C.; Serantes, D.; Ruta, S.; Chubykalo-Fesenko, O.; Chantrell, R.; Oró-Solé, J.; Balcells, L.; Kamzin, A. S.; Nazipov, R. A.; et al. Controlling Magnetization Reversal and Hyperthermia Efficiency in Core–Shell Iron–Iron Oxide Magnetic Nanoparticles by Tuning the Interphase Coupling. *ACS Appl. Nano Mater.* **2020**, *3* (5), 4465–4476. https://doi.org/10.1021/acsanm.0c00568.

(214) Wu, T.; Ding, F.; Li, D.; Zhong, H. Composition Dependent Structural and Magnetic Properties of Mn–Zn Ferrite. *ChemistrySelect* **2020**, *5* (47), 14978–14985. https://doi.org/10.1002/slct.202003205.

(215) Varshney, D.; Verma, K.; Kumar, A. Structural and Vibrational Properties of $Zn_xMn_{1-x}Fe_2O_4$ (X=0.0, 0.25, 0.50, 0.75, 1.0) Mixed Ferrites. *Mater. Chem. Phys.* **2011**, *131* (1–2), 413–419. https://doi.org/10.1016/j.matchemphys.2011.09.066.

(216) Winterton, N. Green Chemistry: Deliverance or Distraction? *Clean Technol. Environ. Policy* **2016**, *18* (4), 991–1001. https://doi.org/10.1007/s10098-016-1118-y.

(217) Mahto, T. K.; Roy, A.; Sahoo, B.; Sahu, S. K. Citric Acid Fuctionalized Magnetic Ferrite Nanoparticles for Photocatalytic Degradation of Azo Dye. *J. Nanosci. Nanotechnol.* **2015**, *15* (1), 273–280. https://doi.org/10.1166/jnn.2015.9223.

(218) Sahoo, Y.; Goodarzi, A.; Swihart, M. T.; Ohulchanskyy, T. Y.; Kaur, N.; Furlani, E. P.; Prasad, P. N. Aqueous Ferrofluid of Magnetite Nanoparticles: Fluorescence Labeling and Magnetophoretic Control. *J. Phys. Chem. B* **2005**, *109* (9), 3879–3885. https://doi.org/10.1021/jp045402y.

(219) Shalbafan, M.; Esmaeilzadeh, F.; Safaei, A.; XiaopoWang. Experimental Investigation of Wettability Alteration and Oil Recovery Enhance in Carbonate Reservoirs Using Iron Oxide Nanoparticles Coated with EDTA or SLS. *J. Pet. Sci. Eng.* **2019**, *180* (January), 559–568. https://doi.org/10.1016/j.petrol.2019.05.085.

(220) Shah, E.; Upadhyay, P.; Singh, M.; Mansuri, M. S.; Begum, R.; Sheth, N.; Soni, H. P. EDTA Capped Iron Oxide Nanoparticles Magnetic Micelles: Drug Delivery Vehicle for Treatment of Chronic Myeloid Leukemia and T_1–T_2 Dual Contrast Agent for Magnetic Resonance Imaging. *New J. Chem.* **2016**, *40* (11), 9507–9519. https://doi.org/10.1039/C6NJ00655H.

(221) Magdalena, A. G.; Silva, I. M. B.; Marques, R. F. C.; Pipi, A. R. F.; Lisboa-Filho, P. N.; Jafelicci, M. EDTA-Functionalized Fe_3O_4 Nanoparticles. *J. Phys. Chem. Solids* **2018**, *113*, 5–10. https://doi.org/10.1016/j.jpcs.2017.10.002.

(222) Danaei, M.; Dehghankhold, M.; Ataei, S.; Hasanzadeh Davarani, F.; Javanmard, R.; Dokhani, A.; Khorasani, S.; Mozafari, M. Impact of Particle Size and Polydispersity Index on the Clinical Applications of Lipidic Nanocarrier Systems. *Pharmaceutics* **2018**, *10* (2), 57. https://doi.org/10.3390/pharmaceutics10020057.

(223) Lalatonne, Y.; Richardi, J.; Pileni, M. P. Van Der Waals versus Dipolar Forces Controlling Mesoscopic Organizations of Magnetic Nanocrystals. *Nat. Mater.* **2004**, *3* (2), 121–125. https://doi.org/10.1038/nmat1054.

(224) Pearce, A. K.; O'Reilly, R. K. Insights into Active Targeting of Nanoparticles in Drug Delivery: Advances in Clinical Studies and Design Considerations for Cancer Nanomedicine. *Bioconjug. Chem.* **2019**, *30* (9), 2300–2311. https://doi.org/10.1021/acs.bioconjchem.9b00456.

(225) Nel, A. E.; Mädler, L.; Velegol, D.; Xia, T.; Hoek, E. M. V.; Somasundaran, P.; Klaessig, F.; Castranova, V.; Thompson, M. Understanding Biophysicochemical Interactions at the Nano–Bio Interface. *Nat. Mater.* **2009**, *8* (7), 543–557. https://doi.org/10.1038/nmat2442.

(226) Kandasamy, G.; Soni, S.; Sushmita, K.; Veerapu, N. S.; Bose, S.; Maity, D. One-Step Synthesis of Hydrophilic Functionalized and Cytocompatible Superparamagnetic Iron Oxide Nanoparticles (SPIONs) Based Aqueous Ferrofluids for Biomedical Applications. *J. Mol. Liq.* **2019**, *274*, 653–663. https://doi.org/10.1016/j.molliq.2018.10.161.

(227) Mincheva, R.; Stoilova, O.; Penchev, H.; Ruskov, T.; Spirov, I.; Manolova, N.; Rashkov, I. Synthesis of Polymer-Stabilized Magnetic Nanoparticles and Fabrication of Nanocomposite Fibers Thereof Using Electrospinning. *Eur. Polym. J.* **2008**, *44* (3), 615–627. https://doi.org/10.1016/j.biomaterials.2007.05.025.

(228) Obeid, L.; El Kolli, N.; Dali, N.; Talbot, D.; Abramson, S.; Welschbillig, M.; Cabuil, V.; Bée, A. Adsorption of a Cationic Surfactant by a Magsorbent Based on Magnetic Alginate Beads. *J. Colloid Interface Sci.* **2014**, *432*, 182–189. https://doi.org/10.1016/j.jcis.2014.06.027.

(229) Mosafer, J.; Abnous, K.; Tafaghodi, M.; Jafarzadeh, H.; Ramezani, M. Preparation and Characterization of Uniform-Sized PLGA Nanospheres Encapsulated with Oleic Acid-Coated Magnetic-Fe_3O_4 Nanoparticles for Simultaneous Diagnostic and Therapeutic Applications. *Colloids Surfaces A Physicochem. Eng. Asp.* **2017**, *514* (1–3), 146–154. https://doi.org/10.1016/j.colsurfa.2016.11.056.

(230) Rahman, M. M.; Chehimi, M. M.; Fessi, H.; Elaissari, A. Highly Temperature Responsive Core-Shell Magnetic Particles: Synthesis, Characterization and Colloidal Properties. *J. Colloid Interface Sci.* **2011**, *360* (2), 556–564. https://doi.org/10.1016/j.jcis.2011.04.078.

(231) Madsen, E. L.; Hobson, M. A.; Shi, H.; Varghese, T.; Frank, G. R. Tissue-Mimicking Agar/Gelatin Materials for Use in Heterogeneous Elastography Phantoms. *Phys. Med. Biol.* **2005**, *50* (23), 5597–5618. https://doi.org/10.1088/0031-9155/50/23/013.

(232) Farrer, A. I.; Odéen, H.; de Bever, J.; Coats, B.; Parker, D. L.; Payne, A.; Christensen, D. A. Characterization and Evaluation of Tissue-Mimicking Gelatin

Phantoms for Use with MRgFUS. *J. Ther. Ultrasound* **2015**, *3* (1), 9. https://doi.org/10.1186/s40349-015-0030-y.

(233) Afewerki, S.; Sheikhi, A.; Kannan, S.; Ahadian, S.; Khademhosseini, A. Gelatin-Polysaccharide Composite Scaffolds for 3D Cell Culture and Tissue Engineering: Towards Natural Therapeutics. *Bioeng. Transl. Med.* **2019**, *4* (1), 96–115. https://doi.org/10.1002/btm2.10124.

(234) Bello, A. B.; Kim, D.; Kim, D.; Park, H.; Lee, S.-H. Engineering and Functionalization of Gelatin Biomaterials: From Cell Culture to Medical Applications. *Tissue Eng. Part B Rev.* **2020**, *26* (2), 164–180. https://doi.org/10.1089/ten.teb.2019.0256.